

APPLIED COMPUTATIONAL ELECTROMAGNETICS SOCIETY JOURNAL

June 2023
Vol. 38 No. 6
ISSN 1054-4887

The ACES Journal is abstracted in INSPEC, in Engineering Index, DTIC, Science Citation Index Expanded, the Research Alert, and to Current Contents/Engineering, Computing & Technology.

The illustrations on the front cover have been obtained from the ARC research group at the Department of Electrical Engineering, Colorado School of Mines

Published, sold and distributed by: River Publishers, Alsbjergvej 10, 9260 Gistrup, Denmark

THE APPLIED COMPUTATIONAL ELECTROMAGNETICS SOCIETY

<http://aces-society.org>

EDITORS-IN-CHIEF

Atef Elsherbeni
Colorado School of Mines, EE Dept.
Golden, CO 80401, USA

Sami Barmada
University of Pisa, ESE Dept.
56122 Pisa, Italy

ASSOCIATE EDITORS

Maokun Li
Tsinghua University
Beijing 100084, China

Wei-Chung Weng
National Chi Nan University, EE Dept.
Puli, Nantou 54561, Taiwan

Paolo Mezzanotte
University of Perugia
I-06125 Perugia, Italy

Mauro Parise
University Campus Bio-Medico of Rome
00128 Rome, Italy

Alessandro Formisano
Seconda Università di Napoli
81031 CE, Italy

Luca Di Rienzo
Politecnico di Milano
20133 Milano, Italy

Yingsong Li
Harbin Engineering University
Harbin 150001, China

Piotr Gas
AGH University of Science and Technology
30-059 Krakow, Poland

Lei Zhao
Jiangsu Normal University
Jiangsu 221116, China

Riyadh Mansoor
Al-Muthanna University
Samawa, Al-Muthanna, Iraq

Long Li
Xidian University
Shaanxi, 710071, China

Sima Noghianian
Commscope
Sunnyvale, CA 94089, USA

Lijun Jiang
University of Hong Kong, EEE Dept.
Hong Kong

Steve J. Weiss
US Army Research Laboratory
Adelphi Laboratory Center (RDRL-SER-M)
Adelphi, MD 20783, USA

Nunzia Fontana
University of Pisa
56122 Pisa, Italy

Shinishihiro Ohnuki
Nihon University
Tokyo, Japan

Jiming Song
Iowa State University, ECE Dept.
Ames, IA 50011, USA

Stefano Selleri
DINFO - University of Florence
50139 Florence, Italy

Kubilay Sertel
The Ohio State University
Columbus, OH 43210, USA

Toni Bjorninen
Tampere University
Tampere, 33100, Finland

Yu Mao Wu
Fudan University
Shanghai 200433, China

Giulio Antonini
University of L'Aquila
67040 L'Aquila, Italy

Santanu Kumar Behera
National Institute of Technology
Rourkela-769008, India

Fatih Kaburcuk
Sivas Cumhuriyet University
Sivas 58140, Turkey

Antonio Musolino
University of Pisa
56126 Pisa, Italy

Daniele Romano
University of L'Aquila
67100 L'Aquila, Italy

Huseyin Savci
Istanbul Medipol University
34810 Beykoz, Istanbul

Abdul A. Arkadan
Colorado School of Mines, EE Dept.
Golden, CO 80401, USA

Alireza Baghai-Wadji
University of Cape Town
Cape Town, 7701, South Africa

Zhixiang Huang
Anhui University
China

Salvatore Campione
Sandia National Laboratories
Albuquerque, NM 87185, USA

Marco Arjona López
La Laguna Institute of Technology
Torreon, Coahuila 27266, Mexico

Amin Kargar Behbahani
Florida International University
Miami, FL 33174, USA

Ibrahim Mahariq
American University of the Middle East
Kuwait and University of
Turkish Aeronautical Association
Turkey

Kaikai Xu
University of Electronic Science
and Technology of China
China

Laila Marzall
University of Colorado, Boulder
Boulder, CO 80309, USA

EDITORIAL ASSISTANTS

Matthew J. Inman
University of Mississippi, EE Dept.
University, MS 38677, USA

Shanell Lopez
Colorado School of Mines, EE Dept.
Golden, CO 80401, USA

EMERITUS EDITORS-IN-CHIEF

Duncan C. Baker
EE Dept. U. of Pretoria
0002 Pretoria, South Africa

Allen Glisson
University of Mississippi, EE Dept.
University, MS 38677, USA

Ahmed Kishk
Concordia University, ECS Dept.
Montreal, QC H3G 1M8, Canada

Robert M. Bevensee
Box 812
Alamo, CA 94507-0516

Ozlem Kilic
Catholic University of America
Washington, DC 20064, USA

David E. Stein
USAF Scientific Advisory Board
Washington, DC 20330, USA

EMERITUS ASSOCIATE EDITORS

Yasushi Kanai
Niigata Inst. of Technology
Kashiwazaki, Japan

Mohamed Abouzahra
MIT Lincoln Laboratory
Lexington, MA, USA

Alexander Yakovlev
University of Mississippi, EE Dept.
University, MS 38677, USA

Levent Gurel
Bilkent University
Ankara, Turkey

Sami Barmada
University of Pisa, ESE Dept.
56122 Pisa, Italy

Ozlem Kilic
Catholic University of America
Washington, DC 20064, USA

Erdem Topsakal
Mississippi State University, EE Dept.
Mississippi State, MS 39762, USA

Alistair Duffy
De Montfort University
Leicester, UK

Fan Yang
Tsinghua University, EE Dept.
Beijing 100084, China

Rocco Rizzo
University of Pisa
56123 Pisa, Italy

Atif Shamim
King Abdullah University of Science and
Technology (KAUST)
Thuwal 23955, Saudi Arabia

William O'Keefe Coburn
US Army Research Laboratory
Adelphi, MD 20783, USA

Mohammed Hadi
Kuwait University, EE Dept.
Safat, Kuwait

Amedeo Capozzoli
Univerita di Naoli Federico II, DIETI
I-80125 Napoli, Italy

Wenxing Li
Harbin Engineering University
Harbin 150001, China

Qiang Ren
Beihang University
Beijing 100191, China

EMERITUS EDITORIAL ASSISTANTS

Khaleb ElMaghoub
Trimble Navigation/MIT
Boston, MA 02125, USA

Kyle Patel
Colorado School of Mines, EE Dept.
Golden, CO 80401, USA

Christina Bonnington
University of Mississippi, EE Dept.
University, MS 38677, USA

Anne Graham
University of Mississippi, EE Dept.
University, MS 38677, USA

Madison Lee
Colorado School of Mines, EE Dept.
Golen, CO 80401, USA

Allison Tanner
Colorado School of Mines, EE Dept.
Golden, CO 80401, USA

Mohamed Al Sharkawy
Arab Academy for Science and Technology, ECE Dept.
Alexandria, Egypt

JUNE 2023 REVIEWERS

**Rabah W. Aldhaferi
Mahendran C.
Matteo Cerretelli
Chakravarthy
Arkaprovo Das
Veysel Demir
Dina Ellaithy
Nasr H. Gad
Haroldo Hattori
Bernhard J. Hoenders
Brian LaRocca
Andrew Peterson**

**Gowri Manohari Ravishankar
Sivaprakash S. C.
Haoran Sun
Siyang Sun
Ye Tian
Steven Weiss
Kaikai Xu
Salah I. Yahya
Abubakar Yakubu
Shihyuan Yeh
Wentao Yuan
Yun-Qi Zhang**

TABLE OF CONTENTS

Improved and Easy-to-implement HFSS-MATLAB Interface without VBA Scripts:
An Insightful Application to the Numerical Design of Patch Antennas
Giacomo Giannetti 377

Mutual Coupling Compensation-based Nonuniform Fourier Transform Technique
for Accurate and Efficient Pattern Evaluation and its Application to Synthesis of
Aperiodic Arrays
Fan Peng, Cheng Liao, You-Feng Cheng, Ju Feng, and Si-Du Wang 382

Planar Antenna Design on the Characteristics of Moore Fractal-based High Impedance
Surface
Akash K. Gupta, Paladuga S. R. Chowdary, and Mandhapati V. Krishna 392

Convolutional Neural Network for Array Size Selection of a Dual-band Reconfigurable
Array
Garrett A. Harris, Corey M. Stamper, and Michael A. Saville 400

Flat-topped Beams using Phase Compensation based on Low-profile Transmitarray
Hui Zhang, Tianhang Lan, Shan Zhao, Qingqi He, and Zengrui Li 409

Design and Evaluation of Ultra-broadband Metamaterial Absorber for Energy Harvesting
Applications
Ebenezer Abishek, Elakkiya Azhagar, Manikandan Esakkimuthu,
and Karthigeyan Arumugam 416

Narrow-band Circularly Polarized Antenna for Medical Microwave Imaging and Health
Monitoring Applications
Bilal Guetaf, Abdelhalim Chaabane, Abderrezak Khalfallaoui, and Hussein Attia 424

Low-profile Circularly Polarized Conformal Antenna Array with Side Lobe Suppression
for Vehicular SATCOM Applications
Ebenezer Abishek, Ramesh Subramaniam, Parthasarathy Ramanujam,
and Manikandan Esakkimuthu 439

Unified Formulation for Evaluation and Visualization of Electric and Magnetic Fields Inside Waveguides and Cavities Zahid Hasan and Atef Elsherbeni	448
CMOS High Swing and Q Boosted Dual Core Voltage Controlled Oscillator for 5G New Radio Application Pravinah Shasidharan, Jagadheswaran Rajendran, Selvakumar Mariappan, Narendra Kumar, and Masuri Othman	457

Improved and Easy-to-implement HFSS-MATLAB Interface without VBA Scripts: An Insightful Application to the Numerical Design of Patch Antennas

Giacomo Giannetti

Department of Information Engineering
Università degli Studi di Firenze, Florence, Italy
giacomo.giannetti@unifi.it

Abstract – An improved and easy-to-implement HFSS-MATLAB interface is presented. Because the interface is realized without the use of VBA scripts, it is easier to implement for beginners and practitioners. This advantage allows more dissemination of the code in the HFSS community. The interface is applied to the numerical design of a patch antenna, showing the capabilities it enables. Practical details about the implementation are provided, enabling the reader to implement the interface on their own.

Index Terms – application programming interface, HFSS, hierarchical optimization, MATLAB, patch antenna.

I. INTRODUCTION

Modern programs for computer-aided design (CAD) are extremely useful tools for the design of complex structures. However, they are difficult to manage when they have to be interfaced with other software or when complex operations are necessary [1, 2].

In order to manage complex operations involving CAD software in a straightforward way, it is of paramount importance to be able to interface CAD software with a numeric computing environment (NCE). In the following, we refer to HFSS [3] and MATLAB [4].

The development of an HFSS-MATLAB interface is not new. It is described in [5–8], and a library for the interface between MATLAB and HFSS is available online [9]. In [1, 2], FEKO [10] is interfaced with MATLAB. Python has also been used recently to launch EM simulators [11, 12]. However, the mentioned works use the Visual Basic for Applications (VBA) scripting language to interface HFSS and MATLAB. VBA scripts require large libraries, since each feature in the HFSS model requires a specific command with a specific syntax. Then, even if HFSS commands can be recorded to a script exploiting a useful feature of HFSS [6], writing a script is a slow and tedious task, especially for beginners. Another possibility to interface HFSS and MATLAB is

to call the latter during the execution of the former. However, this interface is much less flexible than the one in which MATLAB drives HFSS. Not to be forgotten, students and experienced designers can feel pain when they have to learn a further programming language [13].

This paper presents and describes an improved and easy-to-implement HFSS-MATLAB interface that makes no use of VBA scripts. To achieve this goal, variables are updated in the ASCII file describing the HFSS model to simulate. Practical details are provided for the implementation of the application programming interface (API). Moreover, for easier reproducibility of the API, working examples are also available at [14]. Thanks to the API, there is no need to learn VBA to script HFSS. This CAD is then treated like a black box that returns the output of a simulation once it is called from MATLAB. The working principles of the API are presented in a practical example: the numerical design of a patch antenna resonating at 2 GHz.

II. DESIGN EXAMPLE

The example considered for illustrating the proposed interface is the numerical design of a rectangular patch antenna working at $f_0 = 2$ GHz. The substrate of the antenna is characterized by a height of 1.6 mm, a metallization thickness of 0.035 mm, and a relative dielectric constant of 2.2. The technical drawing of the proposed antenna is depicted in Fig. 1. The patch is characterized by a width W and a length L . The feed is a $\lambda/4$ transformer whose length is a . To have more degrees of freedom, the transformer has a trapezoidal shape whose bases are $M - 2b$ and $M - 2c$, where $M = 4.943$ mm, the width of the microstrip with a $50\ \Omega$ characteristic impedance. The distance between the patch and the sides of the substrate is $L_e = 8$ mm and the length of the $50\ \Omega$ microstrip is $L_m = 10$ mm. In the following, only parameters a , b , c , W , and L are variable, the others being constants.

An analytical design procedure for rectangular patch antennas is possible [15], and the values of the geometrical parameters for this design are listed in Table 1.

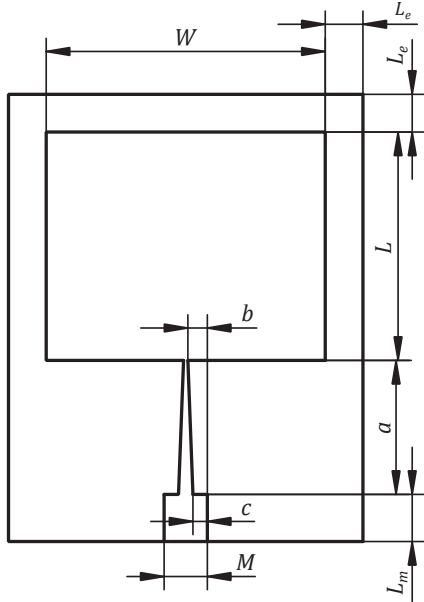


Fig. 1. Technical drawing of the patch antenna.

Table 1: Variable history (dimensions in millimeters, abbreviation a.a. stands for *as above*)

	Variables				
	L	W	a	b	c
Min	46	57	26	1.500	1.500
Max	50	61	32	2.370	2.370
Anal.	49.830	59.290	28.510	2.070	2.070
Opt. (i)	48.472	a.a.	a.a.	a.a.	a.a.
Opt. (ii)	a.a.	59.225	28.440	2.014	1.999

However, once the geometrical values from the analytical design are simulated, the antenna results do not match them at the desired working frequency, as shown in Fig. 2. The resonant frequency f_r (the frequency at which the minimum of the return loss occurs), the minimum of the return loss $|S_{11}|_m$ and the return loss at $f_0 = 2$ GHz, $|S_{11}(f_0)|$, are gathered in Table 2.

To have an antenna working at the desired frequency, an optimization is performed. Since the magnitude of the reflection coefficient is not a smooth function of the geometrical parameters [16], it is not wise to consider a unique goal for the optimization of the return loss. Then, the problem is tackled by means of a hierarchical optimization with these two goals:

$$\min_L (f_r - f_0)^2 \quad (1a)$$

$$\min_{a,b,c,W} |S_{11}|_m, \quad (1b)$$

where min stands for minimize. The reasons behind the definitions of these two optimizations derive from the theory of the problem. Indeed, it is known from theory

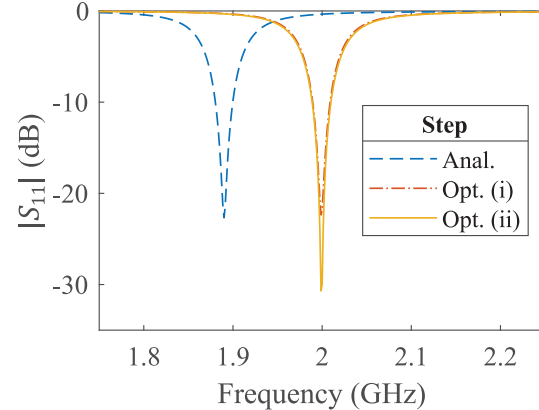
Fig. 2. Magnitude of S_{11} for the patch antenna during the different steps of the design.

Table 2: Result summary

Step	f_r (GHz)	$ S_{11} _m$ (dB)	$ S_{11}(f_0) $ (dB)
Anal.	1.890	-22.68	-0.35
Opt. (i)	1.999	-22.37	-21.83
Opt. (ii)	1.999	-30.70	-29.99

[15] that a) the resonant frequency depends *primarily* on the patch length, and b) matching depends *primarily* on the feed dimensions and patch width. Then the two optimizations of the hierarchical optimization are (1a) for point a and (1b) for point b. Note that while improving matching in (1b) we do not care about the resonant frequency of the antenna, assuming that it does not change remarkably. However, if the change in the resonant frequency after solving (1b) is remarkable, then optimization (1a) can be repeated to re-center the resonant frequency at the desired value.

For the above optimizations, the MATLAB optimization functions are *fminbnd* for (1a), and *fmincon* for (1b). Function *fminbnd* is especially useful for minimization problems with a single variable. As starting point for the hierarchical optimization, the analytical design is considered. The minimum and maximum values for the variables being optimized are listed in Table 1.

III. DESCRIPTION OF THE API

In the following, the filenames indicated in Table 3 are considered. Obviously, only the file extension must be the one indicated while the filename could be different, provided that all occurrences change accordingly.

The MATLAB commands are in *HFSS_API.m*. The HFSS model to simulate is *base.aedt*, while *base.txt* is the same as *base.aedt*, but with the variables substituted by univocal signposts. The file *modified.aedt* is the HFSS model to simulate with updated variables. Eventually,

Table 3: Files for the API

Filename	Description
<i>HFSS_API.m</i>	MATLAB script for the interface
<i>base.aedt</i>	Model to simulate
<i>base.txt</i>	Model with signposts
<i>modified.aedt</i>	Model with updated variables
<i>ExportToFile.py</i>	Python script for data extraction
<i>res.csv</i>	Exported results

ExportToFile.py is the Python script for the export of the results and *res.csv* the exported results.

The flow chart for the proposed API is presented in Fig. 3. The proposed API is made of steps to be done once, called *Preliminary steps*, and steps that have to be done before each simulation, called *Steps to be repeated*. The preliminary steps are done manually by the designer, while the API automatically performs the others. Furthermore, the blocks with rounded corners refer to the steps performed in MATLAB, while those without rounded corners to those of the API.

A. Preliminary steps

The preliminary steps are:

- build the model in HFSS and save it as *base.aedt*;
- copy the previous file and open it as a text file. Substitute the numerical values of the variables to be varied with unique character combinations ('signposts', one for each variable), and save the file as *base.txt*;
- generate the file *ExportToFile.py* to export the results of the simulation.

Since all setups are run by the command used to execute the simulations, the designer, while preparing the HFSS model, should follow these directions: a) insert only one design, called *Design* in the following; b) insert only the required setups.

Here is the part of file *base.txt* defining the variables of the design: the signposts inserted to substitute for the variables are shown in bold:

```
$begin 'Properties'
VariableProp('A', 'UD', "", '1A1Amm')
VariableProp('B', 'UD', "", '1B1Bmm')
VariableProp('a', 'UD', "", '2A2Amm')
VariableProp('b', 'UD', "", '2B2Bmm')
VariableProp('c', 'UD', "", '2C2Cmm')
VariableProp('ts', 'UD', "", '1.6mm')
VariableProp('tc', 'UD', "", '0.035mm')
VariableProp('Le', 'UD', "", '8mm')
VariableProp('Lm', 'UD', "", '10mm')
VariableProp('M', 'UD', "", '4.942869528525mm')
$end 'Properties'.
```

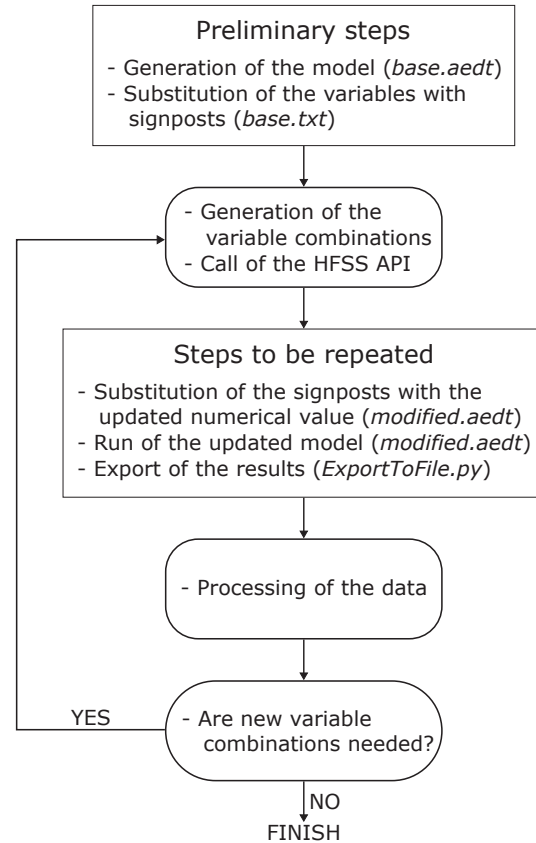


Fig. 3. Flow chart of the proposed API. The rectangles with rounded corners refer to the steps performed in MATLAB, while those without rounded corners relate to the proposed API.

Here is the Python file *ExportToFile.py* to export the results of the simulation:

```
oDesktop.RestoreWindow()
oProject = oDesktop.SetActiveProject("Modified")
oDesign = oProject.SetActiveDesign("Design")
oModule = oDesign.GetModule("ReportSetup")
oModule.UpdateReports(["S11mag"])
oModule.ExportToFile("S11mag", "res.csv"),
```

where *Design* is the name of the design in *modified.aedt* and *S11mag* is the name of the report displaying the results. The file *ExportToFile.py* could even be generated automatically in MATLAB.

B. Steps to be repeated

The steps to be repeated for each parameter combination request by the MATLAB script are:

- read file *base.txt* containing signposts, substitute each signpost with the numerical values indicated by the MATLAB script, and save the new file as *modified.aedt*;

- run file *modified.aedt* to simulate the model;
- run file *ExportToFile.py* to export results;
- read the results exported in file *res.csv*.

While substituting the numerical values with signposts, the designer must be aware of the right correspondence between the substituted variables and the actual variables in the model. Therefore, it is helpful to note a correspondence table while inserting the signposts. For example, after having substituted the numerical variables, the file *modified.aedt* appears as

```
$begin 'Properties'
VariableProp('L', 'UD', '', '48.47213595500mm')
VariableProp('W', 'UD', '', '59.22459629087mm')
VariableProp('a', 'UD', '', '28.44027653740mm')
VariableProp('b', 'UD', '', '2.013573376324mm')
VariableProp('c', 'UD', '', '1.999106250004mm')
VariableProp('ts', 'UD', '', '1.6mm')
VariableProp('tc', 'UD', '', '0.035mm')
VariableProp('Le', 'UD', '', '8mm')
VariableProp('Lm', 'UD', '', '10mm')
VariableProp('M', 'UD', '', '4.942869528525mm')
$end 'Properties'
```

The MATLAB command that executes a string in the command window is *system(StringToExecute)*. The string for simulating the HFSS model is

```
"PathExe\ansysedt.exe" /Ng /BatchSolve
"Path\modified.aedt",
```

while the string for exporting the results is

```
"PathExe\ansysedt.exe" /Ng /BatchExtract
"Path\ExportToFile.py" "Path\modified.aedt",
```

where *ansysedt.exe* is the executable for HFSS, *PathExe* is the folder where the executable file *ansysedt.exe* is stored, */Ng* is the setting enabling the non-graphical mode, and *Path* is the folder where the files listed in Table 3 are saved.

IV. RESULTS

After running optimizations (1a) and (1b), the results for the reflection coefficient are presented in Fig. 2, and the values of the variables are listed in Table 1. Data summarizing the optimization are gathered in Table 2.

We note that it is sufficient to operate only on the length of the patch to have it resonating at the desired frequency. Additionally, optimization (1b) on the other parameters successfully improves matching without affecting the resonant frequency. Eventually, the first optimization requires only 2 function evaluations while the second requires 13, thus proving the effectiveness of the hierarchical optimization over indiscriminate global optimization algorithms like genetic ones [17, 18].

V. CONCLUSIONS

A useful interface between a CAD software, HFSS, and a software for technical computing, MATLAB, is outlined. Unlike other approaches performing the same task, the proposed one makes no use of VBA scripts to drive HFSS, hence being easier to implement and allowing the execution of simulations in non-graphical mode.

A glance into the interesting features enabled by this interface is provided by means of an example: the tuning of a resonant patch antenna. Despite this rather simple problem, it shows how the proposed API interface can realize complex procedures. Indeed, without the API, the designer would launch the different optimizations manually, with a high risk of errors and the need to keep up with the execution. On the contrary, with the proposed API, all steps of the hierarchical optimization can be handled automatically in MATLAB with much more flexibility.

Even though this interface is developed to drive HFSS, its working principles are of general validity and can be adapted to drive other simulators or software. For instance, the author applied the proposed method to drive GPT [19], a code for particle simulations.

Here what we learned from this lesson. Firstly, for the happiness of many, there is no need to learn VBA. Secondly, despite the computation capabilities we are experiencing nowadays, a good knowledge of the theory behind what we are studying is fundamental. The analyzed example shows how a hierarchical optimization approach can tune a patch antenna with only few 3D full-wave simulations.

ACKNOWLEDGEMENTS

The author thanks Prof. Pelosi for having prompted him to publish a single-author paper and to Eng. Maddio for having verified the proposed interface with more complex designs. The author is grateful also to Prof. Scleri and Eng. Righini for hints on how to run HFSS simulations from the command window. All acknowledged persons are from the University of Florence.

REFERENCES

- [1] R. L. Haupt, "Using MATLAB to control commercial computational electromagnetics software," *Applied Computational Electromagnetics Society (ACES) Journal*, vol. 23, no. 1, pp. 98-103, 2008.
- [2] A. Farahbakhsh, D. Zarifi, and A. Abdolali, "Using MATLAB to model inhomogeneous media in commercial computational electromagnetics software," *Applied Computational Electromagnetics Society (ACES) Journal*, vol. 30, no. 9, pp. 1003-1007, 2015.
- [3] "Ansys — Engineering Simulation Software." [Online] Available: <https://www.ansys.com/>, 2022.

- [4] “MathWorks,” [Online] Available: <https://www.mathworks.com/>, 2022.
- [5] Q. Tan, K. Fan, W. Yang, and G. Luo, “Low side-lobe series-fed patch planar array with AMC structure to suppress parasitic radiation,” *Remote Sensing*, vol. 14, no. 15, p. 3597, 2022.
- [6] I. Bouchachi, “Microstrip antenna synthesis using an application programming interface,” *Journal of Mechanics of Continua and Mathematical Sciences*, vol. spl1, no. 4, 2019.
- [7] J. B. Romdhane Hajri, D. Inserra, W. Gu, W. Hu, Y. Huang, J. Li, and G. Wen, “Fast and automatic RF design based on MATLAB-HFSS control applied on magnetic absorber with metasurface,” in *2019 Photonics and Electromagnetics Research Symposium - Fall, PIERS - Fall 2019 - Proceedings*, 2019.
- [8] X. Yuan, Z. Li, D. Rodrigo, H. S. Mopidevi, O. Kaynar, L. Jofre, and B. A. Cetiner, “A parasitic layer-based reconfigurable antenna design by multi-objective optimization,” *IEEE Transactions on Antennas and Propagation*, vol. 60, no. 6, 2012.
- [9] V. Ramasami, “HFSS-API,” [Online] Available: <https://github.com/yuip/hfss-api>, 2020.
- [10] “FEKO,” [Online] Available: <https://www.altair.com/feko>, 2023
- [11] C. Fang, S. Xinyang, and X. Zeng, “Using Python to launch electromagnetic scattering simulation with FEKO,” in *2021 13th International Symposium on Antennas, Propagation and EM Theory (ISAPE)*, pp. 1-3, IEEE, 2021.
- [12] R. J. Sánchez-Mesa, D. M. Cortés-Hernández, J. E. Rayas-Sánchez, Z. Brito-Brito, and L. De La Mora-Hernández, “EM parametric study of length matching elements exploiting an ANSYS HFSS MATLAB-Python driver,” in *2018 IEEE MTT-S Latin America Microwave Conference, LAMC 2018 - Proceedings*, 2018.
- [13] N. Shrestha, C. Botta, T. Barik, and C. Parnin, “Here we go again: Why is it difficult for developers to learn another programming language?” in *Proceedings of the ACM/IEEE 42nd International Conference on Software Engineering*, pp. 691-701, 2020.
- [14] G. Giannetti, “Gianne97/HFSS-MATLAB-API - without-VBA-scripts: HFSS-MATLAB API without VBA scripts - publication,” [Online] Available: <https://doi.org/10.5281/zenodo.8068428>, 2023.
- [15] C. A. Balanis, *Antenna Theory: Analysis and Design, Fourth Edition*, John Wiley & Sons, 2016.
- [16] S. Selleri, S. Manetti, and G. Pelosi, “Neural network applications in microwave device design,” *International Journal of RF and Microwave Computer-Aided Engineering*, vol. 12, no. 1, 2002.
- [17] D. Goldberg, *Genetic Algorithms in Search, Optimization, and Machine Learning*, Addison Wesley Series in Artificial Intelligence, Addison-Wesley, 1989.
- [18] L. Tarricone, “A genetic approach for the efficient numerical analysis of microwave circuits,” *Applied Computational Electromagnetics Society (ACES) Journal*, pp. 87-93, 2000.
- [19] “GPT,” [Online] Available: <https://www.pulsar.nl/gpt/>, 2023.



Giacomo Giannetti (ACES Student Member and IEEE Graduate Student Member) received the B.Sc. degree (cum laude) in electronic and telecommunications engineering from the University of Florence, Florence, Italy, in 2019, and the M.Sc. degree (cum laude) in electronic engineering from the Sapienza University of Rome, Rome, Italy, in 2021, with award as excellent graduate. He is currently working toward a Ph.D. degree in electromagnetism with the University of Florence. He spent a period as a student with the Technical University of Vienna, Vienna, Austria, and the National Laboratory of Frascati, Rome, Italy and a period as a Research Guest with Kiel University, Kiel, Germany. His research interests include microwave devices and computational electromagnetics.

Mutual Coupling Compensation-based Nonuniform Fourier Transform Technique for Accurate and Efficient Pattern Evaluation and its Application to Synthesis of Aperiodic Arrays

Fan Peng¹, Cheng Liao¹, You-Feng Cheng¹, Ju Feng¹, and Si-Du Wang²

¹Institute of Electromagnetics
Southwest Jiaotong University, Chengdu, 610031, China
pfan2023@my.swjtu.edu.cn, c.liao@swjtu.edu.cn, juvencheng@swjtu.edu.cn, fengju-fj@swjtu.edu.cn

²Mianyang Flight College of Civil Aviation
Flight University of China, Mianyang, 621000, China
1075972066@qq.com

Abstract – A rapid solution for evaluating the radiation pattern of aperiodic arrays, taking into account mutual coupling, is presented in this paper. The evaluation is achieved by eliminating the anisotropy of the active element pattern of the array through the use of the mutual coupling compensation matrix (MCCM) technique, in conjunction with the non-uniform fast Fourier transform (NuFFT). In order to eliminate the impact of mutual coupling on array pattern calculation, the MCCM is utilized to convert the active element pattern (AEP) of each element into a shared uniform term and make the NuFFT technique suitable for the array pattern calculation. The proposed solution is validated by evaluating the radiation pattern of a 64-element planar aperiodic array. In addition, the proposed solution is integrated into the Particle Swarm Optimization (PSO) to realize a pattern synthesis method. Two synthesized patterns, including a pencil beam with low sidelobe level and a flat-top beam pattern, are executed to validate. Compared with several reported methods, the proposed method can improve the synthesis efficiency and maintain good accuracy simultaneously.

Index Terms – aperiodic array, mutual coupling compensation, non-uniform fast Fourier transform, radiation pattern calculation and synthesis.

I. INTRODUCTION

Compared with periodic arrays, aperiodic arrays have attracted much attention in recent years because of several excellent advantages, such as suppression of grating lobes, reduction of cost and high degree of freedom in design [1]. However, the diversity of mutual coupling (MC) introduced by the aperiodic layout results in inaccurate evaluation of the radiating pattern. Besides, due to the aperiodic layout, some efficient synthesis solutions, such as the iterative Fourier transform (IFT) technique

[2], are no longer applicable. In published literature, the aperiodic array is usually transformed to a periodic one by embedding an amount of virtual elements to realize the accurate evaluation and fast synthesis. In [3], a virtual uniform array is established, and the element in the real aperiodic array is interpolated by several adjacent elements in the virtual one. In this situation, it is convenient to realize the fast synthesis of the aperiodic array by applying the IFT technique. However, the MC is not considered in the synthesis. You, et al. [4] proposed a concept of active element pattern expansion (AEPE) method and realized the fast synthesis of uniformly-spaced linear array. Inspired by the above AEPE and virtual uniform array, Liu, et al. [5] further presented a novel virtual active element pattern expansion method (VAEPE) and integrated it with the IFT procedure, resulting in a fast synthesis of aperiodic arrays including the MC. Nevertheless, these methods often dramatically increase the size strong of the array, which results in high complexity.

In contrast to the above methods, the fast synthesis of aperiodic arrays also can be directly accomplished by the non-uniform fast Fourier transform (NuFFT) technique [6–10]. The NuFFT technique, in which a variety of uniform sampling with a denser grid is generated, is the expansion of the fast Fourier transform (FFT) technique [11–14]. The time complexity of pattern evaluation is reduced successfully to $O(N \log N)$ from $O(N^2)$. Therefore, it can be integrated into many pattern synthesis methods, such as the stochastic optimization algorithms [15, 16], convex optimization technique [17] and other solutions [18–20] to improve the synthesis efficiency. In [15], the NuFFT technique based on Gaussian interpolation is chosen to reduce optimization time of the aperiodic array. However, those methods are only suitable for the ideal array, which means each element of the

array is seen as an isotropic source and MC is not taken into consideration. In fact, the MC has crucial influences on the radiation pattern of aperiodic array, especially when patterns with low sidelobe level (SLL) and specific nulls are required. To date, realizing the accurate evaluation and fast synthesis of aperiodic arrays is still a strong challenge in the area of phased arrays.

In this paper, an improved NuFFT-based solution to calculate and synthesize the far-field pattern of arbitrary aperiodic arrays is proposed and analyzed. Firstly, the mutual coupling compensation matrix (MCCM) [21–23] is utilized to approximate each active element pattern (AEP) to a far-field pattern of the array without the consideration of MC with compensated excitation. On this basis, the isolated element pattern (IEP) can be extracted outside of the summation of the array pattern. Then, the NuFFT is introduced to form a novel fast pattern evaluation method and accelerate the calculation process. A numerical example of a 64-element planar aperiodic array is chosen to validate the proposed solution. Afterwards, the above solution is integrated into Particle Swarm Optimization (PSO) to replace the conventional pattern multiplication method (PMM) for the radiation pattern synthesis of aperiodic arrays. Two synthesized patterns including a pencil beam with low sidelobe level and a flat-top beam pattern of two linear aperiodic arrays are realized with amplitude and phase weighting, which results indicate that the proposed method can improve the synthesis efficiency and maintain high accuracy simultaneously compared with several reported methods.

II. MC COMPENSATION-BASED NUFFT TECHNIQUE

Without loss of generality, let us consider a planar array composed of N elements which are arbitrarily located in the xoy -plane. The position of the n -th element is denoted as (x_n, y_n) . If MC or edge effect is neglected, the ideal radiation pattern (IRP) of the array can be described as the product of the array factor (AF) and IEP by PMM:

$$\begin{aligned} P_i(\theta, \varphi) &= E_{i0}(\theta, \varphi) \cdot \left(\sum_{n=1}^N w_i^n e^{jk(x_n u + y_n v)} \right) \\ &= \sum_{n=1}^N w_i^n \left(E_{i0}(\theta, \varphi) e^{jk(x_n u + y_n v)} \right) \\ &= \mathbf{E}_i \mathbf{W}_i, \end{aligned} \quad (1)$$

with

$$\mathbf{E}_i = \begin{bmatrix} E_{i0}(\theta, \varphi) e^{jk(x_1 u + y_1 v)} \\ \vdots \\ E_{i0}(\theta, \varphi) e^{jk(x_N u + y_N v)} \end{bmatrix}^T \quad \mathbf{W}_i = \begin{bmatrix} w_i^1 \\ \vdots \\ w_i^N \end{bmatrix}, \quad (2)$$

where w_i^n is the n -th ideal element excitation of the array, E_{i0} is the IEP of the array element, k is the free space

wavenumber at operation frequency, $u = \sin \theta \cos \varphi$, $v = \sin \theta \sin \varphi$ separately and (θ, φ) are the observation direction defined by standard spherical coordinate, the notation “ $(\cdot)^T$ ” is the transpose operator. It is apparent that the Fourier transform-pair relationship exists between AF and array excitation, which means $P_i(\theta, \varphi)$ can be calculated quickly by using the NuFFT technique.

On the contrary, when the MC effect is taken into consideration, the actual radiation pattern (ARP) of the array $P_r(\theta, \varphi)$ can be given by the AEP method (AEPM) [24] as follows:

$$\begin{aligned} P_r(\theta, \varphi) &= \sum_{n=1}^N w_r^n E_r^n(\theta, \varphi) \\ &= \mathbf{E}_r \mathbf{W}_r, \end{aligned} \quad (3)$$

with

$$\mathbf{E}_r = \begin{bmatrix} E_r^1(\theta, \varphi) \\ \vdots \\ E_r^N(\theta, \varphi) \end{bmatrix}^T \quad \mathbf{W}_r = \begin{bmatrix} w_r^1 \\ \vdots \\ w_r^N \end{bmatrix}, \quad (4)$$

where w_r^n is the actual excitation of the n -th element, E_r^n is the AEP corresponding element n . Note that all of the array elements are placed in a common and unique coordinate system. Because of the MC of the array, the AEPs are different from each other, which results in the calculation of $P_r(\theta, \varphi)$ only relying on the summation of AEPs of all elements. In this case, the NuFFT technique is not applicable.

In general, the pattern is evaluated by formula (1) in the pattern synthesis program. After being synthesized, the excitation \mathbf{W}_i is used in the real array analysis. It is obvious that a distorted radiation pattern $P_r(\theta, \varphi)$ with respect to the ideal synthesized pattern $P_i(\theta, \varphi)$ is obtained. Therefore, a method to make the IRP fit to the ARP in whole space and which has the ability to use the FFT/NuFFT technique is needed. To this end, the MCCM is introduced.

The method for solving MCCM of uniform arrays had been reported in [22], and it is further introduced and improved here for non-uniform arrays. Specifically, for the purpose of making the ARP $P_r(\theta, \varphi)$ and the IRP $P_i(\theta, \varphi)$ as similar as possible, the least square method is adopted, the maximum similarity between $P_r(\theta, \varphi)$ and $P_i(\theta, \varphi)$ can be expressed as:

$$\min \iint |P_r(\theta, \varphi) - P_i(\theta, \varphi)|^2 \sin \theta d\theta d\varphi, \quad (5)$$

the above integration will be carried out in visible space to obtain a minimum mean square error and can be rewritten into the following matrix form:

$$\min_{\mathbf{W}_i} \mathbf{W}_r^H \mathbf{Q} \mathbf{W}_r - \mathbf{W}_i^H \mathbf{P}^H \mathbf{W}_r - \mathbf{W}_r^H \mathbf{P} \mathbf{W}_i + \mathbf{W}_i^H \mathbf{C} \mathbf{W}_i, \quad (6)$$

where \mathbf{Q} , \mathbf{P} and \mathbf{C} all are $N \times N$ matrices, which can be calculated by the following formulas:

$$\begin{aligned}\mathbf{Q} &= \iint \mathbf{E}_r^H \mathbf{E}_r \sin \theta d\theta d\varphi, \\ \mathbf{P} &= \iint \mathbf{E}_r^H \mathbf{E}_i \sin \theta d\theta d\varphi, \\ \mathbf{C} &= \iint \mathbf{E}_i^H \mathbf{E}_i \sin \theta d\theta d\varphi.\end{aligned}\quad (7)$$

Furthermore, the solution of (6) is derived as:

$$\mathbf{W}_i = \mathbf{P}^{-1} \mathbf{Q} \mathbf{W}_r. \quad (8)$$

Thus, the MCCM \mathbf{C} is written as:

$$\mathbf{C} = \mathbf{P}^{-1} \mathbf{Q}. \quad (9)$$

Since \mathbf{C} defines a relation between \mathbf{W}_r and \mathbf{W}_i , the compensated excitation enables the calculated array pattern in (1) to maintain the maximum approximation to the ARP. In this situation, $P_r(\theta, \varphi)$ can be easily rewritten as:

$$P_r(\theta, \varphi) = \mathbf{E}_r \mathbf{W}_r \approx \mathbf{E}_i \mathbf{W}_i = \mathbf{E}_i (\mathbf{C} \mathbf{W}_r), \quad (10)$$

where $\mathbf{C} \mathbf{W}_r$ is seen as the compensated excitation. It can be seen from (10) that the consideration of MC is shifted from AEPs to excitation term which is easier to deal with. The reason why the symbol ‘ \approx ’ holds is that the least squares equation in (5) just merely guarantees the approximation. Note that the approximation is able to provide the sufficient computational accuracy, which can be proved by the subsequent comparisons between the results of the numerical calculation and full-wave simulation. Substituting (10) for (1), the approximation of ARP would be easily achieved and given by:

$$P_r(\theta, \varphi) \approx E_{i0}(\theta, \varphi) \cdot \sum_{n=1}^N \left(\sum_{m=1}^N c_{nm} w_r^m e^{jk(x_m u + y_m v)} \right), \quad (11)$$

where the c_{nm} is the (n, m) -th term of \mathbf{C} . This term represents the compensation of m -th element on the n -th element of array due to the coupling. It can be observed from (10) and (11) that the calculation of $P_r(\theta, \varphi)$ is replaced by the calculation of $P_i(\theta, \varphi)$ with excitation $\mathbf{C} \mathbf{W}_r$, and the far-field calculation obeys the principle of pattern multiplication again. In other words, the ARP $P_r(\theta, \varphi)$ can be represented by the IEP and the AF, the AF here is:

$$AF = \sum_{n=1}^N \left(\sum_{m=1}^N c_{nm} w_r^m e^{jk(x_m u + y_m v)} \right). \quad (12)$$

Obviously, the Fourier transform-pair relationship exists between AF and compensated excitation $\mathbf{C} \mathbf{W}_r$, therefore the NuFFT technique can be applied to accelerate the calculation. In addition, when w_r^n in (11) equals 1, the AEP of the n -th array element $E_r^n(\theta, \varphi)$ is approximated by:

$$E_r^n(\theta, \varphi) \approx E_{i0}(\theta, \varphi) \cdot \left(\sum_{m=1}^N c_{nm} e^{jk(x_m u + y_m v)} \right). \quad (13)$$

From (13), the AEP of each element can be seen as a synthesized pattern with excitation of $c_{n,1:N}$. The time complexity of the PMM in (1) is $O(MN)$, and that of (11) drops to $O(M \log M)$ by introducing the NuFFT with M sampling points [10]. In this way, the efficiency of the calculation of $P_r(\theta, \varphi)$ is significantly enhanced.

An example is provided to verify the effectiveness of the MCCM-NuFFT solution. A two-dimensional (2-D) planar array, which is composed of 64 rectangle patch antenna shown in Fig. 1 (a) and operates at 5 GHz, is selected and the array layout is drawn in Fig. 1 (b). Figure 2 shows the comparison between the AEP and the approximative element pattern of the center element (29-th) obtained by Ansys HFSS and MCCM-NuFFT solution respectively, the IEP of the antenna element is given simultaneously. As observed, the AEP is quite different with the IEP due to the MC, a serious distortion about 5 dBV/m of E-field generated in the broadside direction from the Fig. 2 (b). In addition, the main beam direction has been changed. On the contrary, the approximative element pattern obtained by the MCCM-NuFFT method is nearly similar to the original AEP, which can fit well the curve of the original AEP in most angular ranges. Only when θ is greater than 80° do the difference of the

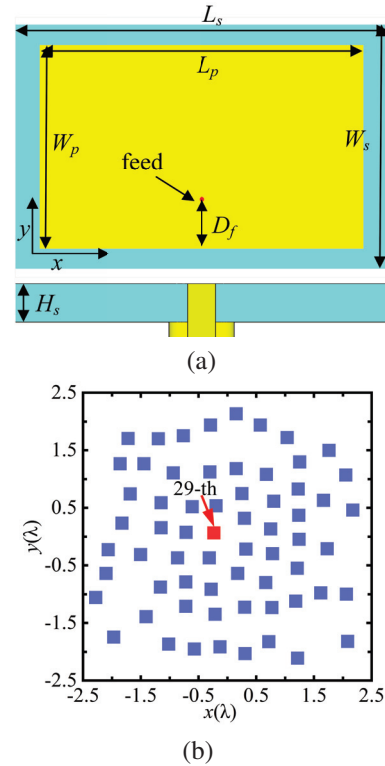


Fig. 1. (a) The geometry of the antenna element. (b) The array layout. (b) $W_s=27.6$ mm, $L_s=22.08$ mm, $W_p=23$ mm, $L_p=18.4$ mm, $D_f=6$ mm, $H_s=2$ mm.

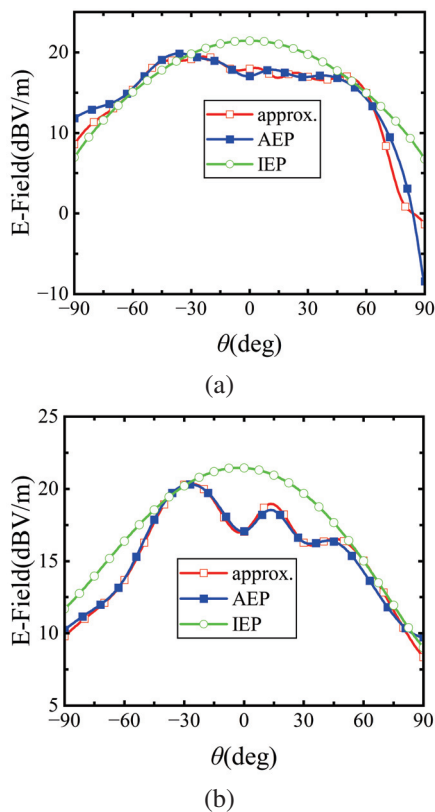


Fig. 2. The compensated pattern of 29-th element (a) xoz -plane, (b) $yo z$ -plane.

curves slightly increase. Figure 2 demonstrates that the distortion pattern of the array element caused by the MC can be compensated well by the MCCM.

In addition, Fig. 3 illustrates the top view of the 3D normalized radiating pattern of the aperiodic array using several methods. Figure 4 provides the 2D patterns of both the xoz and $yo z$ planes. The simulated pattern obtained by Ansys HFSS in Fig. 3 (a) serves as a benchmark to compare the accuracy of the two methods. As observed in Fig. 3 (b), the pattern generated by the MCCM-NuFFT method closely matches the simulated result. The main performance parameters of the array, such as the realized gain and peak sidelobe level (PSL), agree well with the simulated values. Only minor deviations exist in the high-elevation area. This discrepancy can be attributed to the fact that the approximation is conducted across the entire space. Consequently, errors of the same magnitude can manifest as larger relative differences in smaller simulated results expressed in decibels (dB) [25]. Conversely, the pattern obtained by the PMM method exhibits greater differences. While good approximation is maintained in the mainbeam area, noticeable discrepancies arise in the sidelobe regions. Additionally, the 2D pattern in Fig. 4 reveals a degradation in sidelobe

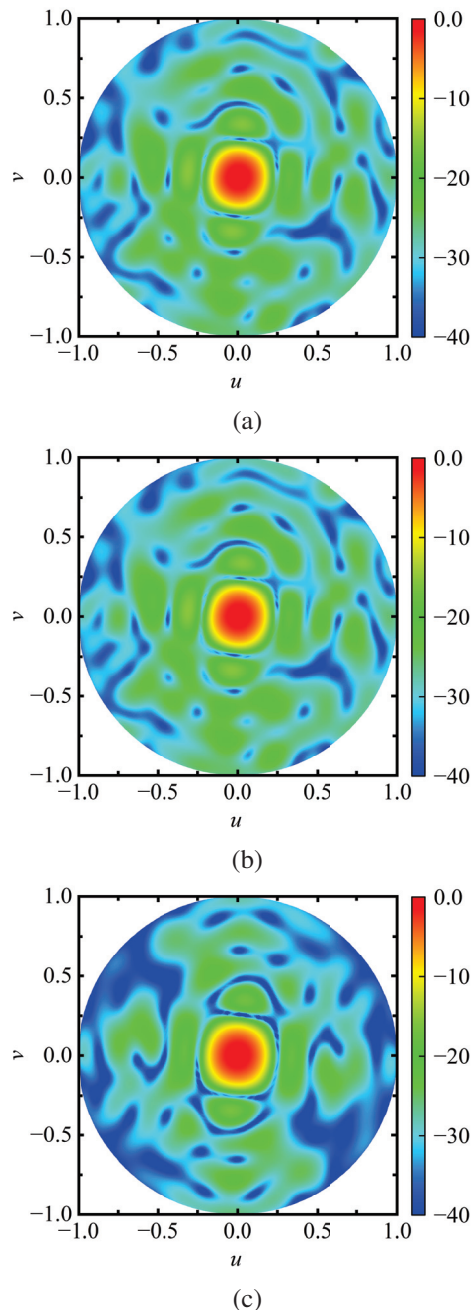


Fig. 3. The normalized radiated pattern of planar 64-element 2-D planar array with different methods, (a) pattern based on Ansys HFSS, (b) pattern based on MCCM-NuFFT, (c) pattern based on PMM.

levels of up to 5 dB, along with changes in null positions. It is evident that the lack of consideration for mutual coupling is the reason behind these discrepancies. These results demonstrate that the proposed method effectively incorporates mutual coupling in the evaluation process of the array pattern.

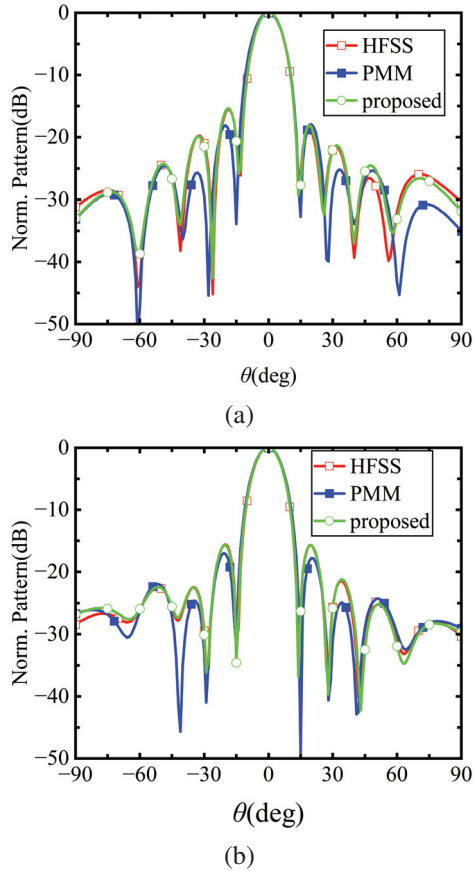


Fig. 4. The normalized 2D radiating pattern of 64-element 2-D planar array in different methods, (a) xoz -plane, (b) $yozy$ -plane.

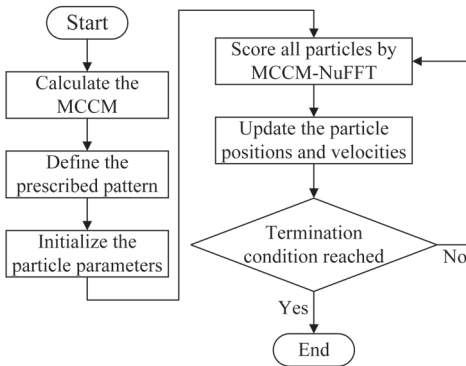


Fig. 5. The flowchart of proposed synthesis method.

III. FAST SYNTHESIS AND VALIDATION

A. Description of synthesis method

Based on the superiority of efficiency and accuracy, the MCCM-NuFFT method is integrated into the PSO to form a synthesis procedure in this section. The PSO algorithm has been applied to different electromagnetic

applications such as array pattern synthesis [26, 27], and antenna design [28] because of the flexible constraints and its robustness to real-world problems. The corresponding flowchart is shown in Fig. 4, a brief description of this procedure is shown as follows:

- Calculate MCCM C : obtain the AEP and the IEP of the predefined array by simulation or measurement. The MCCM C can be calculated by the method presented in section II and the reference [22].
- Define the prescribed pattern: define the mainlobe region, sidelobe region, and PSL. If the target pattern is a shaped pattern, the lower and upper boundaries of the shaped region must be set up.
- Initialize the particle position vector X of Q random individuals for amplitude-phase optimization. A set of random velocities V is also initialized between v_{min} and v_{max} .
- Score all particles: evaluate the pattern including MC effect of each particle using the above MCCM-NuFFT method. Record the global optimal particle p_g and local optimal particles P_l of each particle separately.
- Update the positions and velocities of particles.
- Check if the optimal pattern meets the requirement. If yes, the synthesis procedure would be stopped, or go back to step (d) before going up to the maximum iteration number.

It is obvious that the fitness value of each particle corresponding to a solution must be evaluated in the iteration process. Therefore, equation (1) based on PMM needs QMN complex summations while the proposed MCCM-NuFFT method only requires $QM \log M$ because the NuFFT is available. This means the cost time is significantly saved while the accuracy can be maintained simultaneously. Two pattern synthesis examples are executed to verify the performance improvement on efficiency and accuracy of the proposed modified PSO method.

B. Focused beam pattern synthesis

In the first example, a focused beam of a 16-element linear array with reduced sidelobe is synthesized. The proposed modified PSO method and the PSO solution in [26] are compared to synthesize the same pattern simultaneously by optimizing the excitation amplitudes and phases. For the proposed method, the array element is assumed to be the microstrip antenna shown in Fig. 1 (a), while the array element is set as the isotropic source in the PSO method. The element positions and excitations are given in Fig. 6. The synthesized patterns of the proposed modified PSO method and the PSO solution in [26] are both shown in Fig. 7.

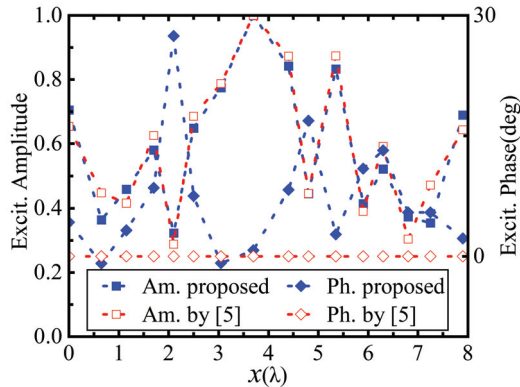


Fig. 6. The optimized excitation of 16-element linear array by two methods.

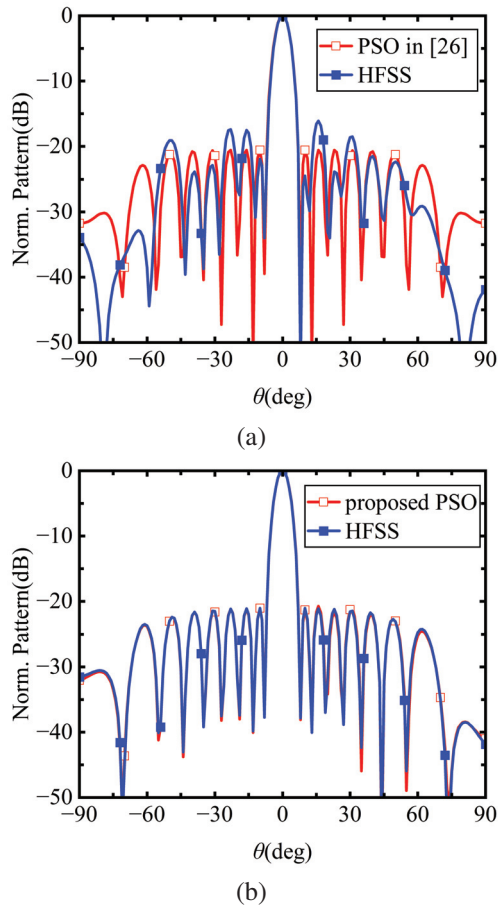


Fig. 7. The normalized pattern of 16-element linear array by (a) PSO in [26] and (b) proposed modified PSO method.

As can be seen, sidelobe levels lower than -21 dB are both obtained by two synthesized methods. However, when excitation amplitudes and phases are applied

to the 16-element array, significant deteriorations occur on the corresponding simulated pattern shown in Fig. 7 (a), the PSL reaches to -16 dB and the simulated pattern in the high-elevation areas vary sharply compared to the synthesized one. That means the solution reported in [26] may encounter some difficulties when it is used to synthesize a scanning beam. By contrast, the difference between patterns realized by the proposed method can be neglected. As plotted in Fig. 7 (b), the PSL remains as -21 dB. It is noted that the accurate synthesized pattern can also be obtained by AEPM. However, the calculation time would be increased because AEPs of array elements are quite different, which results in low synthesis efficiency. Besides, the subsequent time-consuming analysis also proves this point.

C. Flat-top beam pattern synthesis

A numerical experiment is performed and analyzed here to show the superiority in accuracy and efficiency of the proposed synthesis procedure. The experiment is going to synthesize a flat-top beam pattern of a linear aperiodic array composed of 12 dipole antennas by using amplitude-phase optimization, the dipole which works at central frequency of 1 GHz is designed to have a length of 144 mm and a radius of 1.5 mm. The desired pattern was achieved previously in [29] with the aperiodic array composed of 12 isotropic elements by the forward-back matrix pencil method. Then, the similar pattern including MC effect was also realized in [5] by utilizing the IFT method based on the VAEPE method.

The optimized compensated excitation, including the amplitudes and phases, are shown in Fig. 8, the corresponding actual excitation transformed by MCCM is also given. It reveals that the compensated excitation is similar to the actual ones. The difference of excitation amplitudes only emerges on elements on either sides, and the amplitudes of middle elements basically remain unchanged. In terms of excitation phases, they all differ from the original excitation ones. This phenomenon

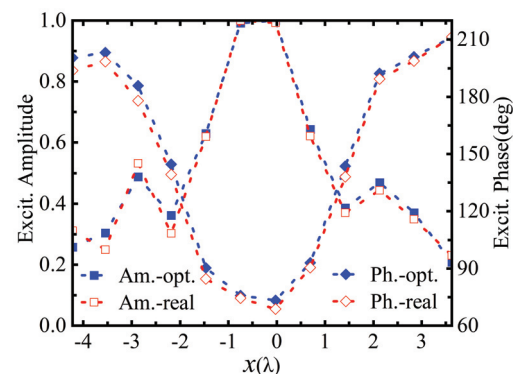


Fig. 8. The optimized and actual excitation.

suggests that excitation phases derive more influences of MC in this synthesis.

The synthesized patterns are shown in Fig. 9 which also includes patterns obtained by real AEPs and the solutions reported in [5] and [29]. It is obvious that all synthesized patterns obtained by these methods fully satisfy the pre-defined constraints. However, the corresponding simulated pattern, which is obtained when the optimized excitation given in [29] applies to the practical

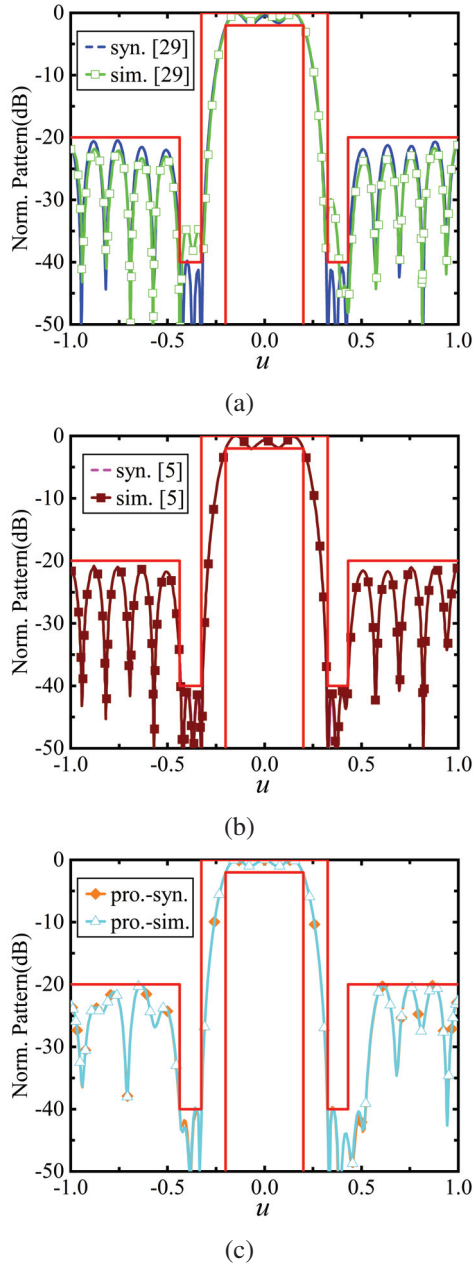


Fig. 9. The flat-top beam patterns of the 12-element dipole array obtained by several solutions, (a) result from [29], (b) result from [5], (c) result from proposed.

array, has some deterioration when compared with the synthesized one, especially in the -40 -dB null regions. This indicates that the synthesized excitation obtained by common optimization cannot achieve the desired pattern with the actual array design. In terms of the pattern obtained by the proposed procedure, it can be seen that the synthesized pattern has a good agreement with the simulated result, which demonstrates that the MC effect can be considered well during the synthesis. Good agreement is also obtained between the synthesized pattern and the actual one with the optimized excitation in [5]. Nevertheless, the virtual array excitation of each real AEP requires a matrix inverse operation, which is time consuming, resulting in the high complexity of the VAEPE method.

Furthermore, the computational time of the proposed solution represented in Table 1 is recorded to analyze the efficiency improvement as well as the results based on the AEPM defined in (2). It should be noted that, since patterns obtained by PMM are not accurate enough, two methods including AEPM and the proposed MCCM-NuFFT are compared and analyzed here. All numerical computations are carried out by 100 trials on an Intel(R) Core (TM) i5-8600k 3.6 GHz CPU, 16 GB RAM computer with MATLAB platform. From Table 1, the computational time of the proposed solution shows some advantages. For instance, when the 64-element 2-D planar array in section II is selected, the computational time of the MCCM-NuFFT solution only takes 0.56 s while the AEPM of (2) requires 4.98 s with 256×256 spatial sampling points. In addition, the computational time quickly grows with the number of spatial sampling and array size for the AEPM. That means the advantages would be magnified synchronously with the increase of the number of the spatial sampling and array size. A similar conclusion can be obtained in other related literature about NuFFT.

Finally, the computational time of the method in [5] is negligible due to the introduction of the FFT. Nevertheless, the indispensable calculation of related coefficients greatly reduces the efficiency of the algorithm. For example, when the example of 64-element 2-D planar

Table 1: The computational time of proposed method and AEPM (unit: s)

Array Type		Sampling Number			
		256	512	1024	2048
12-ele. array	AEPM	0.0102	0.0145	0.0173	0.0371
	Proposed	0.0113	0.0124	0.0156	0.022
16-ele. array	AEPM	0.0131	0.0178	0.0216	0.0457
	Proposed	0.0127	0.0131	0.0151	0.026
64-ele. array	AEPM	4.98	19.88	75.8	293.18
	Proposed	0.56	1.53	4.7	18.6

array is addressed, the computational time of excitation of virtual array in the first time is about 1300 s, whereas only 0.3 s is required for the proposed solution. The reason for high efficiency of the proposed solution is because the number of array elements has not increased, MC is compensated only by adjusting the excitation. The time comparison indicates that the proposed solution also has the advantages of simplicity and ease of implementation.

IV. CONCLUSION

In this paper, based on the utilization of the NuFFT technique and MCCM, a rapid solution for calculating the radiation pattern of aperiodic arrays when MC effects are taken into consideration, is presented. By compensating the excitation with the MCCM technique, the impacts of MC on the element radiation can be compensated. Furthermore, the NuFFT technique is introduced to accelerate the array pattern calculation. The proposed solution is validated by evaluating the radiation pattern of a planar aperiodic array. In addition, the proposed solution is integrated easily into the PSO algorithm to realize the fast pattern synthesis of aperiodic arrays. Two pattern synthesis examples, including focused beam and flat-top beam patterns with different array numbers, are realized, which indicates that the proposed method can improve the synthesis efficiency and maintain good accuracy simultaneously.

ACKNOWLEDGMENTS

This work was supported in part by the National Natural Science Foundation of China (Grant No. 62271416), and the Natural Science Foundation of Sichuan Province (Grant No. 2022NSFSC0494).

REFERENCES

- [1] G. Toso and R. Mailloux, "Guest editorial for the special issue on innovative phased array antennas based on non-regular lattices and overlapped sub-arrays," *IEEE Transactions on Antennas and Propagation*, vol. 62, no. 4, pp. 1546-1548, 2014.
- [2] Y.-F. Cheng, W. Shao, S.-J. Zhang, and Y.-P. Li, "An improved multi-objective genetic algorithm for large planar array thinning," *IEEE Transactions on Magnetics*, vol. 52, no. 3, pp. 1-4, 2016.
- [3] K. Yang, Z. Q. Zhao, and Q. H. Liu, "Fast pencil beam pattern synthesis of large unequally spaced antenna arrays," *IEEE Transactions on Antennas and Propagation*, vol. 61, no. 2, pp. 627-634, 2013.
- [4] P. F. You, Y. H. Liu, X. Huang, L. Zhang, and Q. H. Liu, "Efficient phase-only linear array synthesis including coupling effect by GA-FFT based on least-square active element pattern expansion method," *Electronics Letters*, vol. 51, no. 10, pp. 791-792, 2015.
- [5] Y. H. Liu, X. Huang, K. D. Xu, Z. Y. Song, S. W. Yang, and Q. H. Liu, "Pattern synthesis of unequally spaced linear arrays including mutual coupling using iterative FFT via virtual active element pattern expansion," *IEEE Transactions on Antennas and Propagation*, vol. 65, no. 8, pp. 3950-3958, 2017.
- [6] D. R. Prado, M. Arrebola, M. R. Pino, and F. Las-Heras, "An efficient calculation of the far field radiated by non-uniformly sampled planar fields complying Nyquist theorem," *IEEE Transactions on Antennas and Propagation*, vol. 63, no. 2, pp. 862-865, 2015.
- [7] O. Bucci and M. Migliore, "A novel nonuniform fast Fourier transform algorithm and its application to aperiodic arrays," *IEEE Antennas and Wireless Propagation Letters*, vol. 16, pp. 1472-1475, 2017.
- [8] A. Capozzoli, C. Curcio, and A. Liseno, "Optimized nonuniform FFTs and their application to array factor computation," *IEEE Transactions on Antennas and Propagation*, vol. 67, no. 6, pp. 3924-3938, 2019.
- [9] F. Yang, S. W. Yang, W. J. Long, Y. K. Chen, S. W. Qu, and J. Hu, "A novel 3D-NUFFT method for the efficient calculation of the array factor of conformal arrays," *IEEE Transactions on Antennas and Propagation*, vol. 69, no. 10, pp. 7047-7052, 2021.
- [10] Q. H. Liu and N. Nguyen, "An accurate algorithm for nonuniform fast Fourier transforms (NUFFT's)," *IEEE Microwave and Guided Wave Letters*, vol. 8, no. 1, pp. 18-20, 1998.
- [11] J. W. Cooley and J. W. Tukey, "An algorithm for the machine calculation of complex Fourier series," *Mathematics of Computation*, vol. 19, no. 90, pp. 297-301, 1965.
- [12] W. P. M. N. Keizer, "Fast low-sidelobe synthesis for large planar array antennas utilizing successive fast Fourier transforms of the array factor," *IEEE Transactions on Antennas and Propagation*, vol. 55, no. 3, pp. 715-722, 2007.
- [13] W. P. du Plessis, "Efficient computation of array factor and sidelobe level of linear arrays," *IEEE Antennas and Propagation Magazine*, vol. 58, no. 6, pp. 102-114, 2016.
- [14] W. P. M. N. Keizer, "Large planar array thinning using iterative FFT techniques," *IEEE Transactions on Antennas and Propagation*, vol. 57, no. 10, pp. 3359-3362, 2009.
- [15] L. L. Wang, D. G. Fang, and W. X. Sheng, "Combination of genetic algorithm (GA) and fast Fourier transform (FFT) for synthesis of arrays," *Microwave and Optical Technology Letters*, vol. 37, no. 1, pp. 56-59, 2003.

- [16] J. Z. Liu, Z. Q. Zhao, K. Yang, and Q. H. Liu, "A hybrid optimization for pattern synthesis of large antenna arrays," *Progress in Electromagnetics Research-pier*, vol. 145, pp. 81-91, 2014.
- [17] Y. J. Miao, F. F. Liu, J. X. Lu, and K. Li, "Synthesis of unequally spaced arrays with uniform excitation via iterative second-order cone programming," *IEEE Transactions on Antennas and Propagation*, vol. 68, no. 8, pp. 6013-6021, 2020.
- [18] X. M. Xu, C. Liao, L. Zhou, and F. Peng, "Grating lobe suppression of non-uniform arrays based on position gradient and sigmoid function," *IEEE Access*, vol. 7, pp. 106407-106416, 2019.
- [19] D. R. Prado, M. Arrebola, M. R. Pino, and F. Las-Heras, "Application of the NUFFT to the analysis and synthesis of aperiodic arrays," *2017 International Conference on Electromagnetics in Advanced Applications (ICEAA)*, Verona, Italy, pp. 708-711, 2017.
- [20] M. Narasimhan and R. S. Rao, "Synthesis of far-field patterns of circular cylindrical arrays," *Microwave and Optical Technology Letters*, vol. 4, no. 5, pp. 196-199, 1991.
- [21] H. Steyskal and J. S. Herd, "Mutual coupling compensation in small array antennas," *IEEE Transactions on Antennas and Propagation*, vol. 38, no. 12, pp. 1971-1975, 1990.
- [22] J. Rubio, J. F. Izquierdo, and J. Corcoles, "Mutual coupling compensation matrices for transmitting and receiving arrays," *IEEE Transactions on Antennas and Propagation*, vol. 63, no. 2, pp. 839-843, 2014.
- [23] J. Corcoles, M. A. Gonzalez, and J. Rubio, "Mutual coupling compensation in arrays using a spherical wave expansion of the radiated field," *IEEE Antennas and Wireless Propagation Letters*, vol. 8, pp. 108-111, 2009.
- [24] D. Kelley and W. Stutzman, "Array antenna pattern modeling methods that include mutual coupling effects," *IEEE Transactions on Antennas and Propagation*, vol. 41, no. 12, pp. 1625-1632, 1993.
- [25] S. P. Boyd and L. Vandenberghe, *Convex Optimization*, Cambridge, UK, Cambridge University Press, 2004.
- [26] D. W. Boeringer and D. H. Werner, "Particle swarm optimization versus genetic algorithms for phased array synthesis," *IEEE Transactions on Antennas and Propagation*, vol. 52, no. 3, pp. 771-779, 2004.
- [27] N. Jin and Y. Rahmat-Samii, "Advances in particle swarm optimization for antenna designs: Real-number, binary, single-objective and multiobjective

implementations," *IEEE Transactions on Antennas and Propagation*, vol. 55, no. 3, pp. 556-567, 2007.

- [28] W.-C. Liu, "Design of a multiband CPW-fed monopole antenna using a particle swarm optimization approach," *IEEE Transactions on Antennas and Propagation*, vol. 53, no. 10, pp. 3273-3279, 2005.
- [29] Y. H. Liu, Z.-P. Nie, and Q. H. Liu, "A new method for the synthesis of non-uniform linear arrays with shaped power patterns," *Progress in Electromagnetics Research*, vol. 107, pp. 349-363, 2010.



Fan Peng received his Bachelor's degree in applied physics from the Chengdu University of Information and Technology (CUIT), Chengdu, China. In 2016, he entered Southwest Jiaotong University to study for Ph.D. degree in electromagnetic field and electromagnetic waves. His current research includes wide beam antenna, phased array and array synthesis.



Cheng Liao received his Ph.D. degree in electromagnetic fields and microwave technology from the University of Electronic Science and Technology of China, Chengdu, China, in 1995.

From 1997 to 1998, he was a Visiting Scholar with the City University of Hong Kong, Kowloon Tong, Hong Kong. In 1998, he became a Professor with Southwest Jiaotong University, Chengdu. His research interests include computational electromagnetics, electromagnetic compatibility, and antenna theory and technology.



YouFeng Cheng was born in Anqing, Anhui, China, in 1989. He received his Ph.D. degree in radio physics from the University of Electronic Science and Technology of China (UESTC), Chengdu, China, in 2018.

In 2017, he joined the Mechanical Engineering Department, University of Houston, Houston, TX, USA, as a Visiting Scholar. In 2018, he joined Southwest Jiaotong University (SWJTU), Chengdu. His current research interests include phased arrays, reconfigurable antennas, and evolutionary algorithms.



Ju Feng received her Ph.D. degree in electromagnetic field and microwave technology from Southwest Jiaotong University, Chengdu, China, in 2014.

She is currently an Associate Professor at the Institute of Electromagnetic Field and Microwave Technology, Southwest Jiaotong University. Her major research interests include antenna theory and design, computational electromagnetics, and electromagnetic wave propagation.



Sidu Wang received his Bachelor's scholar degree in electronic and information engineering from the Chengdu University of Information and Technology (CUIT), Chengdu, China. In 2015, he worked at the Civil Aviation Flight University of China (CAFUC), Guanghan, China.

His current research includes signal communication, navigation, radar, and aviation safety management.

Planar Antenna Design on the Characteristics of Moore Fractal-based High Impedance Surface

Akash K. Gupta¹, Paladuga S. R. Chowdary², and Mandhapati V. Krishna³

¹Research Scholar, Department of Electronics and Communication Engineering
Centurion University of Technology and Management, Odisha, 761211, India
akgupta452@gmail.com

²Department of Electronics and Communication Engineering
Raghu Engineering College, Visakhapatnam, Andhra Pradesh, 531162, India
satishchowdary@ieeee.org

³Department of Electronics and Communication Engineering
Dhanekula Institute of Engineering and Technology, Vijayawada, Andhra Pradesh, 521139, India
vamshi51@yahoo.co.in

Abstract – This work presents a planar antenna with a rectangular shape designed over a Moore curve fractal-shaped High Impedance Surface (HIS). The Moore fractal geometries are space-filling curves and are useful for multiband applications. The Moore curve-shaped fractal HIS is simulated up to three iterations, and performance is examined. The proposed antenna has multiband operation within the S-band, C-band, and lower X-band frequency of operation. The antenna has a peak gain of 5.08 dB, 4.69 dB, and 5.07 dB with a Moore curve fractal HIS, with iterations 1, 2, and 3 used as the ground plane. The antenna has been analyzed regarding the reflection coefficient, radiation pattern, 3-D polar plots, and surface current distribution. With Moore curve iteration 1, a shaped HIS provides a maximum bandwidth of 740 MHz with the center frequency of 10.95 GHz, 1.24 GHz with the center frequency of 10.57 GHz, and 1.09 GHz with the center frequency of 12.5 GHz with the second and third iterations, respectively.

Index Terms – High Impedance Surface (HIS), Moore curve fractals, rectangular patch antenna.

I. INTRODUCTION

Nowadays, microstrip patch antennas are preferred in many applications in field communications. The patch antennas have a wide range of applications and ease of use due to their low profile, light weight, ease of fabrication, and relatively low cost. The basic microstrip patch comprises a radiating patch followed by a dielectric media and ground plane. The radiation of the microstrip antenna depends on patch geometry as well as

on the ground layer. In most cases, the ground plane consists of the Perfect Electric Conductor (PEC) due to its reflective properties that enhance antenna forward radiation and gain. The PEC ground plane has the limitation in that it causes a 180°-phase shift between the reflected E-field and the incident field. The phase reversal fields result in ripples in an effective radiation pattern. Another disadvantage of this phase reversal reflected wave is that it forms an image current which leads to the formation of surface waves. Thus, normal and surface-wave radiation provides multipath propagation, leading to ripples in the radiation pattern. However, when the ground plane is spaced at 0.25λ below the radiating patch, it will produce an in-phase current and constructive field. In practice, however, such thick substrates are not feasible for antenna applications. To address the problems of surface waves, High Impedance Surfaces are proposed [1]. These types of materials are frequently referred to as Pseudo Artificial Magnetic Conductors (AMCs) with a reflection phase response of $\pm 90^\circ$.

The high-impedance structure (HIS) is a two-dimensional periodic arrangement of metal patches [1]. These patches are spaced with uniform gaps and act as a sheet capacitance (C). Soldered vias are used to link these patches to the ground plane. The ground plane and the via will serve as an inductive sheet (L). Thus, a mushroom-shaped HIS [1] structure can be modeled using a parallel LC lumped circuit, as shown in Fig. 1. The resonance frequency of this equivalent circuit is given in equation (1) and impedance is given in equation (2):

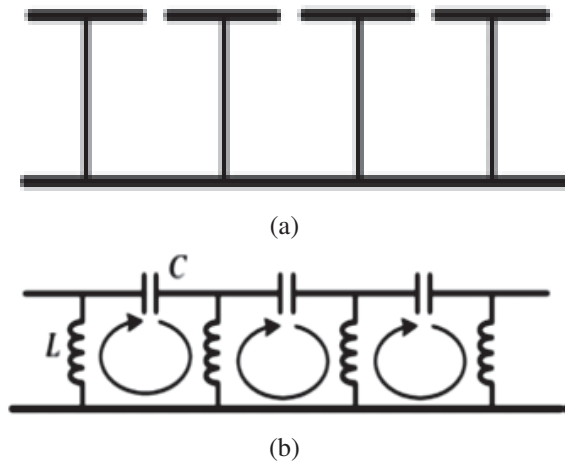


Fig. 1. (a) HIS structure. (b) Equivalent circuit.

$$\omega_0 = \frac{1}{\sqrt{LC}}, \quad (1)$$

$$Z = \frac{j\omega L}{1 - \omega^2 LC}, \quad (2)$$

where z = sheet impedance, C = sheet capacitance L = sheet inductance, and ω_0 is the resonance frequency.

The HIS characteristics are validated using the Finite Difference Time Domain (FDTD) model [2] and the Transmission line model [3]. The reflection phase characteristics of the mushroom shaped HIS are detailed in [4]. The mushroom-shaped HIS ground planes can be used for phased array radars [1]. The hexagonal-shaped HIS cells are used for tunable and steerable antennas [5], while the Generic Algorithm (GA)-optimized square-shaped fractal HIS structures are used for multi-band AMC [6]. The non-uniform HIS structures are designed for bandwidth improvement [7]. The HIS-backed wire antenna [8] is proposed for scanning array applications. A via-less double-layer HIS for polarization-dependent structures, as described in [9], can generate linear and circular polarization. The HIS-based wideband antenna, proposed in [10], is for 14 GHz applications. The dog-bone-shaped HIS structure, proposed in [11], is for RFID and mobile applications, while the HIS-based Luneburg lens, proposed in [12], is for Ku band wave focusing applications. A wearable loop antenna fabricated over a textile surface based on HIS structure is investigated in [13].

This work proposes a Moore curve fractal-shaped HIS structure. The paper is organized as follows: Section I comprises the introduction and literature review, Section II deals with the antenna design methodology, including the design of a Moore curve-shaped HIS cell and rectangular microstrip antenna over the

HIS array, and Section III describes the results and analysis.

II. ANTENNA DESIGN METHODOLOGY

A. Moore curve-shaped HIS unit cell

A Moore fractal curve is a fractal space-filling curve. It is a kind of Hilbert curve proposed by E. H. Moore. Fractal antennas can occupy a small area while covering a larger electrical path length [14]. Due to fractal and self-similar looping structures, they have many resonant frequencies. The Moore fractal curve from the first to the third iteration is illustrated in Fig. 2.

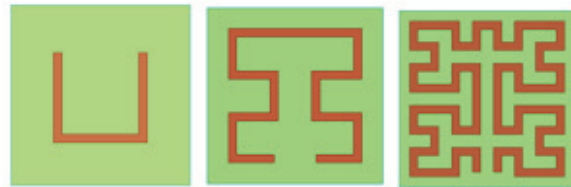


Fig. 2. Moore fractal curve from the first to the third iteration.

A Moore curved HIS unit cell is carved over a square patch of 20×20 mm. The Moore curve patches are designed on a flame retardant 4 substrate with a dielectric constant of 4.4, a loss tangent of 0.02, and a thickness of 1.6 mm.

For the Moore curve HIS cells' phase, reflection characteristics are examined. The effect of vias on reflection characteristics is tabulated in Table 1. For reflection characteristics, the useful bandwidth of a HIS surface has been defined as the range $\pm 90^\circ$, and outside this range of frequencies, the reflected waves are mostly out of phase with the incident waves. As the antenna is intended to function in the X-band, the absence of vias doesn't significantly affect reflection characteristics. Thus, the HIS is designed via-less for ease of fabrication.

B. Moore curve HIS-based rectangular microstrip antenna design

This work presents a rectangular patch antenna designed over a fractal-shaped Moore curve ground plane [14]. The Moore curve HIS rectangular microstrip antenna (MCHRMA) ground plane consists of a 2×2 array of Moore curve-shaped HIS unit cells. The geometry of the antenna is shown in Fig. 3: Fig. 3 (a) illustrates a rectangular radiator over a Moore curve first iteration HIS (MCHRMA-1), Fig. 3 (b) shows a rectangular radiator over a Moore curve in the second iteration HIS (MCHRMA-2), and Fig. 3 (c) shows a rectangular radiator over a Moore curve in the third iteration HIS (MCHRMA-3).

The rectangular patch [15] is designed with dimensions of 28×9 mm² over an FR4 substrate with dimen-

sions of $30 \times 11 \text{ mm}^2$ and thickness of 1.6 mm from the MCH ground plane.

The Moore curve HIS ground plane is used, which is formed by a 2×2 array of Moore-curved HIS cells. The design dimensions of the MCHRMA are tabulated in Table 2.

III. RESULTS AND ANALYSIS

The MCHRMA is designed and simulated using Ansys Electromagnetic Suite 2019 R3. The MCHRMA is examined regarding return loss, radiation pattern, 3-D gain plot, and current density.

A. Reflection coefficient

The reflection coefficient (s_{11}) plot of MCHRMA_1 is shown in Fig. 4. The good impedance matching occurs at 5.87 GHz, 8.38 GHz, 10.31 GHz, and 10.95 GHz, with a return loss of -17.89 dB, -24.72 dB, -19.05 dB, and -13.36 dBi. The MCHRMA_1 has an impedance band-

width of 600 MHz, 360 MHz, 320 MHz, and 740 MHz, respectively. The measured bandwidth is 1790 MHz, 1410 MHz, 1040 MHz, and 1320 MHz, respectively. The measured results have good agreement with the simulated results.

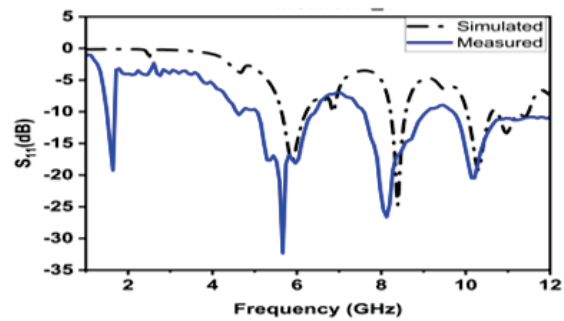
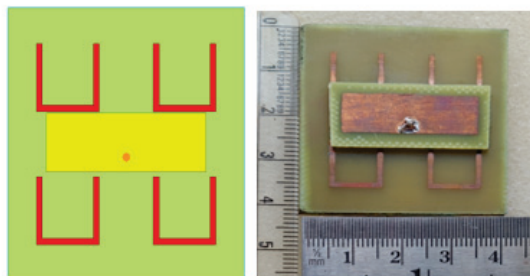
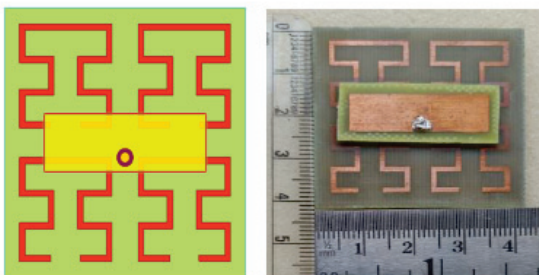


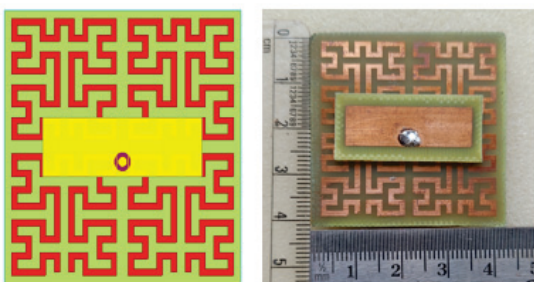
Fig. 4. The reflection coefficient plot for MCHRMA_1.



(a)



(b)



(c)

Fig. 3. (a) Simulated and Fabricated MCHRMA_1. (b) Simulated and Fabricated MCHRMA_2. (c) Simulated and Fabricated MCHRMA_3.

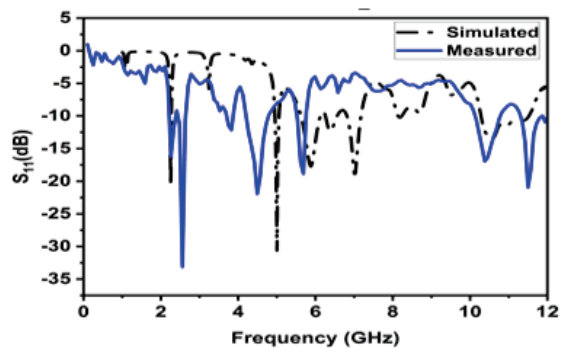


Fig. 5. The reflection coefficient plot for MCHRMA_2.

The reflection coefficient (s_{11}) plot of MCHRMA_2 is shown in Fig. 5. The good impedance matching occurs at 2.25 GHz, 5 GHz, 5.89 GHz, 6.39 GHz, 7.02 GHz, and 10.57 GHz, with a return loss of -20.68 dB, -30.63 dB, -17.65 dB, -12.34 dB, -18.85 dB, and -13.53 dB. The MCHRMA_2 has an impedance bandwidth of 30 MHz, 110 MHz, 510 MHz, 300 MHz, and 370 MHz, respectively. The measured impedance bandwidths are 80 MHz, 440 MHz, 830 MHz, 520 MHz, 600 MHz, and 1210 MHz. The measured results have good agreement with the simulated results.

The reflection coefficient (s_{11}) plot of MCHRMA_3 is shown in Fig. 6. The best impedance matching occurs at 3.79 GHz, 4.85 GHz, 5.39 GHz, 6.09 GHz, 6.98 GHz, 9.32 GHz, 11.03 GHz, and 12.5 GHz, with a return loss of -19.85 dB, -25.16 dB, -11.45 dB, -35.81 dB, -21.91 dB, -10.55 dB, and -34.69 db. The

Table 1: Reflection phase characteristics of Moore curve HIS unit cell

$L_p = W_p = 20$ mm with via ($V_r = 0.5$ mm)				$L_p = W_p = 20$ mm without via			
Design	0°	$+90^\circ$	-90°	Design	0°	$+90^\circ$	-90°
Moore Curve-shaped HIS Iteration 1	–	–	–	Moore Curve-shaped HIS Iteration 1	2.91	2.90	2.92
Moore Curve-shaped HIS Iteration 2	5.85 7.98 9.78	5.80 7.75 9.63	5.86 8.11 9.93	Moore Curve-shaped HIS Iteration 2	5.89 7.92 9.68	5.82 7.7 9.55	5.91 8.08 9.83
Moore Curve-shaped HIS Iteration 3	3.35 4.40 5.87 10.01 11.4	3.34 4.35 5.85 9.98 11.19	3.35 4.45 5.87 10.16 11.59	Moore Curve-shaped HIS Iteration 3	4.41 5.85 9.97	4.35 5.85 9.93	4.45 5.86 9.98

Table 2: MCHRMA design dimensions

S. No.	Antenna Parameter	Dimensions (in mm)
1	Length of HIS patch	20
2	Width of HIS patch	20
3	The gap between HIS unit cells	0.5
4	HIS ground plane array	2×2
5	Substrate 1 thickness	1.6
6	Substrate 2 thickness	1.6
7	Rectangular patch length	9
8	Rectangular patch width	28

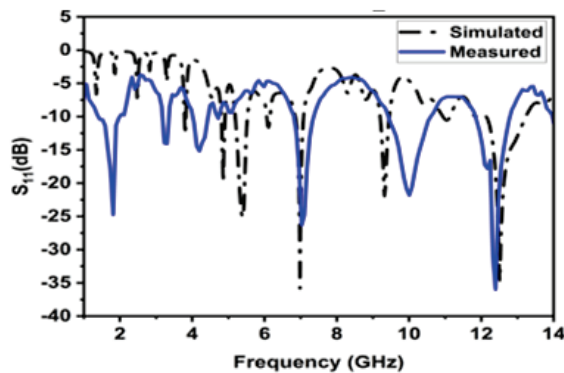


Fig. 6. The reflection coefficient plot for MCHRMA_3.

MCHRMA_3 has an impedance bandwidth of 40 MHz, 110 MHz, 340 MHz, 90 MHz, 230 MHz, 250 MHz, 200 MHz, and 1090 MHz, respectively. The measured bandwidth is 150 MHz, 670 MHz, 450 MHz, 450 MHz, 1080 MHz, and 1160 MHz, respectively. The measured results have good agreement with the simulated results. The simulated results are tabulated in Table 3.

B. Radiation pattern

The radiation pattern of MCHRMA is examined for all its resonance frequencies. The radiation pattern of MCHRMA_1 shown in Fig. 7 has a smooth, stable, and similar response at 5.87, 8.38, and 10.31 GHz. Furthermore, 10.58 GHz patterns have low gain and have ripples in the pattern at the lower hemisphere. The radiation pattern of MCHRMA_2 is shown in Fig. 8. It has a smooth, stable, and similar response at 5, 5.89, 6.39, and 10.97 GHz. Furthermore, 7.02 GHz frequency patterns have low gain and have ripples in the pattern at the lower hemisphere.

The radiation pattern of MCHRMA_3 shown in Fig. 9 has a smooth, stable, and similar response at 5.39, 6.09, 11.03, and 12.5 GHz. Moreover, for 3.79, 4.85, 6.98, 9.32 GHz frequency patterns have low gain and have ripples in the pattern at the lower hemisphere. The radiation pattern has a peak gain of 5.08 dB, 4.69 dB, and 5.07 dB for MCHRMA_1, MCHRMA_2, and MCHRMA_3, respectively.

C. 3D-gain plot

The 3D polar plots for MCHRMA_1, MCHRMA_2, and MCHRMA_3 are shown in Figs. 10, 11, and 12, respectively. The gain plot observed that most radiation is directed over the upper hemisphere, and there is no back radiation. The gain plot has no ripples and side lobes at the resonant frequencies.

D. Surface current density

The surface current distribution at various portions of the patch is represented as the surface current distribution. It displays the current density value at different resonance frequencies. The surface current density of MCHRMA_1, MCHRMA_2, and MCHRMA_3 are shown in Fig. 13. Near the feed position, the surface current is more significant and decreases at the edges. It demonstrates that the feed line has the maximum cou-

Table 3: Simulated results of MCHRMA up to three iterations

Antenna Design	f_c (In GHz)	f_L (In GHz)	f_H (In GHz)	BW (In MHz)	S_{11} (In dB)	Peak Gain (In dB)	Applications
MCHRMA_1	5.87	5.63	6.23	600	-17.89	4.08	C-band/ WLAN (5.4/5.8 GHz) [10]
	8.38	8.22	8.58	360	-24.72	3.41	Lower X-band/ (8.26 GHz) Earth Exploration, satellite services [10]
	10.31	10.3	10.62	320	-19.05	5.08	X-band/ ITU 10 - SHF - Radars, Mobile Phones, and Commercial Wireless LAN
	10.95	10.75	11.49	740	-13.36	4.82	X-band /ITU 10 - SHF - Radars, Mobile Phones, and Commercial Wireless LAN
MCHRMA_2	2.25	2.24	2.27	30	-20.68	-14.65	S-Band /ITU 9- UHF – TV broadcasts, Bluetooth, GPS, and Two-Way Radios
	5	4.95	5.06	110	-30.63	-2.01	C-Band/ ITU 10 - SHF - Radars, Mobile Phones, and Commercial Wireless LAN
	5.89	5.62	6.13	510	-17.65	4.69	C-Band/ ITU 10 - SHF - Radars, Mobile Phones, and Commercial Wireless LAN
	6.39	6.26	6.56	300	-12.34	4.37	C-Band/ ITU 10 - SHF - Radars, Mobile Phones, and Commercial Wireless LAN
	7.02	6.81	7.18	370	-18.85	3.5	C-Band/ ITU 10 - SHF - Radars, Mobile Phones, and Commercial Wireless LAN
	10.57	10.28	11.52	1240	-13.53	3.69	Upper X band(10.48 GHz) Amateur Satellite operating band [10]
MCHRMA_3	3.79	3.78	3.82	40	-12.64	-5.24	S-band WiMAX (3.4-3.69 GHz—IEEE 802.16e) [10]
	4.85	4.8	4.91	110	-19.85	-2.59	C-Band
	5.39	5.19	5.53	340	-25.16	4.73	C-Band Wireless LAN (5.5 GHz) [10]
	6.09	6.06	6.15	90	-11.45	2.88	C-Band
	6.98	6.85	7.08	230	-35.81	0.88	C-Band
	9.32	9.2	9.45	250	-21.91	2.39	X-band (ITU 10 - SHF - Radars, Mobile Phones, and Commercial Wireless LAN
	11.03	10.93	11.13	200	-10.55	4.65	X-band Wireless ISPs (WISP), 4G/5G Operator for LTE Backhaul [10]
	12.5	12.14	13.23	1090	-34.69	5.07	X-band direct broadcast satellite services

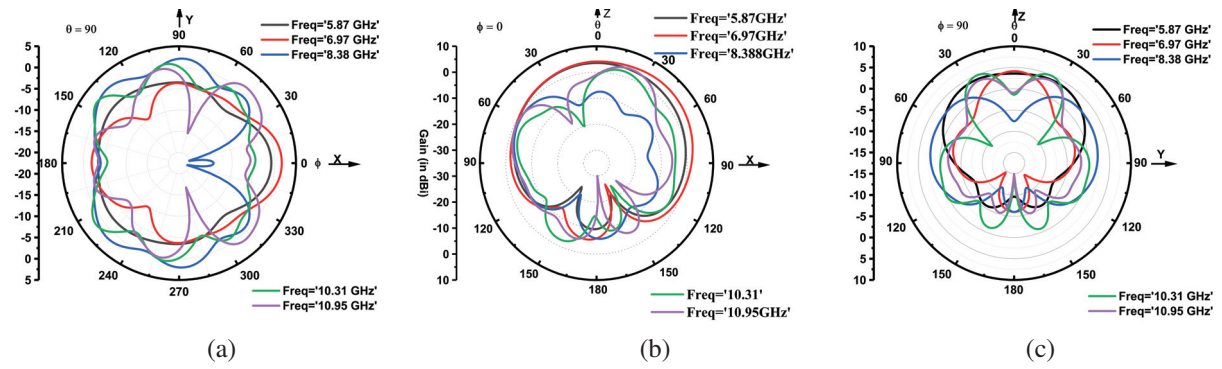


Fig. 7. The E-Plane radiation pattern of MCHRMA_1: (a) XZ Plane, (b) YZ Plane, and (c) XY Plane.

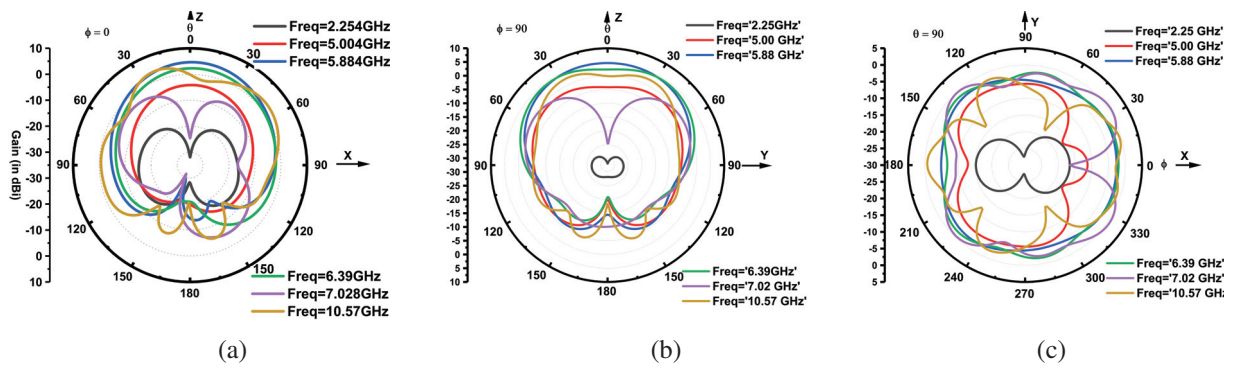


Fig. 8. The E-Plane radiation pattern of MCHRMA_2: (a) XZ Plane, (b) YZ Plane, and (c) XY Plane.

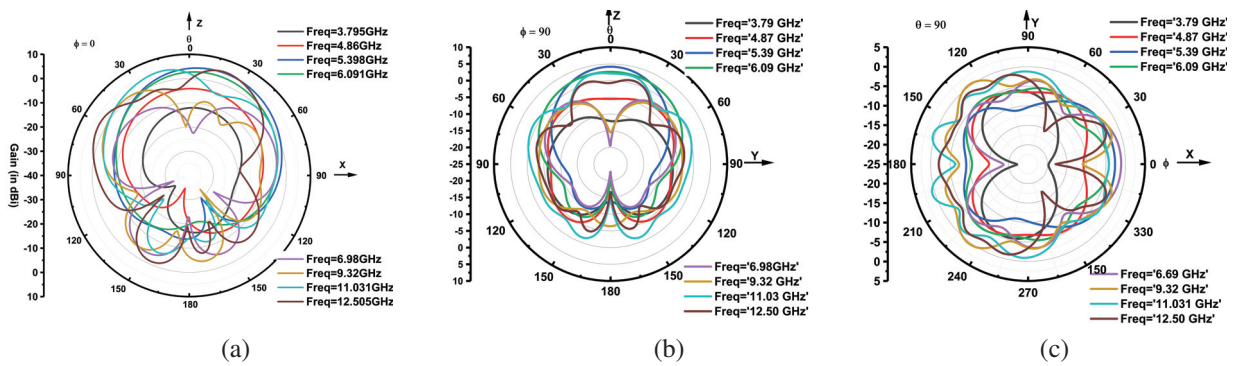


Fig. 9. The E-Plane radiation pattern of MCHRMA_3: (a) XZ Plane, (b) YZ Plane, and (c) XY Plane.

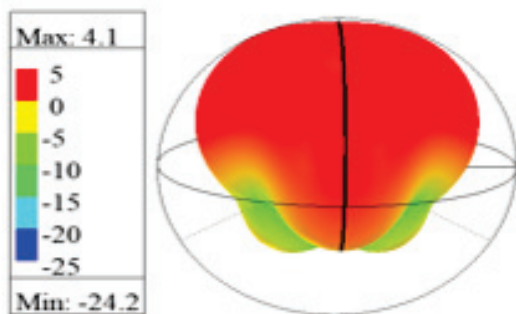


Fig. 10. The gain 3D polar plot of MCHRMA_1.

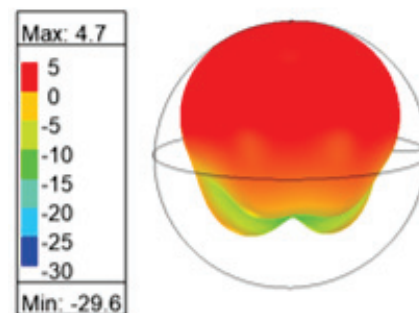


Fig. 11. The gain 3D polar plot of MCHRMA_2.

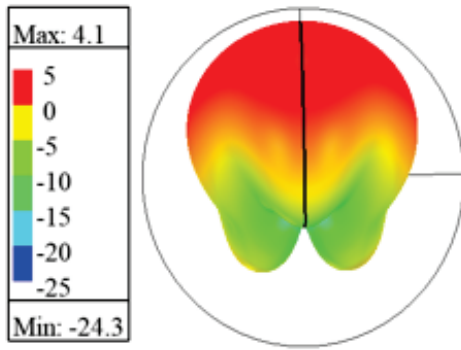


Fig. 12. The gain 3D polar plot of MCHRMA_3.

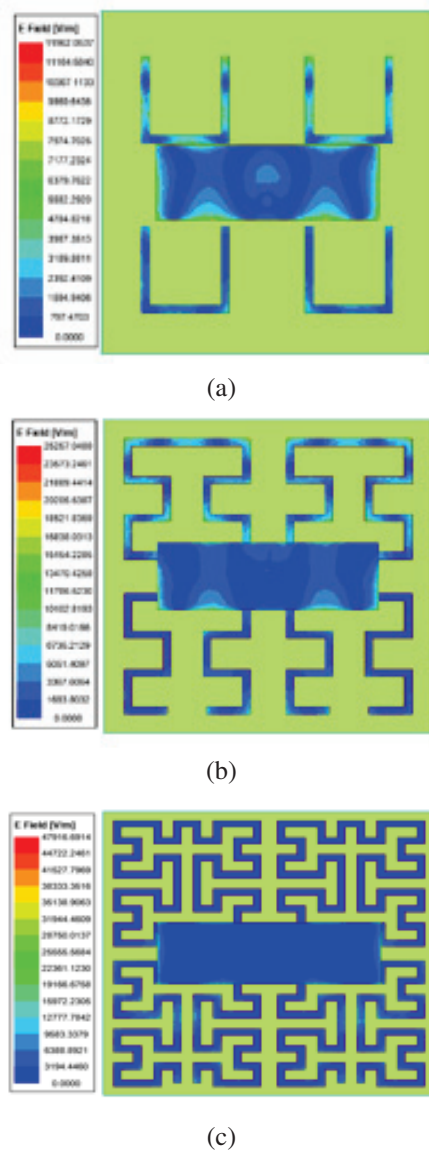


Fig. 13. The surface current density plot: (a) MCHRMA_1, (b) MCHRMA_2, and (c) MCHRMA_3.

pling impact, and HIS suppresses the radiation at the edges and improves the broadside gain.

IV. CONCLUSION

The Moore curve-shaped HIS up to three iterations as the ground plane reflector is investigated. The rectangular patch for the WLAN application is designed over the Moore curve. The Moore curve fractal provides a multiband frequency response. When the Moore curve first iteration is used as HIS plane, it has resonant frequencies of 5.87, 8.38, 10.31, and 10.95 GHz, with a peak gain of 3.41 dB to 5.08 dB. With the Moore curve second iteration, the HIS plane resonated at frequencies of 2.25, 5, 5.89, 6.39, 7.02, and 10.57 GHz, with a max peak gain of 4.69 dB. Similarly, when the Moore curve third iteration is used as HIS ground plane, it has resonant frequencies like 3.79, 4.85, 5.39, 6.09, 6.98, 9.32, 11.03, and 12.5 GHz, and a max peak gain of 5.07 dB is achieved. The surface current distribution shows low radiation at the edges, suppresses surface waves, and smoothens the radiation pattern. The antenna has wide applications in the S-band, C-band, and lower X-band operating frequency regime.

REFERENCES

- [1] D. F. Sievenpiper, "High impedance electromagnetic surfaces," Ph.D. dissertation, Dept. Elect. Eng., UCLA, Los Angeles, CA, USA, 1999.
- [2] F. Yang and Y. Rahmat-Samii, "Reflection phase characterization of an electromagnetic band-gap (EBG) surface," *IEEE Antenna Propag. Soci. Int. Symp. (IEEE Cat. No. 02CH37313)*, San Antonio, TX, USA, pp. 744-747, doi: 10.1109/APS.2002.1018317, 2002.
- [3] S. Clavijo, R. E. Diaz, and W. E. McKinzie, "Design methodology for Sievenpiper high-impedance surfaces: An artificial magnetic conductor for positive gain electrically small antennas," *IEEE Trans. Antennas Propag.*, vol. 51, no. 10, pp. 2678-2690, Oct. 2003.
- [4] F. Yang and Y. Rahmat-Samii, "Reflection phase characterizations of the EBG ground plane for low profile wire antenna applications," *IEEE Trans. Antenna Propag.*, vol. 51, no. 10, pp. 2691-2703, Oct. 2003.
- [5] F. Costa, A. Monorchio, S. Talarico, and F. M. Valeri, "An active high-impedance surface for low-profile tunable and steerable antennas," *IEEE Antennas Wireless Propag. Lett.*, vol. 7, pp. 676-680, Sep. 2008.
- [6] D. J. Kern, D. H. Werner, A. Monorchio, L. Lanuzza, and M. J. Wilhelm, "The design synthesis of multiband artificial magnetic conductors using high impedance frequency selective surfaces,"

- IEEE Trans. Antennas Propag.*, vol. 53, no. 1, pp. 8-17, Jan. 2005.
- [7] M. Hosseini, A. Pirhadi, and M. Hakkak, "Design of a non-uniform high impedance surface for a low profile antenna," *J. Electromagn. Waves Appl.*, vol. 20, no. 11, pp. 1455-1464, Jan. 2006.
- [8] M. Li, S.-Q. Xiao, and B.-Z. Wang, "Investigation of using high impedance surfaces for wide-angle scanning arrays," *IEEE Trans. Antenna Propag.* vol. 63, no. 7, pp. 2895-2901, July 2015.
- [9] G. Gupta and A. R. Harish, "Circularly polarized antenna using a double layered via-less high impedance surface," *Microw. Opt. Technol. Lett.* vol. 58, no. 2, pp. 340-343, Feb. 2016.
- [10] P. K. Panda and D. Ghosh, "Wideband bow-tie antenna with increased gain and directivity by using high impedance surface," *Int. J. RF Microw. Comput. Aided Eng.*, vol. 29, no. 3, pp. e21619, Mar. 2019.
- [11] A. T. Almutawa, H. Kazemi, and F. Capolino, "Analyze and design of thin planar high impedance surface as an antenna," *2018 Int. Conf. Electromag. Adv. Appl. (ICEAA)*, Cartagena, Colombia, pp. 623-624, doi: 10.1109/ICEAA.2018.8520480, 2018.
- [12] G. Cheng, Y.-M. Wu, J.-X. Yin, N. Zhao, T. Qiang, and X. Lv, "Planar Luneburg lens based on the high impedance surface for effective Ku-band wave focusing," *IEEE Access*, vol. 6, pp. 16942-16847, Feb. 2018.
- [13] M. M. Bait-Suwailam, I. I. Labiano, and A. Alomainy, "Impedance enhancement of textile grounded loop antenna using high-impedance surface (HIS) for healthcare applications," *Sensors*, vol. 20, no. 14, p. 3809, July 2020.
- [14] J. K. Ali, "A new microstrip-fed printed slot antenna based on Moore space-filling geometry," *2009 Loughborough Antenna & Propag. Conf.*, Loughborough, UK, pp. 449-452, doi: 10.1109/LAPC.2009.5352551, 2009.
- [15] M. Ali, T. Sittironnarit, V. K. Kunda, H. S. Hwang, R. A. Sadler, and G. J. Hayes, "Wideband patch antenna for 5-6 GHz WLAN applications," *IEEE Antennas and Propag. Society Int. Symp. Digest*, Columbus, OH, USA, pp. 930-933, vol. 2, doi: 10.1109/APS.2003.1219387, 2003.
- [16] J. Anguera, A. Andújar, J. Jayasinghe, V. V. S. S. Chakravarthy, P. S. R. Chowdary, J. L. Pijoan, T. Ali, and C. Cattani, "Fractal antennas: An historical perspective," *Fractal and Fractional*, vol. 4, no. 1, p. 3, Jan. 2020.



Akash K. Gupta received the B.Tech. and M.Tech. degrees from Jawaharlal Nehru Technological University, Kakinada, India, in Electronics and Communication Engineering in 2011 and 2013, respectively. Since 2019 he has been a student researcher in antenna engineering at Centurion University of Technology and Management, Odisha, India. His research interests include microstrip antenna, electromagnetic band-gap structures, high impedance surface antenna designs, and embedded systems.



Paladuga S. R. Chowdary is a Professor and Vice Principal at Raghu Institute of Technology, Visakhapatnam, India. He obtained the M.Tech. and Ph.D. degrees from Andhra University, Visakhapatnam, and Jawaharlal Nehru Technological University, Kakinada, India, respectively. He has been teaching for 20 years and has 5 years of research experience. His research interests are evolutionary computing tools, computational electromagnetics, fractal antennas, and image processing. He is a Senior Member of the IEEE, the Applied Computational Electromagnetics Society, a Life Member of the Instrument Society of India (ISOI), the International Computer Science and Engineering Society (ICSSES), and the Soft Computing Research Society (SCRS).



Mandhapati V. Krishna obtained the Ph.D. degree in Computational Electromagnetics and Antennas from Centurion University, Odisha, India, the M.Tech. degree in Radar and Microwave Engineering from Andhra University, Visakhapatnam, and the B.Tech. degree from Biju Patnaik University of Technology, Odisha. His research interests include soft computing, evolutionary computing tools, antennas, and electromagnetic systems. He is currently a Professor and Head of the Department of Electronics and Communication Engineering, Dhanekula Institute of Engineering and Technology, Vijayawada, Andhra Pradesh, India.

Convolutional Neural Network for Array Size Selection of a Dual-band Reconfigurable Array

Garrett A. Harris, Corey M. Stamper, and Michael A. Saville

Department of Electrical Engineering
Wright State University, Dayton, Ohio, 45435, USA
michael.saville@wright.edu

Abstract – A convolutional neural network (CNN) is designed and trained to partially control a dual-band, large uniform rectangular array of reconfigurable radiating elements. The CNN selects the number of active elements and switch states needed to achieve a desired beam shape. Both pattern multiplication and finite element method (FEM) are used to simulate the radiation patterns of a PIN-diode square-spiral antenna array. After training on radiation pattern images of arrays calibrated for both phase and gain imbalance and mutual coupling, the CNN achieves 97 percent validation accuracy. Then, using the resulting size and switch states, the patterns are simulated with and without mutual coupling using the pattern multiplication model and FEM, respectively. The mean beam steering and 3-dB beamwidth errors without mutual coupling are less than 5.5 degrees and up to 12.3 degrees with mutual coupling.

Index Terms – convolutional neural network, machine learning, pattern multiplication, reconfigurable array.

I. INTRODUCTION

Multichannel arrays are commonly used as multiple-input multiple-output (MIMO) antennas in communications [1–3]. These antennas are essential for multi-beam forming [4], fast angle-of-arrival estimation [5], interference suppression [3], and array calibration [6–7]. The reconfigurable antenna has gained much attention for MIMO arrays because it can facilitate smart antenna technology in which the system senses the environmental conditions and automatically changes the antenna elements and circuitry to operate at different frequencies [2], with different polarization states [8], and with different radiation patterns [1, 9], or a combination thereof [10].

Typical switch methods [3] for the reconfigurable antenna include radio-frequency (RF) micro-electromechanical machines (MEMS), PIN diodes, and varactors, but emerging methods include liquid metals [12], plasma tubes [13], and laser-controlled optical win-

dows [14]. Regardless of the type of switch, the reconfigurable array also requires careful treatment to minimize switch redundancy and to meet beam shape objectives [3]. The machine learning methods such as deep and convolutional neural networks [15–20] have gained much attention for such solutions.

For example, in [17], a 2D PIN-diode reconfigurable intelligent surface (RIS) is used to maximize bit rate in a MIMO system where a CNN is trained to learn the beamforming phases of the RIS for an arbitrary receiver direction. In [18], sidelobe level is controlled by particle swarm and bacteria foraging optimization and is shown to be effective even when individual elements fail. In [19], a CNN is used to design the required complex weights for an 8×8 planar array so that it can be steered in a desired direction. In a similar example, a multi-layer perceptron network is trained in [20] to produce the complex beam steering weights for a uniform linear array of square patches. The recent work of [21] introduced a dual-CNN concept where the CNN estimates the required active elements and steering weights when given an arbitrary radiation pattern.

Prior to the recent popularity of CNNs, a great deal of research was done on using genetic algorithms to design array layouts. In [22], several genetics-inspired algorithms are presented to optimize widely-spaced, wideband arrays with a focus on minimizing sidelobe levels. Another article [23] explores the use of genetic algorithms to design highly directional and rotationally symmetric arrays. However, genetic algorithms require a large time commitment. In one example presented in [23], a single array design took over 270 hours to complete. This makes CNNs particularly attractive due to their ability to solve complex optimization problems in a matter of minutes rather than hours. However, array size selection for reconfigurable arrays have yet to be reported in the literature.

Most CNNs for arrays consider simple radiating elements such as patches, or are limited to a fixed and small array size. Here, we present a novel CNN that predicts the required number of active elements as well as

antenna state of a large uniform reconfigurable rectangular array when given an arbitrary desired specification of beam direction and shape. The array element in this work consists of frequency and pattern reconfigurable spirals designed with the PIN diode single-turn square spiral antenna (PSSA) [24–25].

As it is well known how the CNN training relies on thousands of observations, the pattern multiplication model is used to generate radiation pattern images. The CNN is designed to select the array size and PIN diode ON/OFF states. Training with the images allows the CNN to learn the control parameters that meet a fully specified beam shape, i.e. main beam shape, sidelobe level, and null placement.

The paper is organized as follows: Section II describes the unit cell and array design of [24]. Section III presents the pattern multiplication model and the method to create training images. Section IV describes the CNN and its training. Results and conclusions are presented in Sections V and VI, respectively.

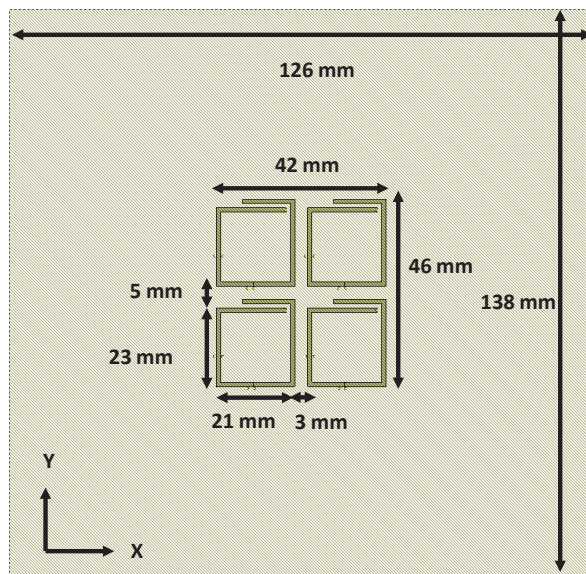


Fig. 1. Layout of the unit cell of [24] but with a larger finite ground plane.

II. ANTENNA ARRAY

A. Reconfigurable element

For the communications array, we considered different reconfigurable antennas that operate at discrete frequencies, could be easily scaled and easily implemented. Hence, the printed square spiral, being in the class of frequency independent antennas, offers both wideband tuning and would easily scale during fabrication. The work of [25] presented a PSSA that used two PIN diodes: one series diode to change the frequency of operation from

3.75 GHz to above 6.0 GHz, and one shunt diode to change the radiation pattern from a boresight pattern to a squinted beam. Thus, the array could operate in two discrete bands (S and C). Also, the radiation pattern was considered for its potential to add an additional degree of freedom in digital beam shaping of the array, but was ultimately left unused. Lastly, the planar form of the PSSA could be arranged in a multichannel planar array where each unit cell has a dedicated transceiver for digital beamforming.

B. Unit cell and array

The planar array design of [24] defines the unit cell as a 2×2 rectangular arrangement of identical PSSA elements with elemental spacings $d_x = 42.0$ mm, and $d_y = 46.0$ mm as shown in Fig. 1. Using a five-layer layout for the model, based on two sheets of Roger's Duroid 5880, the unit cells and feed network are on the top and bottom copper layers, respectively. Conductive vias connect the bias lines to the PIN diodes through the middle copper shielding layer.

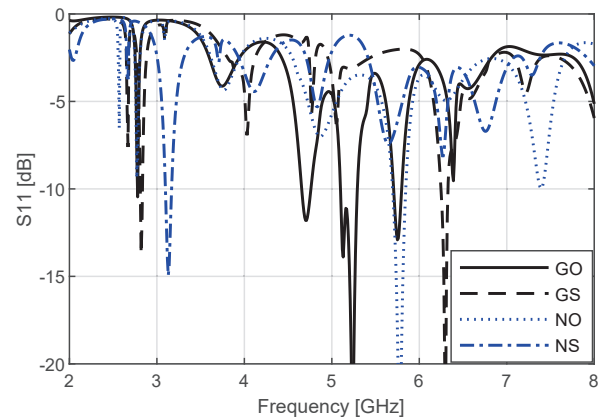


Fig. 2. S11 of the unit cell for each switch state.

The design was modeled with Cadence AWR [24] software using a five-layer stack representing the dielectric laminates. The diode model uses ideal ON and OFF states as in [25] where the microstrip trace is continuous for the ON state and a gap is placed at the location of the diode for the OFF state. The gap length is equal to the physical size of the diode. As an alternative model, the diodes could have been replaced with microstrip transmission lines of equivalent S-parameters [2], or with a series resistor and capacitor [8]. We also note how the model lacks a DC blocking capacitor and RF choke which would affect the final antenna pattern. Differences with the simulated unit cell's radiation pattern with and without the added components and lines are independent of the neural network training methodology and would only require an updated set of simulated radiation pattern images during training.

Table 1: Frequency, 10-dB bandwidth, and half-power beam width of the unit cell for each switch state

	NS	NO	GS	GO
Frequency (GHz)	3.10	5.80	6.30	5.23
10-dB bandwidth (MHz)	60.0	150.0	80.0	190.0
Az-HPBW (deg)	180.0	180.0	76.0	64.0
EI-HPBW (deg)	76.0	56.0	56.0	56.0

In the following, the switch state descriptions follow [25] as GO, GS, NO, and NS where O and S denote open (OFF) and short (ON) for the series diode, and G and N denote grounded (ON) and not grounded (OFF) for the shunt diode. The design in [24] also considered various rotations and reflections of the individual PSSA elements but found that the 2×2 uniform placement provided the best uniformity of the radiation patterns of the different states and was deemed most appropriate for a large array. The arrangement also made the layout simpler for the control lines and corporate feed line. Each PSSA element of the unit cell has one series and one shunt diode, both of which are enabled/disabled at the same time during operation. However, unlike [21], the ground plane for the unit cell used here is sized for a 3×3 array to provide better backlobe characterization.

The unit cell has subtle differences in frequency of operation and radiation pattern when compared to those of the single PSSA element with the same switch state. Figure 2 shows the S11 responses from 2.0 to 8.0 GHz. Table 1 lists the resonant frequencies used in this work along with the 10-dB bandwidths, and half-power beam widths for the radiation patterns shown in Fig. 3.

III. PATTERN MULTIPLICATION MODEL

A. Array pattern model

The pattern multiplication model is a well-known approximation of the array pattern and assumes the antenna elements have the same current distribution. The factored array pattern is

$$F(\theta, \phi) = f_c(\theta, \phi)AF(\theta, \phi), \quad (1)$$

where f_c is the unit cell's radiation pattern and AF is the array factor. The model ignores mutual coupling and effects of a finitely sized array. However, it allows efficient calculation of the array pattern and study of the antenna performance in digital beamforming applications.

The unit cell of each reconfiguration state is first modeled with Cadence AWR software in the x - y plane, and the radiation pattern is simulated over the set of discrete spherical angles $\phi \in [-180, 180]$, $\theta \in [0, 180]$ in degrees. However, the digital beamforming model is defined in the y - z plane with the azimuth and elevation angular coordinates shown in Fig. 4. Hence, the unit cell

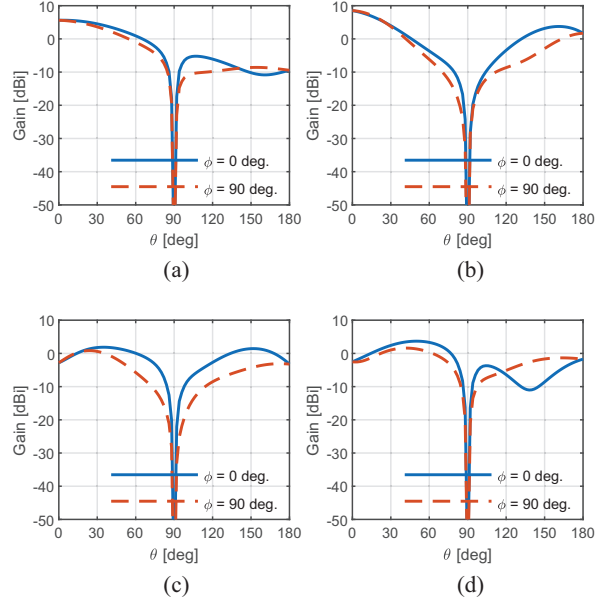


Fig. 3. Gain pattern cuts in dBi of the unit cell for each switch state. Cuts along θ at $\phi = 0$ deg. (solid line) and $\phi = 90$ deg. (dashed line). (a) NS at 3.13 GHz. (b) NO at 5.78 GHz. (c) GS at 6.30 GHz. (d) GO at 5.24 GHz.

pattern is resampled using spline interpolation from the AWR reference frame to the array's reference frame at aspects $\phi \in [-90, 90]$, $\theta \in [-90, 90]$ in degrees. This approach avoids beam wrapping in the radiation pattern image and the need to cast images in sine space coordinates [19].

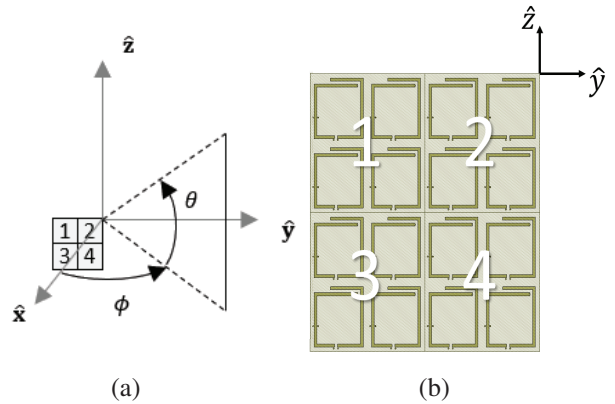


Fig. 4. (a) Array reference frame. (b) Four unit cells showing the reference element.

Each unit cell has position $d_{np} = -\hat{y} n d_y - \hat{z} p d_z$ where $n = 0, \dots, N_y - 1$, $p = 0, \dots, N_z - 1$ and d_y and d_z are the elemental spacing. For the signal direction

$$\hat{\mathbf{u}}(\theta, \phi) = \hat{\mathbf{x}} \cos \phi \cos \theta + \hat{\mathbf{y}} \sin \phi \cos \theta + \hat{\mathbf{z}} \sin \theta, \quad (2)$$

the np -th cell has phase:

$$\Psi_{np}(\hat{\mathbf{u}}) = k\hat{\mathbf{u}}^T \hat{\mathbf{d}}_{np}, \quad (3)$$

which is relative to the reference element. In equation (3), $k = 2\pi/\lambda$ is the wave number and the superscript T denotes vector transpose.

For efficient calculation, the weighted array factor

$$AF(\hat{\mathbf{u}}) = \sum_n \sum_p s_{np} \exp(j\Psi_{np}(\hat{\mathbf{u}})), \quad (4)$$

is recast from the matrix-vector product in (4) to the steering vector product $AF(\hat{\mathbf{u}}) = \mathbf{v}^H(\hat{\mathbf{u}})\mathbf{s}$ using:

$$\mathbf{v}(\hat{\mathbf{u}}) = \mathbf{e}(\hat{\mathbf{u}}) \otimes \mathbf{a}(\hat{\mathbf{u}}), \quad (5)$$

where \otimes denotes the Kronecker vector product and:

$$\mathbf{a}(\hat{\mathbf{u}}) = \left[1, e^{jkd_y \hat{\mathbf{u}}^T \hat{\mathbf{y}}}, \dots, e^{jkd_y (N_y - 1) \hat{\mathbf{u}}^T \hat{\mathbf{y}}} \right]^T, \quad (6a)$$

$$\mathbf{e}(\hat{\mathbf{u}}) = \left[1, e^{jkd_z \hat{\mathbf{u}}^T \hat{\mathbf{z}}}, \dots, e^{jkd_z (N_z - 1) \hat{\mathbf{u}}^T \hat{\mathbf{z}}} \right]^T. \quad (6b)$$

In equation (5), the azimuth (\mathbf{a}) and elevation (\mathbf{e}) steering vectors represent the incremental phase progression across each dimension of the array. In equation (4), s_{np} is the complex weight used to electronically control the beam direction and shape upon transmission. In a receive mode, it represents the signal from an arbitrary direction $\hat{\mathbf{u}}_0$.

The weighted steering vector for beam steering in the direction $\hat{\mathbf{u}}_0 = \hat{\mathbf{u}}(\theta_0, \phi_0)$ with controlled sidelobes is:

$$\mathbf{s}(\hat{\mathbf{u}}_0) = [\mathbf{w}_e \odot \mathbf{e}(\hat{\mathbf{u}}_0)] \otimes [\mathbf{w}_a \odot \mathbf{a}(\hat{\mathbf{u}}_0)], \quad (7)$$

where \odot denotes the Hadamard vector product. The azimuth (\mathbf{w}_a) and elevation (\mathbf{w}_e) weight vectors control sidelobe levels with windowing functions such as Taylor and Hanning, etc. Therefore, the array's radiation pattern in the direction $\hat{\mathbf{u}}$ is:

$$F_a(\hat{\mathbf{u}}) = f_c(\hat{\mathbf{u}}) [\mathbf{v}(\hat{\mathbf{u}})]^H \mathbf{s}, \quad (8)$$

where the superscript H denotes the Hermitian transpose.

B. Training data generation

Figure 5 shows the normalized intensity patterns for the different states of the unit cell for an 8×8 array. Each pixel in the image corresponds to a direction $\hat{\mathbf{u}}(\theta, \phi)$ and the pixel value is calculated with equation (8). The weights of equation (7) are selected as -35 -dB Taylor weights, and the beam is steered to boresight ($\theta_0 = 0$ deg., $\phi_0 = 0$ deg.). Figure 6 shows the pattern when the beam is steered to elevation $\theta_0 = 30$ deg. and azimuth $\phi_0 = 30$ deg.

The images of Figs. 5 and 6 are normalized intensity with units of decibels. In Section IV, equation (8) is used to create a single channel image representing linear gain scaled to $[-1, 1]$. It is noted how an alternative approach and possibly a better approach is to use three-channel images where channel 1 is the normalized intensity image on a decibel scale with 60-dB dynamic range, channel 2 is a linear-scale image, and channel 3 is a quarter-power linear-scale image. Finally, each image channel would also be scaled to the interval $[-1, 1]$.

C. Consideration of mutual coupling

The analysis of [24] considered effects of mutual coupling and concluded that the effect on the pattern multiplication model was negligible for arrays larger than 3×3 . However, the GO and GS patterns showed a greater impact of mutual coupling than the NS and NO patterns. When the shunt diode is off, the current flow remains in the spiral winding and exhibits an overall symmetry about the unit cell. However, when the shunt diodes are on (GO, GS), a portion of the current flows to the ground plane and disturbs the symmetry. As reported in [25], the lack of symmetry changes the radiation pattern but also causes an increased contribution to mutual coupling.

Hence, the unit-cell pattern of equation (8) was simulated as an isolated 2×2 array of PSSA elements and designated as f_c^{iso} to distinguish it from the embedded unit cell pattern f_c^{emb} . The embedded pattern was simulated in AWR as a 3×3 array of unit cells with the center cell active and all others inactive. Both array patterns F^{iso} and F^{emb} are considered during the CNN training.

IV. ARRAY CONFIGURATION WITH CNN

A. Machine learning approach

The general theories of CNN and machine learning are beyond the scope of this paper, but [26], [27] give the theory of the CNN, and for antenna array applications. The objective of the machine learning controller is to predict the length of each dimension of the array ($d_y N_y, d_z N_z$) and to predict the PIN diode switch states (NS, NO, GS, GO) that meet a desired array pat-

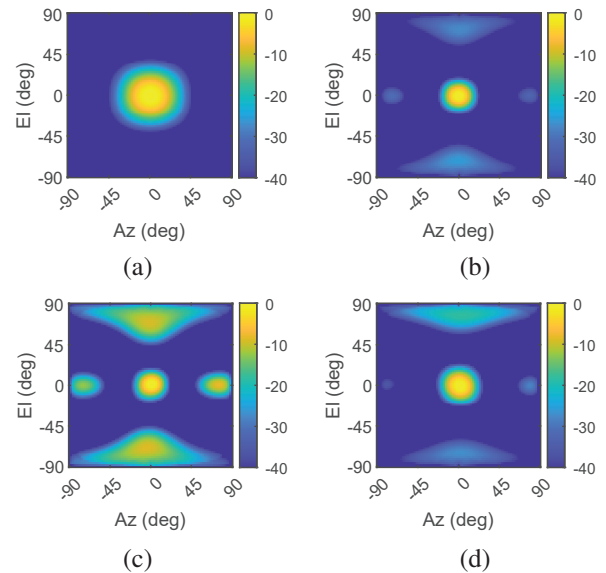


Fig. 5. Normalized 3D gain patterns in dB for the 8×8 array. The signal arrives from aspect ($\theta_0 = 0$ deg., $\phi_0 = 0$ deg.). (a) NS. (b) NO. (c) GS. (d) GO.

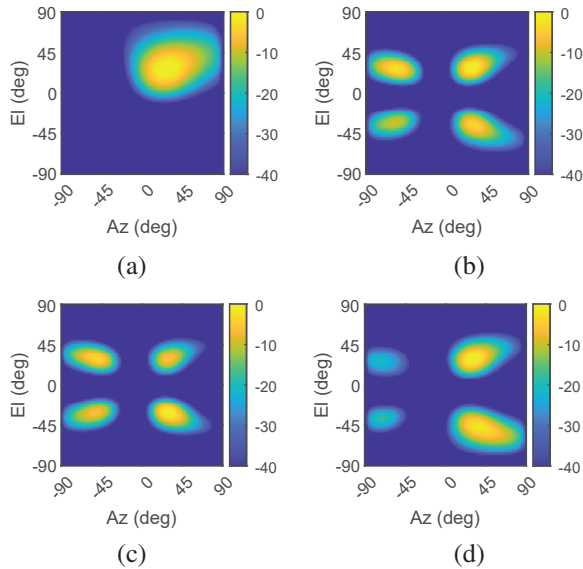


Fig. 6. Normalized 3D gain patterns in dB for the 8×8 array. The signal arrives from aspect ($\theta_0 = 30$ deg., $\phi_0 = 30$ deg.). (a) NS. (b) NO. (c) GS. (d) GO.

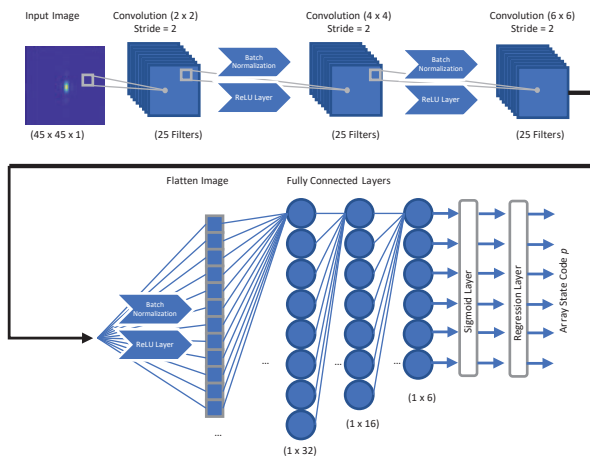


Fig. 7. CNN architecture: the first stage comprises three convolution layers and the second stage consists of three fully connected input, hidden, and output layers.

tern. We assume that the unit cells are adjacent and have fixed spacing (d_y, d_z). Then, we define the predicted array state vector as $\mathbf{p} = [S, N_y, N_z]$, which is cast as the binary number p for convenience during CNN training.

Unlike [15] that uses a self-organizing map neural network to learn the PIN diode switch states from 1D S11 data, we use a CNN to learn the relationship between the array pattern and p . Our approach is similar to [19] where a CNN is trained to learn the phase control of an 8×8 planar array from 2D images of radiation patterns.

Using equation (8), we generate a large sample of images for different array sizes and switch states and train a CNN to learn the relationship between the array pattern and the switch state when the beam is steered in an arbitrary direction. When simulating patterns with equation (8), the array is assumed to have ideal phase and gain calibration and ideal compensation for mutual coupling. Then, we use the trained CNN to predict the array state vector from an intensity image of the desired array pattern; that is, a mask of the pattern we want to radiate with the array.

There are two main challenges for using a CNN. First, training the CNN requires a large amount of data. Full-wave simulations would take an untenable amount of time so we use the pattern multiplication technique. Second, the neural network architecture is an art and requires substantial trial and error. Neural networks can have many different layers which all perform different tasks. Some layers work well together, and some do not. Next, we describe the training and testing data and the CNN architecture. We present results in Section V.

B. Training data

The input data consists of 46×46 -pixel grayscale images that represent the magnitude of the radiation patterns in the forward hemisphere of the array. The set of images are generated with equations (6) and (8) using a variable array shape, reconfigurable switch state, and steering direction, which are represented in the label p . We also scaled the pixel values to the interval $[-1, 1]$. The length of the array in each dimension is allowed to be within $[2, 4, 6, 8]$, and the steering direction $\hat{\mathbf{u}}_0$ is constrained to a 45-degree cone relative to boresight. Also, a -35 -dB Taylor window is used to reduce sidelobes. Each image has dimensions corresponding to the azimuth and elevation angles of the forward hemisphere of the array.

For each combination of array size and switch state the array is steered to 1,000 uniformly sampled directions, and the total data set comprises 64,000 unique images. Lastly, 10 percent of the training data is randomly selected for use during CNN validation. This validation set comprises 6,400 images randomly selected before training. These images are not included in the training set but are used to estimate CNN accuracy after training. Validation accuracy during training is calculated as root mean square error (RMSE) from the known and predicted values of p during training. In addition, the validation set was tested by calculating the percentage of correctly predicted state vectors.

C. CNN architecture

Figure 7 shows the CNN design that consists of a three-layer convolution stage followed by a three-layer

neural network. In the first stage, each image is down-sampled and then processed with eight 3×3 convolution kernels. The subsequent convolution layers use 5×5 and 7×7 kernels. Then, the images are flattened (vectorized) as input to the neural network. Three hidden layers are used. The output of the CNN is quantized as 0 or 1 in order to create a binary number that represents the array state. Table 2 lists the specific layers, convolution window sizes, and number of nodes. Table 3 lists the final set of hyperparameters that control batching, dropout, learning rate and loss metric. The output layer represents regression-based prediction of the array state but in a binary form. The specific CNN architecture was learned by trial and error [21]. Training the CNN on a Windows 10 machine with MATLAB 2021b took approximately 25 minutes on a single CPU (Intel i5 with 16 GB RAM), and 3 minutes on an Intel i7 with 32 GB with a single GPU (Nvidia RTX A3000 with 6GB).

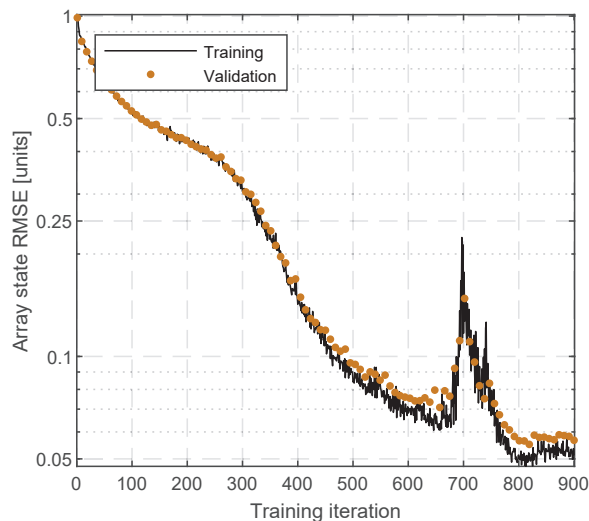


Fig. 8. Root mean square error (RMSE) calculated with the known and predicted values of p during CNN training.

V. RESULTS

After experimenting with several architectures and training schemes, the network achieved an accuracy of 97% on the validation data. This high level of accuracy indicates that the network learned the general relationship between the radiation patterns and the array configurations. However, we set up testing data to observe how well the network performs when given a radiation mask that was produced by a different method.

Hence, test data consists of arbitrary and novel radiation patterns (masks) that were unobserved by the CNN during training. We first generated masks with a 2D Gaussian pulse to approximate the main beam of the array for a desired beam direction and beamwidth.

Table 2: CNN layers characterized according to their function; e.g. convolution, batching, normalization, activation function, and connectedness

Layer	Type	Options
Layer 1	2D Convolution	25 2×2 Filters, Stride = 2
Layer 2	Batch normalization	n/a
Layer 3	ReLU	n/a
Layer 4	2D Convolution	25 4×4 Filters, Stride = 2
Layer 5	Batch normalization	n/a
Layer 6	ReLU	n/a
Layer 7	2D Convolution	25 6×6 Filters, Stride = 2
Layer 8	Batch normalization	n/a
Layer 9	ReLU	n/a
Layer 10	Fully connected	32 Nodes
Layer 11	Fully connected	16 Nodes
Layer 12	Fully connected	6 Nodes
Layer 13	Sigmoid	n/a
Layer 14	Regression	n/a

Table 3: CNN training options and hyperparameters that control the learning accuracy

Hyperparameter	Setting
Optimization method	adam
Epochs	100
Mini batch size	160
Learning rate	0.001
L2 regularization	0.001
Gradient threshold	Inf

The network struggled to predict the correct array state for this mask type. Instead, we used Taylor-windowed isotropic array patterns using equations (5) and (6) and saw a noticeable improvement in validation accuracy. We considered how the sidelobe structure contributes to the CNN learning, and we confirmed it by observing how the respective neurons became active when null features were detected in the convolution layers.

In order to test the effectiveness of the CNN, 1,000 arbitrary radiation pattern masks were simulated for array sizes N_y, N_z in $[2, 4, 6, 8]$ and main beam directions $[-45 \leq \theta, \phi \leq 45]$ deg. The operating frequency was randomly assigned to one of the four unit cell frequencies listed in Table 1.

As the CNN returns a discrete array state p (size and switch configuration), we tested the effectiveness of the network's prediction by comparing the pattern

$G(p)$ calculated with equation (8) to the input mask. For each test and mask pair we compared the mainlobe's steering angles (θ_0, ϕ_0) and half-power beamwidths (θ_{3dB}, ϕ_{3dB}) and calculated the mean differences ($\Delta\theta_0, \Delta\phi_0, \Delta\theta_{3dB}, \Delta\phi_{3dB}$) listed in Table 4. Except for the elevation steering angle which has a mean error of 5.5 deg., the mean error is less than 4 deg. and suggests the CNN has successfully learned the relationship between the pattern features and the array configuration. The increased error in the elevation steering angle is likely a result of the specific pattern of the unit cell. We also noticed how the beamwidth and steering angles were less than 2 degrees when the size of the array exceeded 3×3 and the steering angle was within a 30-deg. cone.

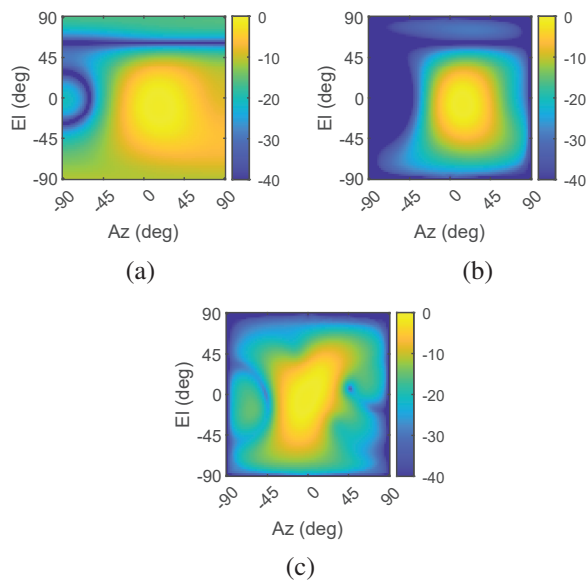


Fig. 9. Desired and predicted patterns for beam steered to $\phi = 17$ deg. and $\theta = 11$ deg. Azimuth and elevation, respectively. (a) Desired pattern and CNN predictions using (b) $G(p)$ and (c) $H(p)$.

The pattern when calculated with G assumes ideal phase and gain calibration for the individual transmit and receive channels and ideal compensation for mutual coupling. To check the effects of mutual coupling, we selected several predicted array states where $G(p)$ had errors less than 5 deg. and simulated the array pattern with AWR as $H(p)$. Thus, H assumes ideal phase and gain calibration of the individual channels but no compensation for mutual coupling (MC). For computing time and memory limitations, only six array configurations were selected and the number of unit cells was limited to nine or less. Figures 9 shows an example with $p = [NS, 4, 2]$ and steering angles of 17 deg. in elevation and 11 deg. in azimuth. Figures 9 (a) shows the test mask (windowed, isotropic array factor),

Table 4: Mean steering angle and half-power beamwidth errors in degrees for pattern multiplication (G) and FEM (H) test images

Test Method	$\Delta\theta_0$	$\Delta\phi_0$	$\Delta\theta_{3dB}$	$\Delta\phi_{3dB}$
$G(p)$	-5.5	3.7	-2.9	-2.7
$H(p)$	-9.3	12.3	12.3	2.3

Figs. 9 (b) shows $G(p)$ (windowed, pattern multiplication model with ideal phase/gain calibration and MC-compensation), and Figs. 9 (c) shows $H(p)$ (windowed, calibrated phase/gain, MC-uncompensated). The mean errors for $H(p)$ are listed in Table 4, and are larger than the errors of $G(p)$.

We effectively trained the CNN with patterns of a calibrated and MC-compensated array, but we tested with MC-uncompensated array patterns. The increase in error is reasonable given the well-known degrading effects of mutual coupling on the array pattern.

VI. CONCLUSION

A convolutional neural network has been presented for predicting the array state from an arbitrary beam shape. The network was trained with images of different radiation patterns and learned the number of elements needed to achieve the mask. Using a recently studied uniform rectangular array of reconfigurable planar square spiral antennas, the network achieved a 97% training accuracy. When tested with masks of different distributions than those used during training, the desired mask and the pattern multiplication model had good agreement between the beamwidths (less than 3 deg.) and steering direction (less than 6 deg.). However, when the mask was compared to the array pattern when mutual coupling was present, the errors increased by up to 12.3 degrees.

The CNN was trained using patterns representing the ideal case where there is no mutual coupling, and with balanced gain and phase. Future work will train CNNs with gain and phase imbalances as well as pattern distortions from mutual coupling in order to compensate for these limitations in real arrays.

ACKNOWLEDGMENT

The authors thank the DAGSI Fellowship program for supporting the foundational work presented in [24], and the DoD SMART Scholarship program for support during the current work.

REFERENCES

- [1] Y. Zhou, R. S. Adve, and S. V. Hum, "Design and evaluation of pattern reconfigurable antennas for MIMO applications," *IEEE Trans. Antennas Propag.*, vol. 62, no. 3, pp. 1084-1092, doi: 10.1109/TAP.2013.2284874, Mar. 2014.

- [2] D. Piazza, N. J. Kirsch, A. Forenza, R. W. Heath, and K. R. Dandekar, "Design and evaluation of a reconfigurable antenna array for MIMO systems," *IEEE Trans. Antennas Propag.*, vol. 56, no. 3, pp. 869-881, doi: 10.1109/TAP.2008.916908, Mar. 2008.
- [3] Y. Tawk, J. Constantine, and C. G. Christodoulou, *Antenna Design for Cognitive Radio*, Artech House, Norwood, MA, 2016.
- [4] L. Di Palma, A. Clemente, L. Dussopt, R. Sauleau, P. Potier, and P. Pouliguen, "Radiation pattern synthesis for monopulse radar applications with a reconfigurable transmitarray antenna," *IEEE Trans. Antennas Propag.*, vol. 64, no. 9, pp. 4148-4154, doi: 10.1109/TAP.2016.2586491, Sep. 2016.
- [5] X. Wang, E. Aboutanios, M. Trinkle, and M. G. Amin, "Reconfigurable adaptive array beamforming by antenna selection," *IEEE Trans. Signal Process.*, vol. 62, no. 9, pp. 2385-2396, doi: 10.1109/TSP.2014.2312332, May 2014.
- [6] Y. Ji, J. Ø. Nielsen, and W. Fan, "A simultaneous wideband calibration for digital beamforming arrays at short distances [Measurements Corner]," *IEEE Antennas Propag. Mag.*, vol. 63, no. 3, pp. 102-111, June 2021.
- [7] T. W. Nuteson, J. E. Stocker, J. S. Clark, D. S. Haque, and G. S. Mitchell, "Performance characterization of FPGA techniques for calibration and beamforming in smart antenna applications," *IEEE Trans. Microw. Theory Tech.*, vol. 50, no. 12, pp. 3043-3051, doi: 10.1109/TMTT.2002.805151, Dec. 2002.
- [8] V. Zarei, H. Boudaghi, M. Nouri, and S. A. Aghdam, "Reconfigurable circular polarization antenna with utilizing active devices for communication systems," *Applied Computational Electromagnetics Society (ACES) Journal*, vol. 30, no. 9, pp. 990-995, <https://journals.riverpublishers.com/index.php/ACES/article/view/10395>, Sep. 2015.
- [9] H. Moghadas, M. Zandvakili, D. Sameoto, and P. Mousavi, "Beam-reconfigurable aperture antenna by stretching or reshaping of a flexible surface," *IEEE Antennas Wireless Propag. Lett.*, vol. 16, pp. 1337-1340, doi: 10.1109/LAWP.2016.2633964, Dec. 2016.
- [10] L. Di Palma, A. Clemente, L. Dussopt, R. Sauleau, P. Potier, and P. Pouliguen, "Circularly-polarized reconfigurable transmitarray in Ka-band with beam scanning and polarization switching capabilities," *IEEE Trans. Antennas Propag.*, vol. 65, no. 2, pp. 529-540, doi: 10.1109/TAP.2016.2633067, Feb. 2017.
- [11] W. Li, L. Bao, and Y. Li, "A novel frequency and radiation pattern reconfigurable antenna for portable device applications," *Applied Computational Electromagnetics Society (ACES) Journal*, vol. 30, no. 12, pp. 1276-1285, <https://journals.riverpublishers.com/index.php/ACES/article/view/10291>, Dec. 2015.
- [12] A. M. Morishita, C. K. Y. Kitamura, A. T. Ohta, and W. A. Shiroma, "A liquid-metal monopole array with tunable frequency, gain, and beam steering," *IEEE Antennas Wireless Propag. Lett.*, vol. 12, pp. 1388-1391, doi: 10.1109/LAWP.2013.2286544, Oct. 2013.
- [13] O. A. Barro, M. Himdi, and O. Lafond, "Reconfigurable radiating antenna array using plasma tubes," *IEEE Antennas Wireless Propag. Lett.*, vol. 15, pp. 1321-1324, doi: 10.1109/LAWP.2015.2507066, 2016.
- [14] I. F. da Costa, A. Cerqueira S., D. H. Spadoti, L. G. da Silva, J. A. J. Ribeiro, and S. E. Barbin, "Optically controlled reconfigurable antenna array for mm-wave applications," *IEEE Antennas Wireless Propag. Lett.*, vol. 16, pp. 2142-2145, doi: 10.1109/LAWP.2017.2700284, May 2017.
- [15] A. Patnaik, D. Anagnostou, C. G. Christodoulou, and J. C. Lyke, "Neurocomputational analysis of a multiband reconfigurable planar antenna," *IEEE Trans. Antennas Propag.*, vol. 53, no. 11, pp. 3453-3458, doi: 10.1109/TAP.2005.858617, Nov. 2005.
- [16] F. Zardi, P. Nayeri, P. Rocca, and R. Haupt, "Artificial intelligence for adaptive and reconfigurable antenna arrays: a review," *IEEE Antennas Propag. Mag.*, vol. 63, no. 3, pp. 28-38, doi: 10.1109/MAP.2020.3036097, June 2021.
- [17] B. Sheen, J. Yang, X. Feng, and M. M. U. Chowdhury, "A deep learning based modeling of reconfigurable intelligent surface assisted wireless communications for phase shift configuration," *IEEE Open J. Commun. Soc.*, vol. 2, pp. 262-272, doi: 10.1109/OJCOMS.2021.3050119, Jan. 2021.
- [18] O. P. Acharya, A. Patnaik, and S. N. Sinha, "Comparative study of bio-inspired optimization techniques in antenna array failure compensation," in *Proc. IEEE Int. Symp. Antennas Propag. (APSURSI)*, Orlando, FL, USA, pp. 1232-1233, doi: 10.1109/APS.2013.6711276, 2013.
- [19] R. Lovato and X. Gong, "Phased antenna array beamforming using convolutional neural networks," in *IEEE Int. Symp. Antennas Propagat. and USNC-URSI Radio Science Meeting*, Atlanta, GA, USA, pp. 1247-1248, doi: 10.1109/APUSNCURSINRSM.2019.8888573, 2019.
- [20] J. H. Kim and S. W. Choi, "A deep learning-based approach for radiation pattern synthesis of an array antenna," *IEEE Access*, vol. 8, pp. 226059-226063, doi: 10.1109/ACCESS.2020.3045464, Dec. 2020.

- [21] G. A. Harris, "Reconfigurable array control via convolutional neural networks," M.S. Thesis, Dept. Elect. Eng., Wright State Univ., Dayton, OH, 2021.
- [22] D. H. Werner, M. D. Gregory, and P. L. Werner, "A review of high performance ultra-wideband antenna array layout design," in *8th Eur. Conf. Antennas Propag. (EuCAP 2014)*, The Hague, Netherlands, pp. 3128-3131, doi: 10.1109/EuCAP.2014.6902490, 2014.
- [23] M. D. Gregory, F. A. Namin, and D. H. Werner, "Exploiting rotational symmetry for the design of ultra-wideband planar phased array layouts," *IEEE Trans. Antennas Propag.*, vol. 61, no. 1, pp. 176-184, doi: 10.1109/TAP.2012.2220107, Jan. 2013.
- [24] C. M. Stamper, "Reconfigurable antenna array using the PIN-diode-switched printed square spiral element," M.S. Thesis, Dept. Elect. Eng., Wright State Univ., Dayton, OH, 2021.
- [25] G. H. Huff, J. Feng, S. Zhang, and J. T. Bernhard, "A novel radiation pattern and frequency reconfigurable single turn square spiral microstrip antenna," *IEEE Microw. Wireless Compon. Lett.*, vol. 13, no. 2, pp. 57-59, doi: 10.1109/LMWC.2003.808714, Feb. 2003.
- [26] I. Goodfellow, Y. Bengio, and A. Courville, *Deep Learning*, MIT Press, Cambridge, MA, 2016.
- [27] M. Martinez-Ramon, A. Gupta, and J. L. Rojo-Álvarez, *Machine Learning Applications in Electromagnetics and Antenna Array Processing*, Artech House, Norwood, MA, 2020.



Garrett A. Harris received his B.S.E.E. at Wright State University in 2020 and the M.S.E.E degree in 2022 via the DoD SMART scholarship. While a student he was a member of IEEE and an adviser for the Ohio Mu chapter of Tau Beta Pi. Garrett has spent two summers at Wright State's Autonomy Technology Research Center internship with AFRL. His research interests include antenna design, remote sensing, and machine learning.

Corey M. Stamper received the B.S.E.E degree at Wright State University in 2020 and the M.S.E.E degree in 2021, also from Wright State University. His research interests are in applied electromagnetics, antenna design, and signal processing.

Michael A. Saville received the B.S.E.E., M.S.E.E., and Ph.D. degrees from Texas A&M University in 1997, the Air Force Institute of Technology in 2000, and the University of Illinois at Urbana-Champaign in 2006, respectively. He is currently Associate Professor of Electrical Engineering at Wright State University with a broad range of research interests in applied electromagnetics and applied signal processing. He is a Senior Member of IEEE, a registered Professional Engineer in Ohio, and Associate Editor for PIER Journal and IET Electronics Letters.

Flat-topped Beams using Phase Compensation based on Low-profile Transmitarray

Hui Zhang¹, Tianhang Lan¹, Shan Zhao², Qingqi He³, and Zengrui Li¹

¹The State Key Laboratory of Media Convergence and Communication, School of Information and Communication Engineering, Communication University of China, Beijing 100024 China
zhanghuicuc@hotmail.com, cuc_lth09@qq.com, zrli@cuc.edu.cn

²Beijing Institute of Graphic Communication, Beijing 102600, China
zhaoshan@bigc.edu.cn

³School of Electronic Engineering, Guangxi University of Science and Liuzhou 545006, China
qingqih@163.com

Abstract – This paper proposes a method to add an additional phase compensation to conventional phased arrays to achieve flat-topped beam forming, which can convert the spherical waves emitted by common conical horn antennas into cylindrical flat-topped beams, at the same time, there is also a certain power enhancement. A centrosymmetric unit composed of four layers of F4B and metal patches is designed. By changing the value of the parameters, a 360° phase change can be achieved, and it has the advantages of small size and low-profile. To validate the design concept, a prototype of the transmitarray (TA) was designed, fabricated, and measured by calculating the phase distribution of the front. The measurement results show that the designed TA can achieve flat-topped beams at 5.2GHz, the maximum gain is 1.15dB higher than that of the horn antenna, and the flat-topped range is about ±10°. The results are in good agreement with the simulation within the test range.

Index Terms – beam forming, flat-topped beams, horn antenna, low-profile, meta-surface, transmitarray.

I. INTRODUCTION

With fifth generation (5G) mobile communication technology developing rapidly, our lives have changed considerably. Beamforming (BF) plays an important role in this because BF can artificially control the direction and shape of the radiation wave to achieve high-efficiency energy propagation and reduce the propagation loss between the transmitting and receiving devices. It is becoming more and more widely applied in wireless communication systems. Commonly used BF target beams include differential beams, cosecant square beams, multi-beams and flat-topped beams.

They are often used in surveillance radar systems [1], broadcast and communication satellites [2], radio frequency circuits, wireless charging and drones [3].

Recently, various types of antennas with flat-topped beam radiation patterns have been attracting attention, and the advantage is that their radiated power is completely equal over a wide range of space. If the electromagnetic waves received by the receiving antenna are not uniform in density, the corresponding rectifier circuit design will become very complicated, because the internal diode is highly sensitive to power changes, resulting in a significant reduction in overall reliability and efficiency [4]. For the realization method of the flat-topped beams, many articles have been studied, such as directly feeding different antenna elements in the array to change the amplitude and phase in [5] or by designing a special feed network that is combined with a radiating antenna array [6]. In order to reduce the complexity of feeding the antenna array, planar arrays can be loaded with waveguides to control reactive loads around active radiating elements in the center [7] or sub-array topology optimization [8] to form flat-topped beams. In addition, the methods of synthesizing flat-topped beams using advanced optimization algorithms are also gradually maturing [9-11]. In contrast, antennas using a single feed are more suitable for the energy transmission environment in terms of complexity and practicability. Under the excitation of the microstrip slot antenna, a double-shell dielectric lens antenna [12] and a dielectric resonant antenna [13] based on the principle of combining eigenmodes have achieved good flat-topped performance. Combining the principle of metasurface, [14] designed an ultrathin linear graded index metasurface and a radial graded index metasurface lens, and realized a large-angle flat-topped beam by

controlling the microstrip patch antenna. To sum up, although these methods have completed the formation of flat-topped beams, they are more complicated to implement and generally larger in size. We hope to create a simple and fast method for realizing flat-topped beams.

A horn antenna, as a basic element of the antenna system, has the advantages of high gain, wide frequency band, low side lobes, etc. It is very suitable for wireless power transmission, but its maximum power is not flat-topped. TA can change the direction, shape and other characteristics of the received electromagnetic wave by controlling the phase of the elements and radiating it out. It also has the characteristics of no feeding resistance and low cost. Therefore, we aim to transform the spherical wave of the corresponding horn antenna into a flat-topped beam by changing the phase distribution of the TA without weakening the transmission gain of the horn antenna.

This paper is organized as follows. Section II details the principle of flat-topped BF and proposes a new 360° phase-shift unit for verification. Section III introduces the design of the TA, as well as the simulation and measurement results of the prototype. Section IV concludes the paper.

II. PRINCIPLE ANALYSIS

A. Flat-topped beamforming

In this section, the use of phase divergence for planar transmission arrays to generate flat-topped beams is discussed. The entire antenna system consists of a horn antenna placed along the z -axis with its focus at $z=-F$ and a flat square transmissive array placed along the xy plane and centered at the origin. Assuming that the electromagnetic waves are radiated from the feed antenna located in the far field and all waves start from the center of the feed, in order to form a pencil beam along the $+z$ direction, the array theory [15] points that a plane composed of $N \times N$ elements, the phase compensation $\varphi_{a,b}$ of the elements (a,b) in row a and column b on the array should be

$$\varphi_{a,b} = k_c \left[\sqrt{F^2 + (pR_{a,b})^2} - F \right], \quad (1)$$

where k_c is the wavenumber of free space at the target frequency, p is the side length of each element in the transmission array, $R_{a,b}$ is the relative distances from the center of the element (a,b) on the array to the origin, which can be determined by the following equation

$$R_{a,b} = \sqrt{\left(a - \frac{N+1}{2}\right)^2 + \left(b - \frac{N+1}{2}\right)^2}. \quad (2)$$

Here, the phase compensation required by the entire unit is approximately replaced by the phase compensation at the center of each unit, and the phase

difference caused by the different spacing between the unit and the feed is balanced by assigning different phases to each unit. In this way the spherical waves emitted by the feed antenna can be transformed into plane waves. It can be seen that the phase compensation of the center unit of the array is 0°. Besides, as the value $R_{a,b}$ of the unit to the origin increases, the required phase compensation $\varphi_{a,b}$ also increases. In order to shape the radiation wave into a flat-topped beam, we add an extra phase $\varphi'_{a,b}$ to each element, which is also related to the element's position $R_{a,b}$, and its determination method is

$$\varphi'_{a,b} = k_c \left[\sqrt{F^2 + [F \tan(\theta_0 R_{a,b})]^2} - F \right], \quad (3)$$

where θ_0 is a fixed constant, which means that each unit can obtain different divergence degrees according to its own position. Finally, the phase $\Phi_{a,b}$ required for each unit is obtained by adding $\varphi_{a,b}$ and $\varphi'_{a,b}$ as

$$\Phi_{a,b} = \varphi_{a,b} + \varphi'_{a,b}. \quad (4)$$

B. Unit cell design and validation

The two basic requirements that the TA unit needs to have are a high transmission coefficient and 360° transmission phase coverage [16–17]. In this part, we propose a basic TA unit shown in Fig. 1, which has a sub-wavelength structure and ultra-thin three-dimensional size, and the overall structure is simple. The cell has a side length of $p = 18$ mm (about $\lambda/3$ at 5.2GHz), four layers of dielectric substrates are closely stacked, its material is F4B ($\epsilon_r=2.65$ and $\tan\delta=0.01$), and the outer surface of each layer is printed with square metal patches with a side length of s . As phase delay units, the metal patches can achieve 360° phase range by changing the size of its side length. The middle patch layer is a combination of a cross slot and a circular slot. Here, adding a circular slot on the cross slot can increase the transmission coefficient and reduce the reflection loss.

The unit cell was analyzed with the finite element method (FEM) employed by the full-wave simulation software CST Microwave Studio under periodic boundary conditions at sub-6GHz frequencies from 4.8-6 GHz. The incident wave was along the $+z$ direction at normal incidence. Then, the value of s is changed from 2 to 8 mm. The simulation results of the amplitude and phase of the transmission coefficient changing with frequency are shown in Fig. 2. At the target frequency of 5.2 GHz, the amplitude and phase change diagram of the transmission coefficient is shown in Fig. 3 (a). The unit transmission coefficients are all greater than -3 dB, and the phase coverage can reach more than 360°.

When the units are arranged in a transmission array, most of the units receive electromagnetic waves that are at an oblique incident angle from the feed horn antenna,

so the influence of oblique incidence should also be considered. Figure 3 (b) shows that the change of the incident angle has little effect on the unit performance, which is within an acceptable range.

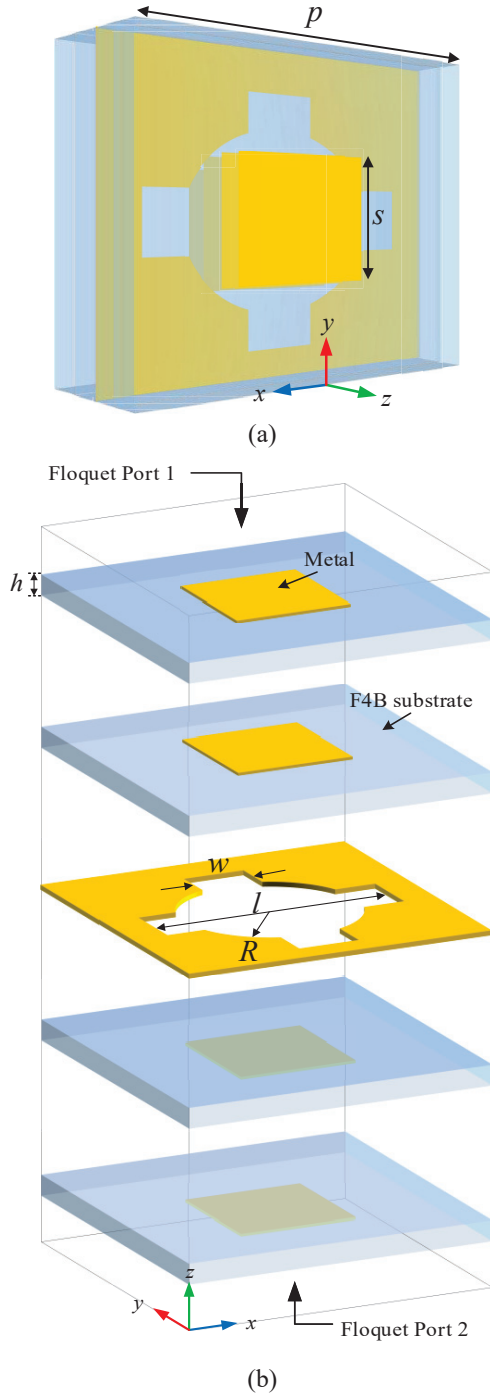


Fig. 1. Geometry of unit cell for TA: (a) perspective view and (b) schematic diagram of details. The specific structural parameters are set as $h = 1.5\text{mm}$, $w = 4\text{mm}$, $r = 7\text{mm}$, $l = 16\text{mm}$.

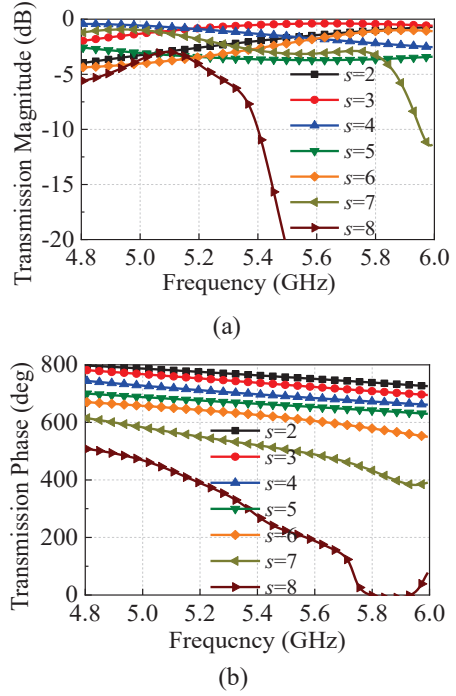


Fig. 2. Simulated transmission magnitude and phase of the unit cell under different frequencies: (a) magnitude and (b) phase.

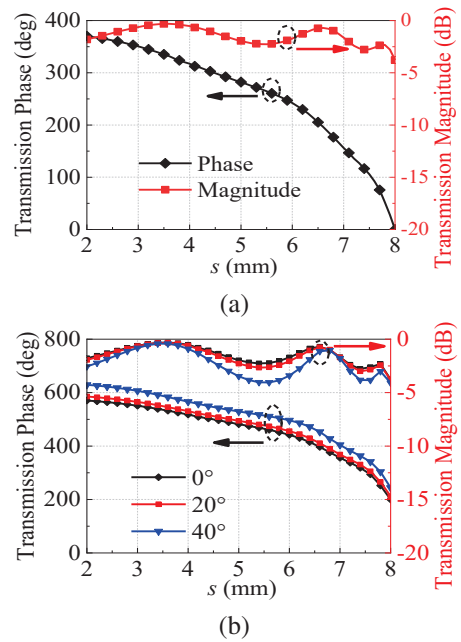


Fig. 3. Transmission magnitude and phase against s at 5.2GHz when: (a) vertical incidence and (b) oblique incidence.

C. Array design

In order to achieve flat-topped BF, 13×13 elements are selected to form a transmission array in our case,

there are 169 elements in total, and its overall size is $234\text{ mm} \times 234\text{ mm} \times 6\text{ mm}$ (about $4.05\lambda \times 4.05\lambda \times 0.1\lambda$ at 5.2GHz), which is reduced as much as possible while ensuring the performance, and the TA is excited by a linear polarized horn antenna.

Next, it is necessary to determine the position of the feed antenna, that is, to find the appropriate value of F/D . If its value is too large or too small, it will affect the spillover efficiency and illumination efficiency and reduce the efficiency of the antenna system [18]. In addition, if combined with the radiation pattern of the horn antenna when its maximum power drops by 10 dB, the radiation angle deviates from the maximum radiation direction θ , and $F/D = \cot(\theta)/2$ can be obtained. Here, we simulated the gain of the antenna system for different F/D values, and it can be seen from Fig. 4 (a) that the maximum gain is near 0.55. After further simulation, we finally choose the focal length $F=125\text{mm}$, and the corresponding F/D is about 0.53.

Using the theory described in Section II.A, the unit model proposed in Section II.B, and the position of the feed horn that has been determined, the phase $\Phi_{a,b}$ of each unit can be calculated by equation (4), and then the phase distribution of the entire array can be obtained. They are plotted in Fig. 4 (b).

Then, we need to determine the unit cell's size corresponding to the zero-phase point. When forming an array, in order to minimize the reflection loss, it is necessary to concentrate the cells with good transmission performance in the central part. At the same time, according to the description in [19], on the premise of hardly changing the cell phase, the sidelobe levels can be reduced by adjusting the unit cell's amplitude. First, according to the amplitude and phase variation diagram shown in Fig. 3 (a), $s = 6.7\text{ mm}$ is selected as the phase zero point through calculation. Then we try to adjust the unit amplitude, that is, change the size of r in the unit, and the obtained amplitude and phase vary with s is shown in Fig. 5, and there is only a slight phase change between different units. Ultimately, we chose $r = 5\text{ mm}$ elements for the middlemost section, $r = 8\text{ mm}$ elements for the surrounding sections, and $r = 7\text{ mm}$ elements for the edge sections. In this way, the transmission coefficient of the middle and surrounding parts is less than -1.5dB.

In order to further study the flat-topped beam pattern, the far-field 3D radiation patterns of the simulated horn antenna and the entire antenna system at 5.2 GHz are shown in Figs. 6 (a) and (b). Meanwhile, the electric field distribution on xz -plane and yz -plane are illustrated in Fig. 6 (c). Figure 6 (d) is the power-flow distribution on the corresponding xz - and yz -reference planes, respectively. The results show that after TA, the beam is focused from the original spherical shape to

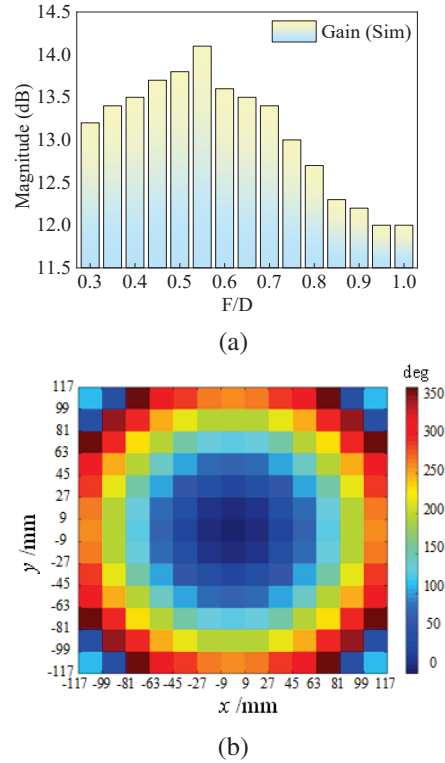


Fig. 4. (a) Simulated gain when changing the value of F/D and (b) required phase shift (in degrees) for the flat-topped beam forming when $F/D = 0.53$.

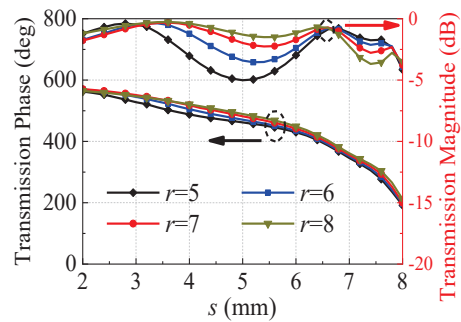


Fig. 5. Transmission magnitude and phase against s at 5.2GHz when varying r .

a columnar shape, and the gain is increased by about 1.15 dB. To make it more intuitive, Fig. 6 (c) and Fig. 6 (d) show that in the propagation direction of $+z$, electromagnetic waves radiate in the form of flat-topped beams, and the maximum transmission distance is about 300 mm (about 5.3λ at 5.2 GHz). The 2D pattern will be further analyzed in the next section.

D. Fabricated and measured

As shown in Fig. 7, a TA prototype was fabricated using PCB technology. The four-layer plate is fixed by

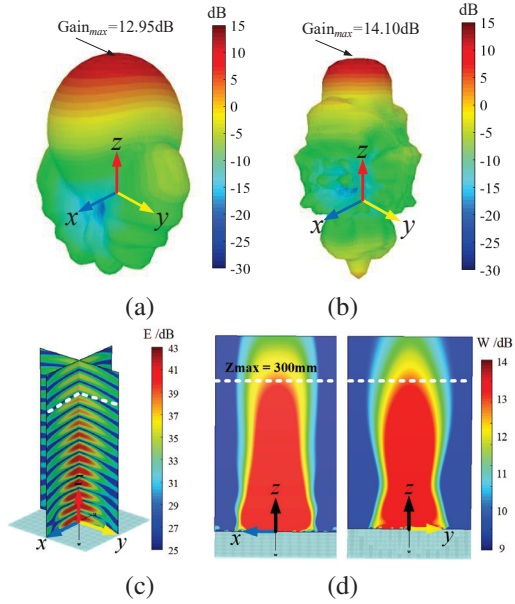


Fig. 6. 3-D simulated far-field radiation pattern for (a) feed horn and (b) antenna system. (c) Simulated electric field distribution on xz-plane and yz-plane. (d) Power-flow distribution on xz-plane (left) and yz-plane (right).

a washer and nylon screws. The TA antenna's radiation characteristics were performed in an anechoic chamber using the far-field measurement system. The chamber contains a probe and a feed horn. Its placement sequence and overall structure are shown in Fig. 7. The simulated and measured radiation patterns of the flat-topped beam in both principal planes (xz and yz) at 5.2 GHz are shown in Figs. 8 (a) and (b). The simulation and measurement results show good agreement. The incomplete match between them is caused by the measurement and the environment. It can be seen that the beam emitted by the feed horn is focused on the main beam direction after passing through the array, and at the same time, the maximum gain change does not exceed 1% within the range of $\pm 10^\circ$. The maximum gain of the feed horn selected for actual measurement is 12.95 dB, and the

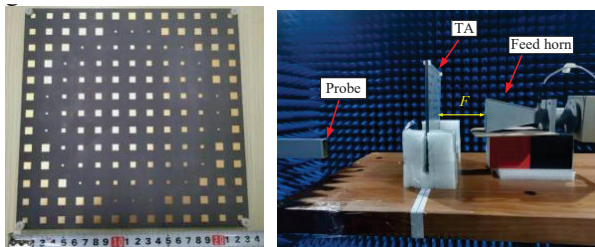


Fig. 7. Fabricated TA prototype and measurement setup in the anechoic chamber.

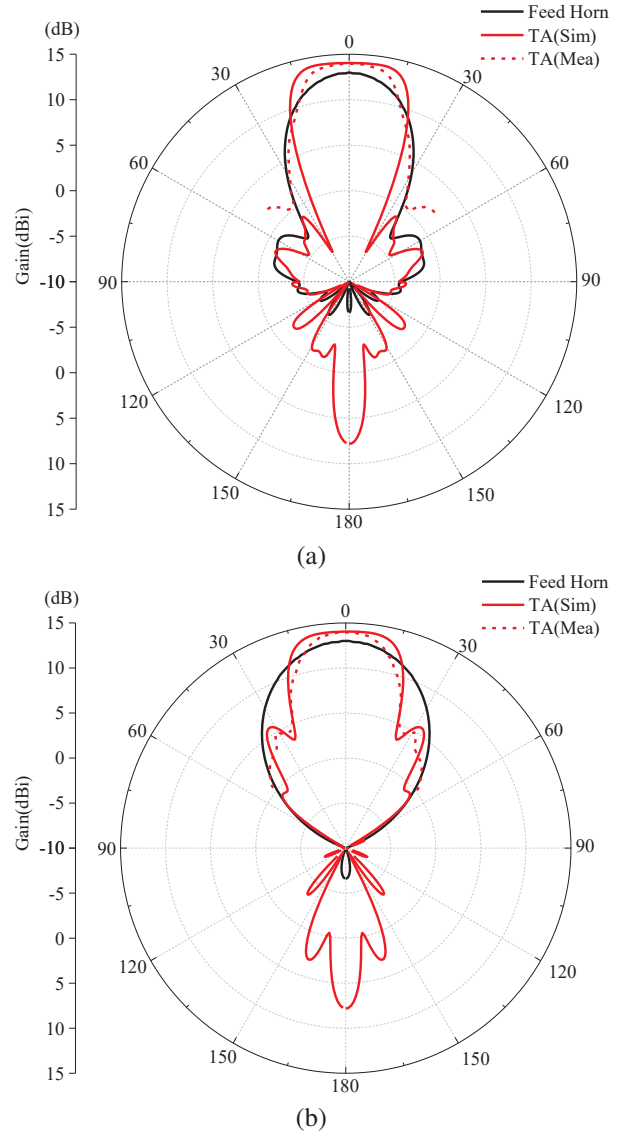


Fig. 8. Simulated and measured radiation patterns on (a) xz-plane and (b) yz-plane.

maximum gain of the system obtained by simulation and measurement is 14.07 dB and 14.05 dB, respectively. The simulated and measured sidelobe levels are -15.3 dB / -11.97 dB for the xz-plane and -8.37 dB / -9.25 dB for the yz-plane. This difference is related to the radiation pattern of the horn antenna, which can be clearly seen in the Fig. 8.

To illustrate the flat-topped effect, we refer to the shape factor (SF) of the bandpass filter, which is defined here as [3]:

$$SF = \frac{BW_{3dB}}{BW_{1dB}}. \quad (5)$$

Among it, BW_{3dB} and BW_{1dB} represent the 3 dB gain bandwidth to the 1 dB gain bandwidth of the antenna radiation pattern, respectively. The closer the

ratio is to 1, the better the flat-topped effect. For the selected horn antenna, the SFs of the xz -plane and yz -plane are 1.80 and 1.77, respectively. After passing through the antenna array, their sizes are 1.20 and 1.24, respectively, which indicates that the flat-topped beam forming effect is good.

The comparison between this work and previous flat-topped BF research are shown in Table 1. It can be seen from the table that compared with the published designs, this paper uses the form of TA to realize the flat-topped beams while maintaining a high gain, and the TA has the advantages of small size and simple structure.

III. CONCLUSION

In this paper, a new method for flat-topped BF is proposed. The whole antenna system consists of a horn antenna and a TA. By adding an extra phase gradient on the basis of the original phase compensation of the transmission array to change its refractive power, a flat-topped radiation pattern is realized in the direction of the main beam. For verification, a four-layer simple antenna element with 360° phase change is designed. We fabricated and measured a prototype of this antenna array after forming the array using the proposed theory. The experimental results show that at the operating frequency of 5.2 GHz, power enhancement to the corresponding horn antenna and a flat-topped pattern with a wide angle can be achieved. This method has a certain application value in wireless energy transmission. The array as a whole has the characteristics of miniaturization, low profile, simple structure, low cost, center symmetry, and can also be applied to other TA designs.

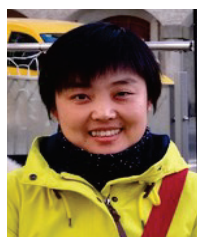
ACKNOWLEDGMENT

This work was supported by the National Natural Science Foundation of China (62101515) and the Fundamental Research Funds for the Central Universities.

REFERENCES

- [1] H. Chu, P. Li, and Y. Guo, "A beam-shaping feeding network in series configuration for antenna array with cosecant-square pattern and low sidelobes," *IEEE Antennas and Wireless Propagation Letters*, vol. 18, no. 4, pp. 742-746, Apr. 2019.
- [2] A. Aziz, F. Yang, S. Xu, and M. Li, "A low-profile quad-beam transmitarray," *IEEE Antennas and Wireless Propagation Letters*, vol. 19, no. 8, pp. 1340-1344, Aug. 2020.
- [3] N. Takabayashi, N. Shinohara, T. Mitani, M. Furukawa, and T. Fujiwara, "Rectification improvement with flat-topped beams on 2.45-GHz rectenna arrays," *IEEE Transactions on Microwave Theory and Techniques*, vol. 68, no. 3, pp. 1151-1163, Mar. 2020.
- [4] C. Cheng and K. Huang, "Synthesis of flat-topped beams in wireless power transmission," *Journal of Electronics and Information Technology*, vol. 40, no. 5, pp. 1115-1121, May 2018.
- [5] A. Li, B. Feng, and L. Deng, "A $\pm 45^\circ$ dual-polarized flat-topped radiation antenna array for 5G applications," *2021 IEEE 4th International Conference on Electronic Information and Communication Technology (ICEICT)*, Seoul, Korea, pp. 684-686, Apr. 2021.
- [6] L. Sun, "Design of beamforming network with flat-topped radiation patterns," *2021 IEEE MTT-S International Microwave Workshop Series on Advanced Materials and Processes for RF and THz Applications (IMWS-AMP)*, pp. 211-213, Nov. 2021.
- [7] R. T. Maximidis, A. B. Smolders, G. Toso, and D. Caratelli, "Planar reactively loaded array antenna with flat-top radiation pattern characteristics," *IEEE International Symposium on Antennas and Propagation and North American Radio Science Meeting, Montreal, QC, Canada*, pp. 2091-2092, July 2020.
- [8] R. Maximidis, D. Caratelli, G. Toso, and A. B. Smolders, "High-gain flat-top antenna sub-arrays for planar arrays with limited field of view," *14th European Conference on Antennas and Propagation (EuCAP)*, Copenhagen, Denmark, pp. 1-4, June 2020.
- [9] Y. Xu, X. Shi, W. Li, and J. Xu, "Flat-top beam pattern synthesis in range and angle domains for frequency diverse array via second-order cone programming," *IEEE Antennas and Wireless Propagation Letters*, vol. 15, pp. 1479-1482, Jan. 2016.
- [10] P. Angeletti, G. Buttazoni, G. Toso, and R. Vescovo, "Parametric analysis of flat top beam patterns generated by linear periodic arrays," *10th European Conference on Antennas and Propagation (EuCAP)*, Davos, Switzerland, pp. 1-2, Apr. 2016.
- [11] S. Khaefi, A. Mallahzadeh, and M. H. Amini, "Flat-topped pattern synthesis of optical leaky-wave antennas," *Optics Communications*, vol. 485, p. 126737, Mar. 2021.
- [12] N. T. Nguyen, R. Sauleau, and L. Le Coq, "Reduced-size double-shell lens antenna with flat-top radiation pattern for indoor communications at millimeter waves," *IEEE Transactions on Antennas and Propagation*, vol. 59, no. 6, pp. 2424-2429, June 2011.

- [13] C. K. Wang, B. J. Xiang, S. Y. Zheng, K. W. Leung, W. S. Chan, and Y. A. Liu, "A wireless power transmitter with uniform power transfer coverage," *IEEE Transactions on Industrial Electronics*, vol. 68, no. 11, pp. 10709-10717, Nov. 2021.
- [14] A. K. Singh, M. P. Abegaonkar, and S. K. Koul, "Wide angle beam steerable high gain flat top beam antenna using graded index metasurface lens," *IEEE Transactions on Antennas and Propagation*, vol. 67, no. 10, pp. 6334-6343, Oct. 2019.
- [15] A. H. Abdelrahman, F. Yang, A. Z. Elsherbeni, and P. Nayeri, *Analysis and Design of Transmitarray Antennas*, M&C Publishers, 2017.
- [16] J. Tang, X. Chen, X. Meng, Z. Wang, Y. Ren, C. Pan, X. Huang, M. Li, and A. A. Kishk, "Compact antenna test range using very small F/D transmitarray based on amplitude modification and phase modulation," *IEEE Transactions on Instrumentation and Measurement*, vol. 71, pp. 1-14, Feb. 2022.
- [17] X. Zhang, F. Yang, S. Xu, A. Aziz, and M. Li, "Dual-layer transmitarray antenna with high transmission efficiency," *IEEE Transactions on Antennas and Propagation*, vol. 68, no. 8, pp. 6003-6012, Aug. 2020.
- [18] M. Jiang, Z. N. Chen, Y. Zhang, W. Hong, and X. Xuan, "Metamaterial-based thin planar lens antenna for spatial beamforming and multibeam massive MIMO," *IEEE Transactions on Antennas and Propagation*, vol. 65, no. 2, pp. 464-472, Feb. 2017.
- [19] Q. Lou and Z. N. Chen, "Sidelobe suppression of metalens antenna by amplitude and phase controllable metasurfaces," *IEEE Transactions on Antennas and Propagation*, vol. 69, no. 10, pp. 6977-6981, Oct. 2021.



Hui Zhang received the Ph.D. degree in Communication and Information System from Beijing Jiaotong University, Beijing, China, in 2009. She is currently a Professor with the Communication University of China, Beijing. Her research interests include the areas of finite-difference time-domain (FDTD) methods, electromagnetic scattering, and microstrip antenna arrays.



Tianhang Lan received the B.Eng. degree in Communication Engineering from the Communication University of China, Beijing, China, in 2021. His current research interests include analysis and design of transmitarray antennas.



Shan Zhao received the Ph.D. degree from the School of Communication and Information System, Communication University of China, Beijing, China, in 2013. She is currently a lecturer at Beijing Institute of Graphic Communication, China. Her research interests include integral equation and frequency selective surface.



Qingqi He received the bachelor's degree in Electrical Engineering from Henan Polytechnic University, Jiaozuo, China in 2020. His current research interests include metasurfaces and their antenna applications.



Zengri Li received the B.S. degree in Communication and Information System from Beijing Jiaotong University, Beijing, China, in 1984, the M.S. degree in Electrical Engineering from the Beijing Broadcast Institute, Beijing, in 1987, and the Ph.D. degree in Electrical Engineering from Beijing Jiaotong University in 2009. He is currently a Professor with the Communication University of China, Beijing. He studied at Yokohama National University, Yokohama, Japan, from 2004 to 2005. His research interests include the areas of finite-difference time-domain (FDTD) methods, electromagnetic scattering, metamaterials, and antennas.

Design and Evaluation of Ultra-broadband Metamaterial Absorber for Energy Harvesting Applications

**Ebenezer Abishek¹, Elakkiya Azhagar², Manikandan Esakkimuthu³,
and Karthigeyan Arumugam⁴**

¹Associate Professor, Department of Electronics and Communication Engineering
Vel Tech Multi Tech Dr. Rangarajan Dr. Sakunthala Engineering College, Chennai-600062, India
ebenezerabishek@gmail.com

²Department of Electronics and Communication Engineering
Saveetha Engineering College, Chennai- 602105, India

³Center for Innovation and Product Development, School of Electronics Engineering
Vellore Institute of Technology, Chennai- 600127, India

⁴Department of Electronics and Communication Engineering
Vel Tech Rangarajan Dr. Sagunthala R&D Institute of Science
and Technology, Chennai- 600062, India

Abstract – A perfect metamaterial absorber (MMA) is designed and evaluated numerically for solar energy harvesting applications. A dielectric layer separates the top structured metallic plane and the bottom ground metallic plane that make up the MMA. The MMA structure is primarily presented in the range of 100-1000 THz, which corresponds to 3000-300 nm in wavelength, for the efficient utilization of solar energy. The results obtained in the band 441-998 THz correspond to a visible and ultraviolet wavelength range of 680-300 nm. It has achieved a maximum absorption rate of 99.9% at 700 THz and 99% between 500 and 800 THz, respectively. In the desired frequency bands, the structure has achieved polarization and angle-resolved behavior. The MMA-based absorber has a high absorption rate of over 90% in the broadest visible (400-700 nm) and UV (100-300 nm) spectra. Also shown are the absorption characteristics of the MMA-based solar cell in the infrared (IR) region. The band 345-440 THz, corresponding to 870-690 nm, has 75% absorption. The other IR band (240-345 THz), which corresponds to 1250-880 nm, has achieved absorption of nearly 50%. So it can be utilized for the entire visible solar spectrum, including infrared to ultraviolet. If the proposed MMA structure were equipped with the appropriate electrical circuitry, it could be utilized for solar energy harvesting.

Index Terms – absorber, energy harvesting, metamaterial, solar.

I. INTRODUCTION

The distinction between renewable and nonrenewable energy sources is made. Included in fossil fuels are coal, oil, and petroleum. Excessive use depletes resources. Natural gas will last 60 years, petroleum 40 years, and coal 200 years [1]. The combustion of these fuels in automobiles and power plants produces greenhouse gases that contribute to global warming. Renewable energies such as geothermal, tidal, hydroelectric, solar, and wind are all free. These resources are plentiful, non-perishable, and environment friendly. Energy demand has increased due to technological advancements, rising populations, and industrial expansion. Available fossil fuels cannot meet energy demands [2]. Solar energy is a renewable substitute for fossil fuels. Solar can be divided into three major regions: infrared (52%), visible (39%), and ultraviolet (9%), approximately. In one hour, solar emissions can meet the world's annual energy needs [3–4]. However, this source is difficult to harvest. Solar cells convert incident solar energy into electricity, but their low conversion efficiency presents a challenge for scientists. The material's bandgap corresponds to the absorption of incident photon energy. Solar cells convert absorbed electrons into electric current. The corresponding frequency band is in the range of 100-1000THz [7]. To improve absorption, scientists are researching nanomaterials and nanostructure-based absorbers, solar cell concentrators, embedded solar cell systems, etc. Solar trackers enhance absorption in accordance with

environmental conditions. A device with improved absorption characteristics is required to absorb incident energy regardless of polarization or angle. These issues must be addressed by solar cells. Non-natural metamaterials possess extraordinary properties, such as negative refraction and cloaking [8–9]. Metamaterials are used to construct electromagnetic (EM) energy absorbers that are more efficient. Metamaterials are synthetic materials with peculiar properties and benefits, such as evanescent wave amplification, invisibility cloaking, superlenses, electromagnetic filters, sensors, antennas, high-frequency polarization rotators, a negative refractive index, and negative permeability [10–15]. This is not normal. Recently, there has been increased interest in metamaterials as absorbers [16–20]. A metamaterial absorber (MMA) can collect sunlight to increase the efficiency of solar cells. In the THz and microwave regions, MMA was developed for shielding, sensing, etc. Perfect index sensing based on MMA is also described [21]. The resonance of MMA is governed by geometric parameters and material properties [22]. Exotic, high-frequency MMA is created between the visible and ultraviolet regimes [23–30]. Similar outcomes are observed in the infrared [31–34]. These are narrowband designs. Many MMA competitors used low-frequency techniques. Therefore, the design of solar MMA must have broad absorption. Solar energy harvesting will require a broadband metamaterial absorber. In this paper, a new MMA structure with broadband absorption characteristics is designed. Variations in the geometric parameters of the structure produce different absorption characteristics. It absorbs infrared, visible, and ultraviolet radiation. The engineered structure possesses pseudo-plasmon frequencies. By optimizing the model's geometric parameters and dielectric substrate, its resonance is modified. 90% of visible light is absorbed, with a peak absorption of 99% in the 500-800THz band. As a reflector, the bottom metal plate increases absorption.

II. MATERIALS AND STRUCTURE

The perspective view of the proposed MMA and the boundary conditions are shown in Figs. 1 (a) and (b), respectively. The numerical simulation of the designed structure is carried out using CST Microwave Studio software in a high-frequency finite element analysis approach. The structure has three layers: a structured top metallic patch, a bottom metallic ground plane, and an intermediate dielectric substrate. The metal is tungsten (W), and the substrate is silicon dioxide (SiO_2). The properties of these materials at the desired frequencies are used as given by Ghosh (1999) and Palik (1997). The advantages of using tungsten are that it has a higher melting point and better solar absorption characteristics than the other metals. Furthermore, SiO_2 allows

for greater flexibility in solar cell integration, which improves absorption even further. This eases the fabrication process as well.

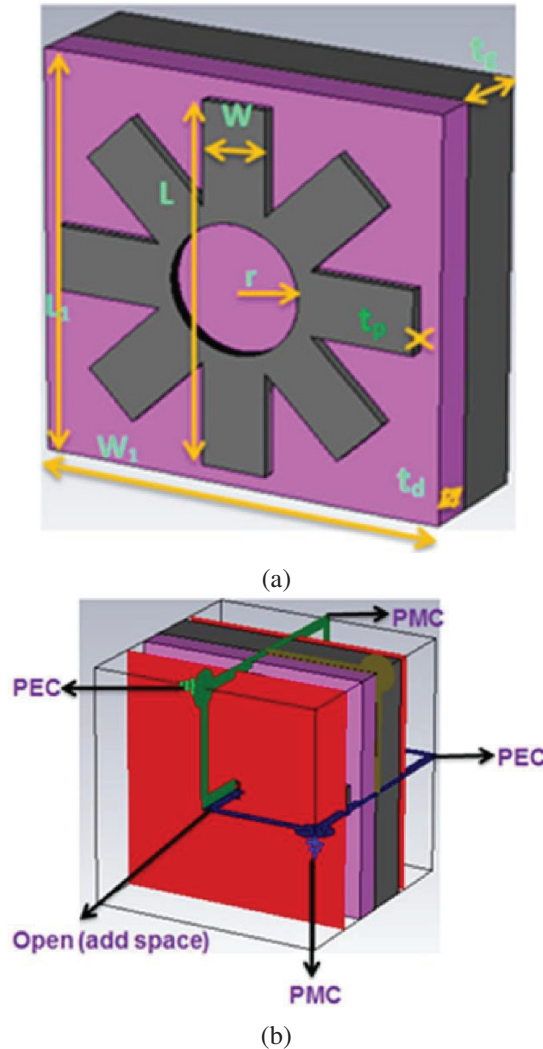


Fig. 1. (a) Geometry of the unit cell of the proposed MMA, perspective view. [Geometrical parameters: $L_1 = W_1 = 500$ nm, $W = 80$ nm, $L = 450$ nm, $r = 80$ nm, $t_p = 15$ nm, $t_d = 60$ nm, $t_g = 100$ nm], (b) Boundary conditions.

III. ABSORPTION AND SIMULATION STUDIES

In simulation, unit cell periodic boundary conditions in the x and y directions and open space in the z -direction are utilized. The wave is incident on the top metallic patch using the floquet port, and the output is measured at the backside of the bottom ground plane. This kind of setup avoids any near-field problems. By using parametric analysis, the best dimensions for the proposed MMA

can be found and are shown in Fig. 1 (a). The electromagnetic spectrum is divided into different regions, but the majority of solar energy that reaches the earth belongs to the visible, infrared, and ultraviolet (UV) regions. So this region, i.e., 100-1000 THz, is chosen for the analysis, and the MMA is designed. The incident solar EM radiation may be either absorbed, reflected, or transmitted. The absorption value is calculated indirectly by obtaining the reflection and transmission values. For better absorption, reflection and transmission should be kept to a minimum. The thickness of the bottom ground plane is kept higher to avoid any transmission through it, i.e., a thinner layer transmits more. The transmitted wave power is considered to be zero due to the presence of a metallic ground plane that reflects the incident EM radiation. So the objective is to minimize the reflection. The following will be used for the calculation of the absorption:

$$A(\omega) = 1 - R(\omega). \tag{1}$$

From equation (1) it is evident that for obtaining maximum absorption $A(\omega)$, the reflection $R(\omega)$ in the structure should be kept minimum. This can be achieved by proper impedance matching where the free space impedance matches with the structure impedance ($Z_{in} = Z_o$). Therefore, the transmission and reflection should be negligible for obtaining better absorption characteristics.

IV. RESULTS AND DISCUSSION

The obtained absorption, reflection, and transmission characteristics of the proposed structure for the desired geometrical parameters are shown in Fig. 2. The proposed MMA has obtained near-perfect absorption of about 99.9% at the frequency of 700 THz, with broadband absorption behavior of about 90% in the entire solar spectrum. The amount of light that is absorbed is more than 90% across the entire range of visible and ultraviolet (UV) light. The bottom metallic layer acts as a good reflector, and in addition, the lossy nature of the dielectric supports perfect absorption. The dielectric substrate and unit cell dimensions will determine the resonance. The structured top metallic patch determines the resonant characteristic of the MMA. As a result, all of these must be carefully chosen in order to achieve perfect absorption in the desired band.

From the wavelength vs. absorption spectrum, the respective frequency is extracted. The absorption characteristics of the proposed MMA are also observed for wider frequency ranges, including infrared (IR), visible light, and UV regions, which are shown in Fig. 3.

It is obvious that absorption of more than 70% is seen even in the infrared region between 300 and 430 THz, which is an indicator that the proposed structure can also be utilized for IR photodetector applications.

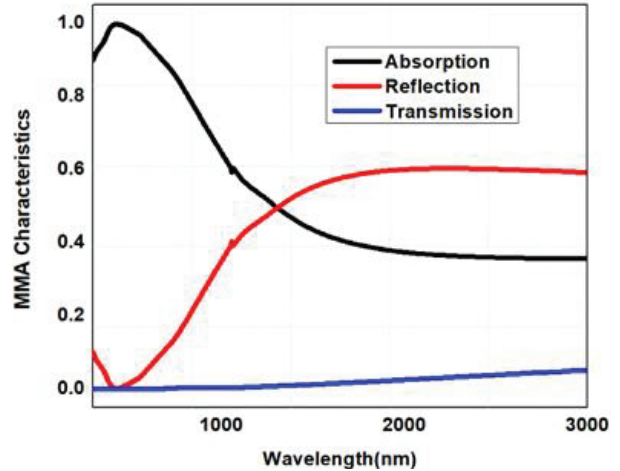


Fig. 2. Wavelength versus characteristics of the designed MMA.

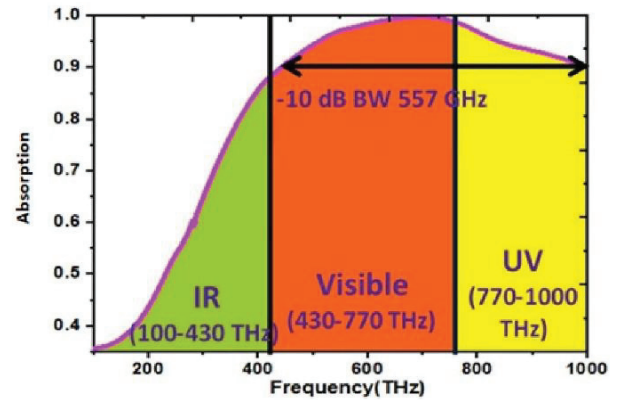
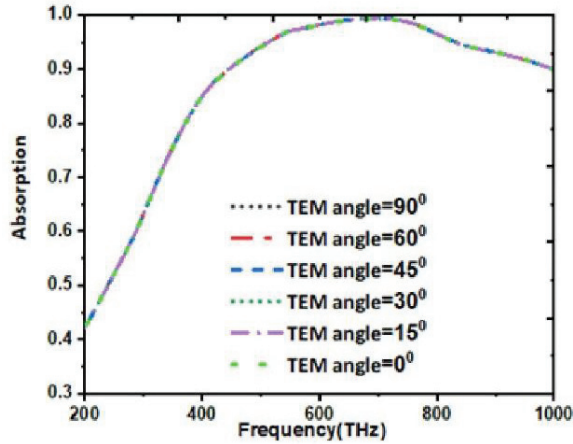


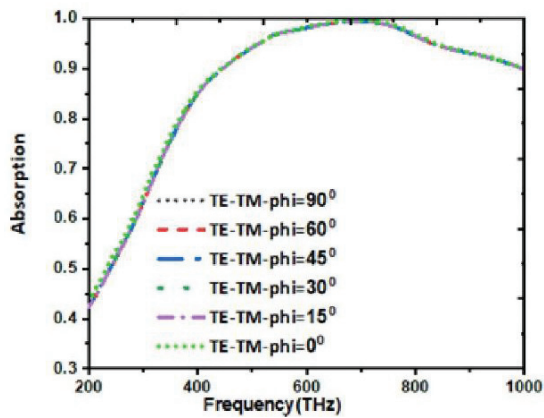
Fig. 3. The absorption rate of the proposed structure in the solar light regime (100-1000 THz).

Likewise, it is clear that the absorption value of the proposed MMA in the UV region is also above 90% in the frequency range between 770 and 1000 THz. Based on these features, it can be said that the proposed MMA can be used not only for solar energy harvesting but also as a photodetector.

Figures 4 (a) and 4 (b) show the absorption characteristics of the designed structure for different modes at various angles of incidence. This is evidence for the proposed structure’s absorption characteristics, independent of the incidence angles varying from 0° to 90°. Therefore, the proposed structure could be utilized for absorbing the incident solar energy even at different incidence angles for all polarizations. Since most research only looks at transverse electric (TE) and transverse magnetic (TM) polarization, this adds importance to the proposed structure for analysis.



(a)



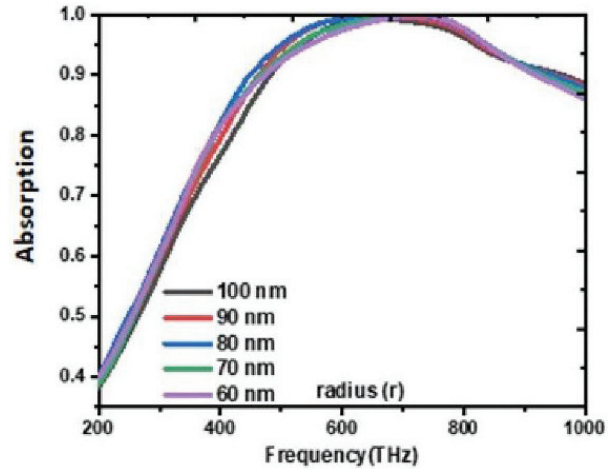
(b)

Fig. 4. (a) The absorption spectra TEM mode various incident angles for TE mode. (b) The absorption spectra TEM mode for various incident angles for TM mode.

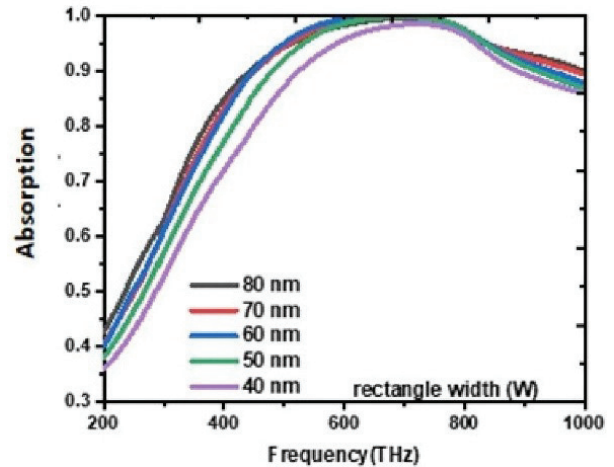
V. PARAMETRIC ANALYSIS

The geometrical parameters of the proposed structure are depicted in Fig. 1. The parametric study can be used to find out how the size of a part affects the frequency at which it works. The study is done for three geometric parameters, each of which is changed one at a time, and their absorption properties are found.

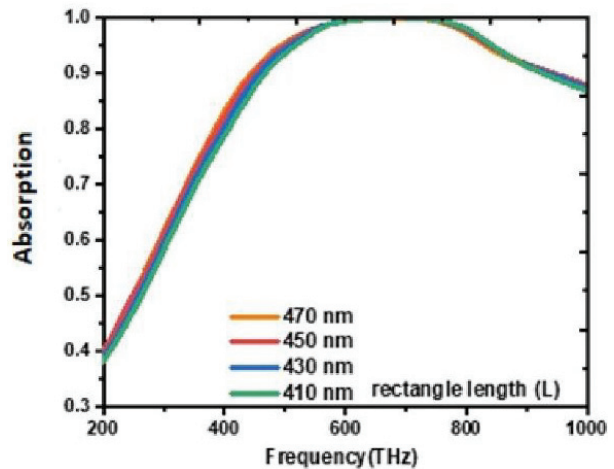
The effects of changing the inner radius (r), rectangle width (W), and rectangle length (L) of the patch on the absorption spectra are as follows. By changing r from 60 to 100 nm (keeping W at 80 nm, L at 450 nm), W from 40 to 80 nm (keeping L at 450 nm, r at 80 nm), and L from 410 to 470 nm (keeping W at 80 nm, r at 80 nm), the resonance modes drift to lower frequencies, as shown in Figs. 5 (a), (b), and (c), respectively. From this analysis, the parameters $r = 80$ nm, $W = 80$ nm, and $L = 450$ nm are chosen as the desired parameters for the designed structure for better absorption.



(a)



(b)



(c)

Fig. 5. (a) absorption rate changes with respect to radius, (b) absorption rate changes with respect to rectangle width, and (c) absorption rate changes with respect to rectangle length.

VI. FIELD DISTRIBUTIONS AND ANALYSIS

For understanding the primary physical mechanism of the proposed MMA, the distributions of the electric field at the three resonant frequencies are shown in Figs. 6 (a-c). A similar star-shaped resonator without any aperture was presented [22]. But it was focused only on the visible region and obtained a bandwidth of around 300 THz. In considering three bands (IR, visible, and UV), three peak resonant frequencies (441 THz, 700 THz, and 998 THz) are chosen for analysis. The electric field distribution confirms that only vertical and diagonal elements are contributing at 441 THz, but all elements are participating at 700 THz. It is noted that in addition to the resonating elements, the circular aperture and the substrate also contribute to the third resonance, i.e., 998 THz. This is how the proposed design is differentiated to absorb different regions of the solar spectrum [22]. The corresponding y-component of the magnetic field distributions is also depicted in Figs. 6 (d-f). For the resonances at 441 THz and 700 THz, the magnetic field is high throughout the whole patch structure and in the dielectric substrate layer as well. Also observed is the excitation of quad polar, octa polar, and other higher resonances in the magnetic field distribution analysis.

The current distributions through the surface of the metamaterial are also observed and shown in Figs. 6 (g-i). At 441 THz, vertical and diagonal resonating elements are responsible. Similarly, at 700 THz and 998 THz, the circular aperture and the entire resonator are contributing to the respective resonances.

In order to validate the importance of this work, the results are compared with the recent literatures related to this work and shown in Table 1.

Table 1: Comparison between the earlier studies in the literature and proposed absorber

Ref.	Band (THz)	Obtained Bandwidth (GHz) (Absorption > 90%)
[17]	69-72	5
[19]	75-85	10
[31]	40-70	30
[29]	60-115	55
[30]	175-300	125
[22]	430-770	340
[6]	450-700	250
[34]	500-800	300
[7]	300-500	200
This work	441-998	557

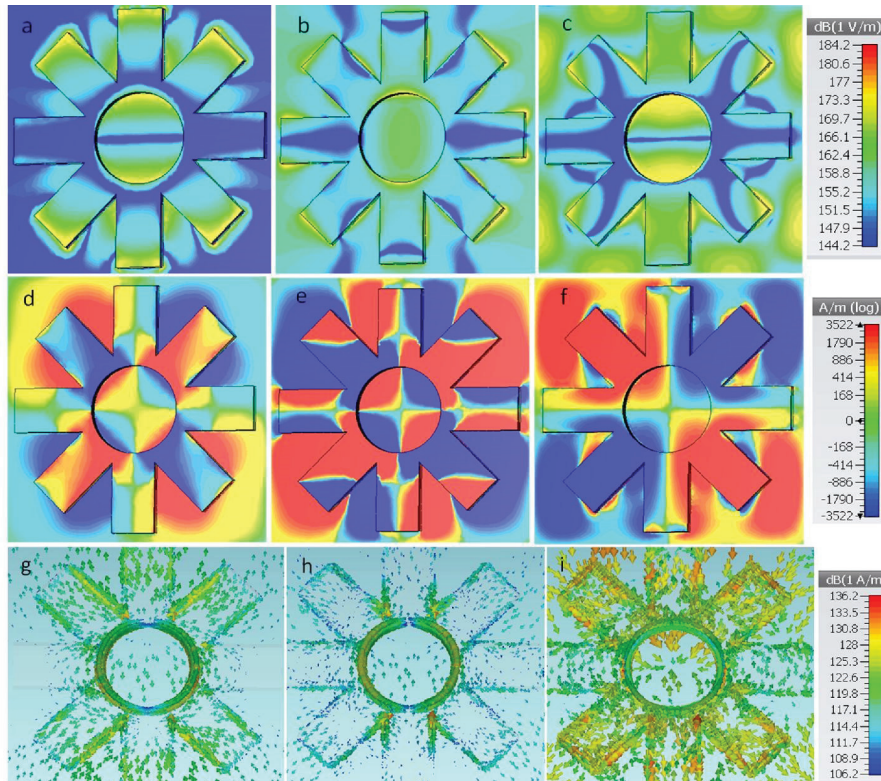


Fig. 6. (a-c) Electric field; (d-f) magnetic field; (g-i) surface current distributions for the three resonances 441 THz, 700 THz, and 998 THz, respectively.

The absorption value and the bandwidth determine the performance of the structure. The absorption rate of a minimum of 90% is considered for the analysis. A comparison with the literature is presented in Table 1 given above. The important point to note is that the proposed structure achieved broadband operation with better absorption characteristics than the previously reported works. It is evident that the structure is simple and obtained a broadband absorption of 557 GHz bandwidth, which is 2-3 times better than the earlier reported works.

The structure's thickness is 175 nm, indicating that it is thinner and more flexible. This absorption capability and size makes it efficient for capturing solar radiation. Independently, it can work as an energy harvesting module with proper electrical circuits, or it can be integrated with the solar cell as an absorbing medium.

Fabrication Feasibility and Real-time Characterization:

The proposed structure has two materials: a dielectric substrate and the conducting patch/ground plane. The conducting material, copper, can be deposited using the sputtering technique, which can yield the nm thickness easily. The major advantage of this proposed structure is that the dimensions are in the order of 100 nm with a minimum feature of 80 nm. Using a lithography process like E-beam or etching techniques like reactive ion etching, the minimum feature with high resolution could be achieved. Overall, the proposed structure is simple to fabricate with the mentioned facilities. The real-time measurements can be done with UV-visible spectroscopy for the absorption characteristics.

VII. CONCLUSION

A three-layered ultra-broadband MMA is designed and evaluated numerically. The structure absorbs 99.9% of 700 THz and 99% of 500-800 THz. It absorbs over 90% of visible (400-700) nm and UV (100-200) nm light. The MMA-based solar cell for the infrared absorption is also studied, i.e., 345-440 THz, or 870-680 nm in wavelength which is having around 75% absorption. The other IR band (1250-870 nm/240-345 THz) absorbs nearly 50% of the incident radiation. The structure has polarisation and angle-resolved behaviour in the desired bands. Resonance electric and magnetic field distribution analysis investigates broadband absorption. By integrating proper electrical circuits to the MMA, incident energy can be directly converted into electrical energy. This W-SiO₂ absorber could be used for detector application also.

REFERENCES

[1] B. Li, L. Wang, B. Kang, P. Wang, and Y. Qiu, "Review of recent progress in solid-state dye-

- sensitized solar cells," *Solar Energy Materials and Solar Cells*, vol. 90, no. 5, pp. 549-573, 2006.
- [2] M. P. Ustunsoy and C. Sabah, "Dual-band high-frequency metamaterial absorber based on patch resonator for solar cell applications and its enhancement with graphene layers," *Journal of Alloys and Compounds*, vol. 687, pp. 514-520, 2016.
- [3] A. V. Getman, M. G. Dushejko, A. V. Ivashchuk, M. S. Fadieiev, and Y. I. Yakymenko, "Influence of the carrier lifetime on the silicon solar cells radiation resistance," *IEEE 34th International Scientific Conference on Electronics and Nanotechnology (ELNANO)*, pp. 227-229, 2014.
- [4] Z. L. Wang and W. Wu, "Nanotechnology-enabled energy harvesting for self-powered micro/nanosystems," *Angew. Chem. Int. Ed.*, vol. 51, pp. 11700-11721, 2012.
- [5] F. Dincer, O. Akgol, M. Karaaslan, E. Unal, and C. Sabah, "Polarization angle independent perfect metamaterial absorbers for solar cell applications in the microwave, infrared, and visible regime," *Progress in Electromagnetics Research*, vol. 144, pp. 93-101, 2014.
- [6] P. Rufangura and C. Sabah, "Dual-band perfect metamaterial absorber for solar cell applications," *Vacuum*, vol. 120, part B, pp. 68-74, 2015.
- [7] B. Mulla and C. Sabah, "Perfect metamaterial absorber design for solar cell applications," *Waves in Random and Complex Media*, vol. 25, no. 3, pp. 382-392, 2015.
- [8] Y. Avitzour, Y. A. Urzhumov, and G. Shvets, "Wide-angle infrared absorber based on a negative-index plasmonic metamaterial," *Phys. Rev. B*, vol. 79, pp. 045131-045136, 2009.
- [9] J. Wang, C. Fan, P. Ding, J. He, Y. Cheng, W. Hu, G. Cai, E. Liang, and Q. Xue, "Tunable broad-band perfect absorber by exciting of multiple plasmon resonances at optical frequency," *Opt Express*, vol. 20, no. 14, pp. 14871-14878, 2012.
- [10] B. Wang, T. Koschny, and C. M. Soukoulis, "Wide-angle and polarization-independent chiral metamaterial absorber," *Phys. Rev. B*, vol. 80, pp. 033108-033111, 2009.
- [11] B.-X. Wang, X. Zhai, G.-Z. Wang, W.-Q. Huang, and L.-L. Wang, "Frequency tunable metamaterial absorber at deep-subwavelength scale," *Opt. Mater. Express*, vol. 5, pp. 227-235, 2015.
- [12] R. A. Shelby, D. R. Smith, and S. Schultz, "Experimental verification of a negative index of refraction," *Science*, vol. 292, no. 5514, pp. 77-79, 2001.
- [13] D. R. Smith, W. J. Padilla, D. C. Vier, S. C. Nemat-Nasser, and S. Schultz, "Composite medium with simultaneously negative permeability

- and permittivity,” *Phys. Rev. Lett.*, vol. 84, no. 18, pp. 4184-4187, 2000.
- [14] N. I. Landy, S. Sajuyigbe, J. J. Mock, D. R. Smith, and W. J. Padilla, “Perfect metamaterial absorber,” *Phys. Rev. Lett.*, vol. 100, pp. 207402-207405, 2008.
- [15] L. Huang and H. Chen, “Multi-band and polarization insensitive metamaterial absorber,” *Progress in Electromagnetics Research*, vol. 113, pp. 103-110, 2011.
- [16] J. Yang, S. Qu, H. Ma, J. Wang, and Y. Pang, “Dual-band tunable infrared metamaterial absorber with VO₂ conformal resonators,” *Optics Communications*, vol. 402, pp. 518-522, 2017.
- [17] L. Li, Y. Yang, and C. Liang, “A wide-angle polarization-insensitive ultra-thin metamaterial absorber with three resonant modes,” *Journal of Applied Physics*, vol. 110, no. 6, pp. 063702, 2011.
- [18] W. Ma, Y. Wen, and X. Yu, “Broadband metamaterial absorber at mid-infrared using multiplexed cross resonators,” *Opt Express*, vol. 21, no. 25, pp. 30724-30730, 2013.
- [19] N. Liu, M. Mesch, T. Weiss, M. Hentschel, and H. Giessen, “Infrared perfect absorber and its application as plasmonic sensor,” *Nano Letters*, vol. 10, no. 7, pp. 2342-2348, 2010.
- [20] M. Bagmanci, M. Karaaslan, E. Unal, O. Akgol, M. Bakır, and C. Sabah, “Solar energy harvesting with ultra-broadband metamaterial absorber,” *International Journal of Modern Physics B*, vol. 33, no. 08, pp. 1950056, 2019.
- [21] W. Zhou, K. Li, C. Song, P. Hao, M. Chi, M. Yu, and Y. Wu, “Polarization-independent and omnidirectional nearly perfect absorber with ultra-thin 2D subwavelength metal grating in the visible region,” *Opt. Express*, vol. 23, pp. A413-A418, 2015.
- [22] M. Bağmanci, M. Karaaslan, E. Ünal, O. Akgöl, and C. Sabah, “Extremely-broad band metamaterial absorber for solar energy harvesting based on star shaped resonator,” *Optical and Quantum Electronics*, vol. 49, no. 7, 2017.
- [23] F. Dincer, M. Karaaslan, E. Unal, K. Delihacioglu, and C. Sabah, “Design of polarization and incident angle insensitive dual-band metamaterial absorber based on isotropic resonators,” *Progress in Electromagnetics Research*, vol. 144, pp. 123-132, 2014.
- [24] B. Mulla and C. Sabah, “Perfect metamaterial absorber design for solar cell applications,” *Waves in Random and Complex Media*, vol. 25, no. 3, pp. 382-392, 2015.
- [25] P. Pitchappa, C. P. Ho, P. Kropelnicki, N. Singh, D.-L. Kwong, and C. Lee, “Micro-electromechanically switchable near infrared complementary metamaterial absorber,” *Appl. Phys. Lett.*, vol. 104, no. 20, pp. 201114, 2014.
- [26] P. Rufangura and C. Sabah, “Polarization angle insensitive dual-band perfect metamaterial absorber for solar cell applications,” *Phys. Status Solidi C*, vol. 12, pp. 1241-1245, 2015.
- [27] X. Duan, S. Chen, W. Liu, H. Cheng, Z. Li, and J. Tian, “Polarization-insensitive and wide-angle broadband nearly perfect absorber by tunable planar metamaterials in the visible regime,” *Journal of Optics*, vol. 16, no. 12, 2014.
- [28] W. Zhou, K. Li, C. Song, P. Hao, M. Chi, M. Yu, and Y. Wu, “Polarization-independent and omnidirectional nearly perfect absorber with ultra-thin 2D subwavelength metal grating in the visible region,” *Opt. Express*, vol. 23, pp. A413-A418, 2015.
- [29] X. Ling, Z. Xiao, X. Zheng, J. Tang, and K. Xu, “Broadband and polarization-insensitive metamaterial absorber based on hybrid structures in the infrared region,” *Journal of Modern Optics*, vol. 64, no. 7, pp. 665-671, 2017.
- [30] F. Ding, J. Dai, Y. Chen, J. Zhu, Y. Jin, and S. I. Bozhevolnyi, “Broadband near-infrared metamaterial absorbers utilizing highly lossy metals,” *Sci Rep*, vol. 6, 2016.
- [31] X. Ling, Z. Xiao, and X. Zheng, “A three-dimensional broadband infrared metamaterial absorber based on the plasmonic and dipole resonance responses,” *Plasmonics*, vol. 13, pp. 175-180, 2018.
- [32] R. Feng, W. Ding, L. Liu, L. Chen, J. Qiu, and G. Chen, “Dual-band infrared perfect absorber based on asymmetric T-shaped plasmonic array,” *Opt Express*, vol. 22, no. 5, 2014.
- [33] N. Zhang, P. Zhou, S. Zou, X. Weng, J. Xie, and L. Deng, “Improving the mid-infrared energy absorption efficiency by using a dual-band metamaterial absorber,” *Progress in Natural Science: Materials International*, vol. 24, no. 2, pp. 128-133, 2014.
- [34] P. Rufangura and C. Sabah, “Design and characterization of a dual-band perfect metamaterial absorber for solar cell applications,” *Journal of Alloys and Compounds*, vol. 671, pp. 43-50, 2016.



Ebenezer Abishek is an associate professor in the Department of Electronics and Communication Engineering, Vel Tech Multi Tech Dr. Rangarajan Dr. Sakunthala Engineering College. Has more than 10 years of teaching experience. In July of 2019, he earned a Ph.D. in electronics and communication engineering from the Vels Institute of Science, Technology, and Advanced Studies (VISTAS). Antennas, and electromagnetism are his research interests. He has published 33 articles in Scopus-indexed journals, two in SCI-indexed journals. The ORCID assigned to him is 0000-0003-2908-7069.



Elakkiya Azhagar is an assistant professor in the Department of Electronics and Communication Engineering, Saveetha Engineering College. She earned her doctorate degree from Sri Sivasubramaniam Nadar College of Engineering (SSN) in Chennai, India. Her current research is on terahertz devices like metamaterial absorbers, antennas, and filters.



Manikandan Esakkimuthu earned his Ph.D. in electrical engineering from Anna University in 2019. Currently, he is a senior assistant professor at the Vellore Institute of Technology, Chennai, in the Center for Innovation and Product Development (CIPD) and the School of Electronics Engineering. His areas of research interest are sensors and micromachining.



Karthigeyan Arumugam earned his Ph.D. in information and communication engineering in 2022 from Anna University. Currently, he is an assistant professor in the Department of Electronics and Communication Engineering at Vel Tech Rangarajan Dr. Sagunthala R&D Institute of Science and Technology. His research interests currently include RF circuits and devices, terahertz applications, and hardware cybersecurity.

Narrow-band Circularly Polarized Antenna for Medical Microwave Imaging and Health Monitoring Applications

Bilal Guetaf¹, Abdelhalim Chaabane¹, Abderrezak Khalfallaoui¹, and Hussein Attia²

¹Laboratoire des Télécommunications-LT

Département d'Electronique et Télécommunications, Faculté des Sciences et de la Technologie

Université 8 Mai 1945 Guelma, BP 401, Guelma, 24000, Algeria

guettaf.bilal@univ-guelma.dz, abdelhalim.chaabane@univ-guelma.dz, khalfalloui.abderrezak@univ-guelma.dz

²Interdisciplinary Research Center for Communication Systems and Sensing, and Electrical Engineering Department

King Fahd University of Petroleum and Minerals, Dhahran, 31261, Saudi Arabia

hattia@kfupm.edu.sa

Abstract – In this paper, a circularly polarized printed monopole antenna (CPPMA) is proposed for medical microwave imaging and health monitoring applications. The proposed CPPMA is optimized to operate at the Industrial, Scientific and Medical (ISM) band. A prototype of the designed antenna is fabricated and printed on the low-cost FR-4 substrate that has a compact size of $34 \times 28 \times 1.5 \text{ mm}^3$. The simulated results indicate that the designed CPPMA operates between 2.425 GHz and 2.475 GHz while the measured results range between 2.32 GHz and 2.515 GHz. The designed CPPMA also reveals a circular polarization performance at 2.45 GHz (2.4386 GHz - 2.4633 GHz). The suitability of CPPMA for microwave imaging is confirmed by checking its aptitudes to detect the presence of breast tumors and brain strokes. A great detection capability is achieved for breast tumors and brain strokes of various sizes inserted at different positions with a high sensitivity to changes or anomalies in the dielectric properties of human tissues. In addition, the usefulness of the proposed CPPMA for wearable application is justified experimentally. Excellent agreement is achieved between the simulated results and the measured ones.

Index Terms – Breast tumor and brain stroke detection, circularly polarized printed monopole antenna (CPPMA), industrial scientific and medical (ISM) band, medical microwave imaging and health monitoring, phantom models, wearable antenna.

I. INTRODUCTION

The most commonly used medical imaging modalities for image reconstructions of human anatomy, tissues or organs include X-ray computed tomography, mammography, magnetic-resonance imaging, single photon

emission computed tomography-computerized tomography (SPECT-CT) and ultrasound. However, each one of these screening approaches are quite costly, painful and ionized [1].

To overcome the drawback of these methods, microwave imaging has gained the interest of many biomedical researchers because of its attractive features that include low-cost, safety, simplicity, high image resolution of the scanned body tissues, non-ionizing radiations and being non-invasive [2]. It is based on mono-static or multi-static radar-type measurements, and benefits from the marked dielectric contrast between healthy and diseased tissues. The mono-static radar imaging system that uses a single antenna to scan the body with mechanical movement is faster and more efficient. Whereas the multi-static radar imaging system that uses an antenna array is complex, expensive and time consuming [3].

Circularly polarized (CP) antennas enhance the performances of medical microwave imaging radar systems since they reduce indoor multi-path effects and body postures, reduce polarization mismatch losses, penetrate lossy dielectric materials of the human body tissues, and provide a robust detection of the tumors irrespective to the antenna orientation constraints [4]. Several antennas have been reported for biomedical applications such as those presented in [5–17], however, these antennas are linearly polarized and have only one use whether for cancer screening, stroke screening, or health monitoring. Thus, novel high-performance antennas are needed for several biomedical applications.

In this paper, a mono-static CPPMA of size $34 \times 28 \times 1.5 \text{ mm}^3$ is proposed at Industrial, Scientific and Medical (ISM) band for medical microwave imaging applications and health monitoring wearable applications. The proposed CPPMA is capable of detecting

breast tumors and brain strokes of various sizes inserted at different positions. This CPPMA may also be utilized for remote health monitoring systems because of its operation in the ISM band and circular polarization properties. This remote health monitoring system can keep track of a patient's medical information while they are at home, making it easier to diagnose and treat them as well as forecast when they will get sick and regulate their condition. Additional contributions presented in this work include: 1) the design and the fabrication of a simple and low-cost antenna for several biomedical applications: breast cancer detection, brain stroke detection and for health monitoring and wearable applications; 2) the introduction and the evaluation of the circular polarization performance for the detection of tumors; 3) the ability to detect very small breast tumors and strokes is validated through the use of phantom models; 4) the usefulness of the fabricated prototype for wearable health applications is justified experimentally; 5) the detection of strokes in the human head through the analysis of E-field, H-field and current density; 6) the evaluation of specific absorption rate (SAR) parameters on the breast, head and arm of the human body phantom.

All the simulations presented in this work are carried out using CST Microwave Studio software.

II. ANTENNA AND BODY PHANTOM MODEL DESIGN

A. Antenna design and evolution analysis

Figure 1 presents the geometry of the designed CPPMA. Its optimized dimensions are given in Table 1.

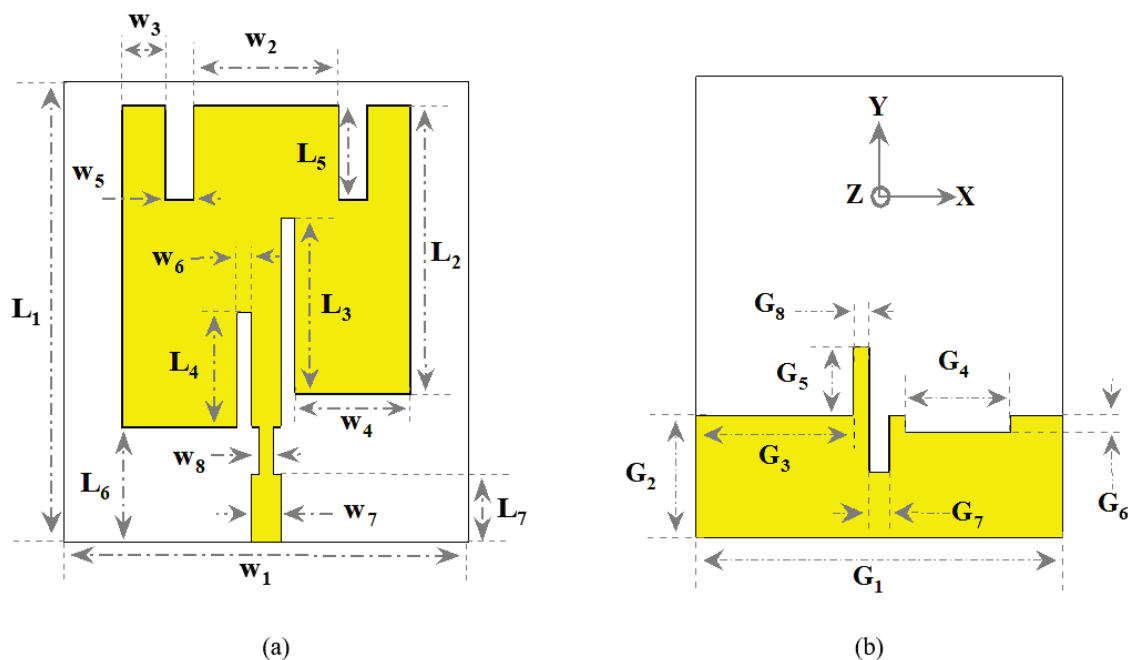


Fig. 1. Geometry of the designed CPPMA: (a) front view, (b) back view.

Figure 2 shows the evolution of the CPPMA design during the design process, whereas Fig. 3 describes the corresponding reflection coefficient and the axial ratio (AR) of the different designs.

The two slots and a stub inserted on the ground plane are responsible for generation of the circular polarization ($AR = 0.98 \text{ dB} < 3 \text{ dB}$ at 2.45 GHz, AR bandwidth ranges from 2.4386 GHz to 2.4633 GHz). This circular polarization performance can also be observed from the surface current direction as the phase augments in time. Figure 4 shows the current distributions on the surface of the proposed CPPMA at 2.45 GHz for four different phases (0° , 90° , 180° and 270°). It can be seen from the results that the main current direction for 0° is in the $-X$ direction, whereas the main current direction for 90° is in the $+Y$ direction. Besides, the main current direction at 180° and 270° are reverse to those of 0° and 90° , respectively. Accordingly, the main surface current turns in a clockwise trend. It signifies that a left-hand circular polarization (LHCP) is acquired in the direction of propagation with the designed CPPMA.

Figure 5 shows the simulated right-hand circularly polarized (RHCP) and LHCP far-field radiation patterns of the antenna in xz -plane (H-plane) and yz -plane (E-plane) at 2.45 GHz. It confirms that the proposed CPPMA radiates LHCP in the direction of the propagation and RHCP in the reverse direction. The minor inclinations of the radiation patterns in xz -plane (H-plane) are due to asymmetric geometry of the designed CPPMA. Comparable results are obtained in [18–19].

Table 1: Optimized dimensions of the proposed CPPMA

Parameter	W₁	L₁	W₂	W₃	W₄	W₅	W₆	W₇	W₈	L₂	L₃	L₄
Value (mm)	28	34	3	10	8	2	1	2	1	21.3	13	8.5
Parameter	L₅	L₆	L₇	G₁	G₂	G₃	G₄	G₅	G₆	G₇	G₈	
Value (mm)	7	8.7	5	28	9	12	8	5	1.25	1.6	1.2	

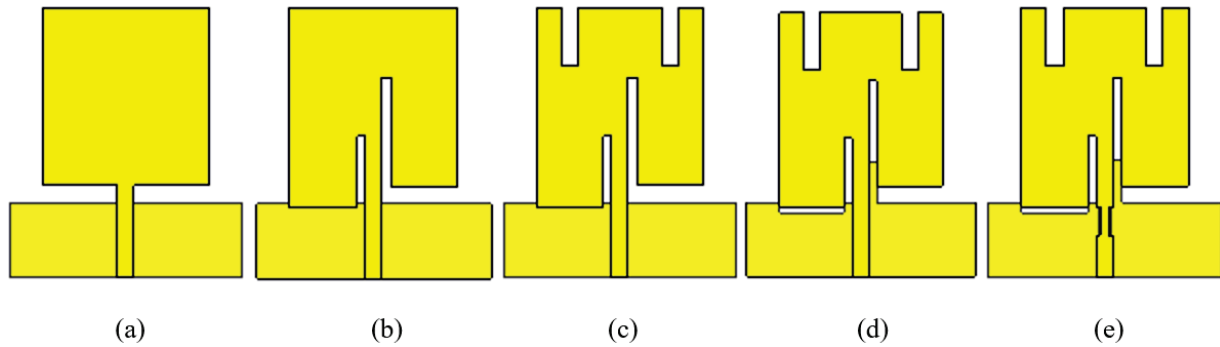


Fig. 2. The evolution of the proposed CPPMA during the design process: (a) Antenna 1, (b) Antenna 2, (c) Antenna 3, (d) Antenna 4, and (e) Proposed CPPMA.

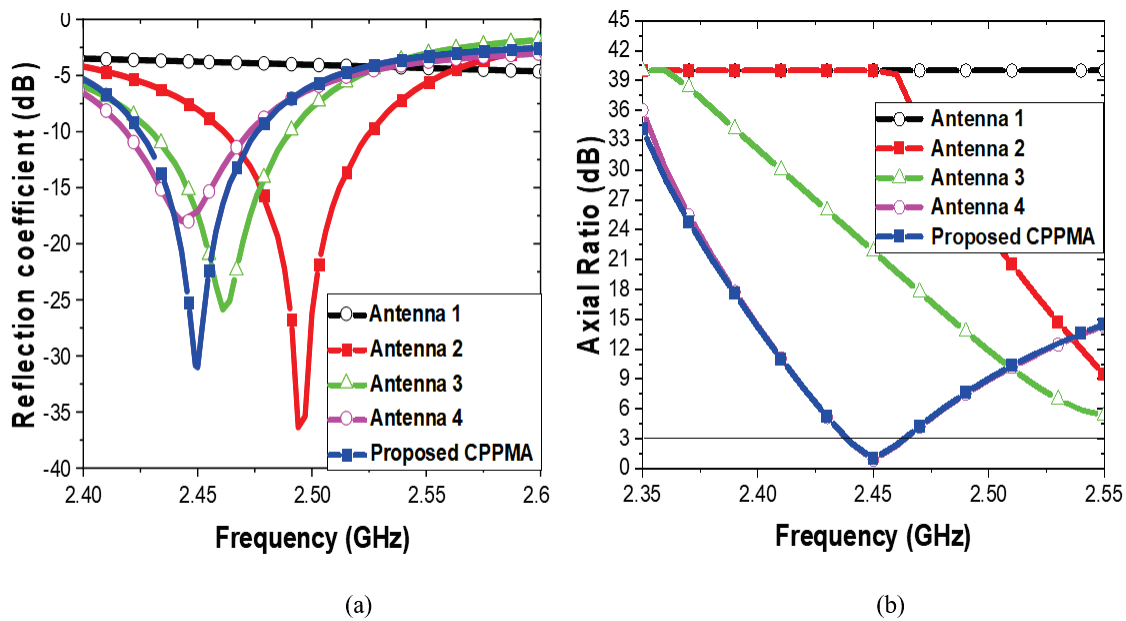


Fig. 3. (a) Reflection coefficient and (b) AR of the proposed CPPMA compared with the initial reference antennas.

A 3.01 dBi maximum directivity is achieved while a radiation efficiency of 92.49 % is attained at 2.45 GHz.

Figure 6 shows the fabricated prototype of the proposed CPPMA printed on FR4-Epoxy of size $34 \times 28 \times 1.5 \text{ mm}^3$. The prototype was fabricated using the PCB prototyping machine LPKF Proto Mat E44. Figure 7 presents the reflection coefficient setup mea-

surement using the R&S®ZNB Vector Network Analyzer. Figure 8 shows that the simulated and measured reflection coefficients of the CPPMA are in good agreement. The measured impedance bandwidth ranges between 2.32 GHz and 2.515 GHz while the simulated one varies between 2.425 GHz and 2.475 GHz.

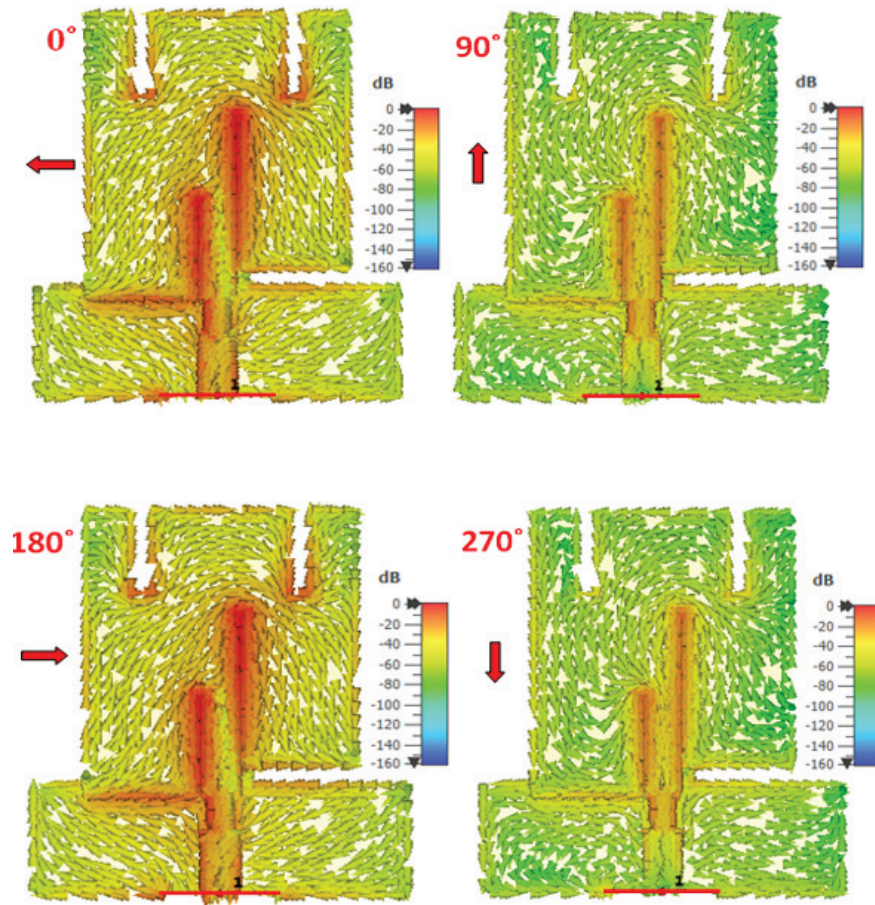


Fig. 4. Surface current distribution on the proposed CPPMA at 2.45 GHz for four different phases: 0° , 90° , 180° and 270° .

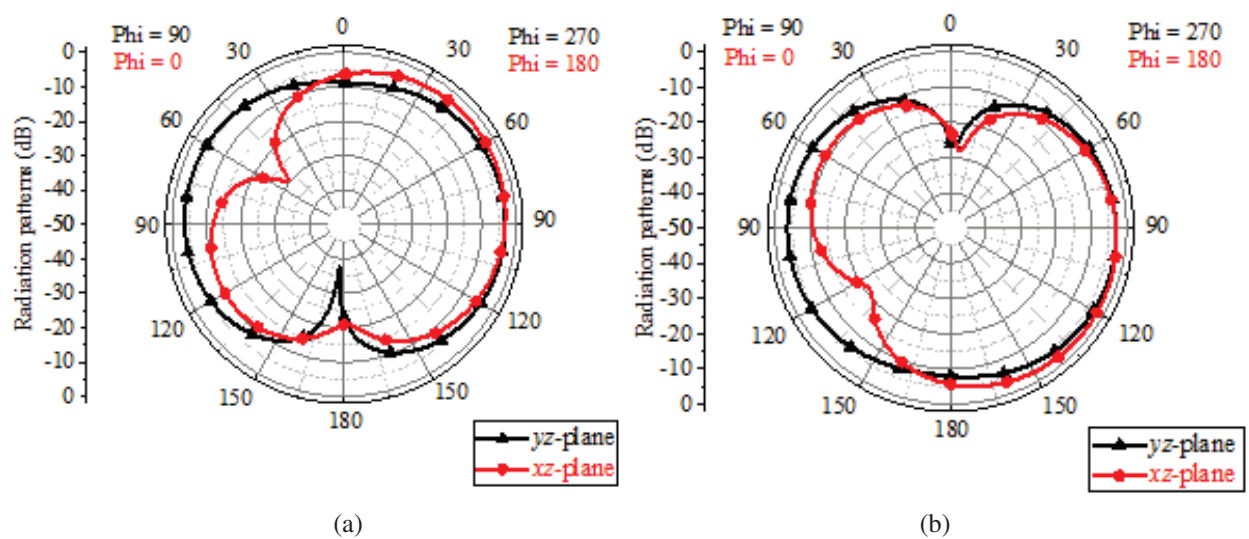


Fig. 5. Radiation patterns of the proposed CPPMA at 2.45 GHz: (a) LHCP and (b) RHCP.



Fig. 6. Fabricated prototype of the proposed CPPMA: (a) front view and (b) back view.



Fig. 7. Reflection coefficient setup measurement of the proposed CPPMA.

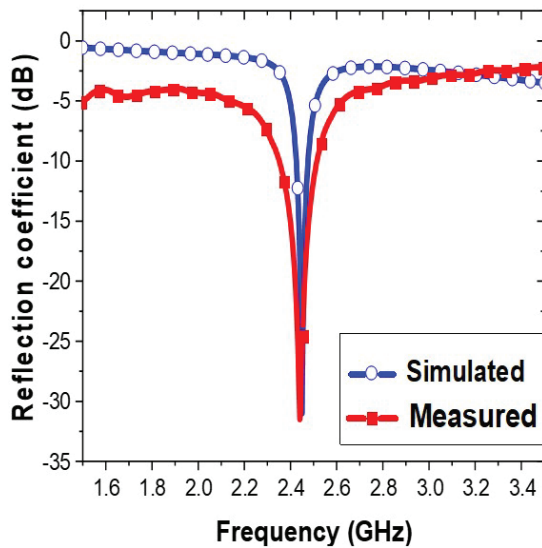


Fig. 8. Simulated and measured reflection coefficient of the proposed CPPMA.

B. Human body phantom models

Various breast, head and arm phantoms have been proposed in the literature. Because various tissues have different electrical properties and absorb different quantities of microwaves, changes in the frequency spectrum have a large influence on the dielectric characteristics of biological tissues [20, 21].

The dielectric properties are reconstructed in quantitative microwave imaging based on the difference in the complex permittivity. Due to the complexity of the structure and composition of biological tissues, Gabriel, et al. [22, 23] used the 4-Cole-Cole model which exhibits a parametric description of four types of dispersion in biological tissue. This model describes the frequency-dependent permittivity and conductivity of several biological tissues in the frequency range from Hz to GHz, which is defined as:

$$\begin{aligned} \varepsilon(\omega) &= \varepsilon'(\omega) + j\varepsilon''(\omega) \\ &= \sum_{n=1}^4 \varepsilon_{\infty} + \frac{\Delta \varepsilon_n}{1 + (j\omega\tau_n)^{1-\alpha_n}} + \frac{\sigma_i}{j\omega\varepsilon_0}, \quad (1) \end{aligned}$$

where the ability to absorb microwave energy is indicated by the loss factor, whereas the ability to store microwave energy is indicated by the real part. The magnitude of the dispersion is described as $\Delta \varepsilon_n = \varepsilon_s - \varepsilon_{\infty}$, ε_{∞} is the permittivity at high frequency, ε_s is the static permittivity, ω is the angular frequency (rad/s), τ is the relaxation time constant (s), σ_i is the static ionic conductivity (S/m), α is a distribution parameter and ε_0 is the permittivity of free space.

The basic principle of the use of microwaves in breast imaging for detecting malignant cells is based on the significant divergence between the dielectric properties of pathological tissues and healthy tissues. In the

breast cancer detection, a mono-static radar imaging system uses one antenna that acts as a transceiver to detect and locate the tumor in the breast with an easier and clearer manner. The antenna transmits microwave pulses toward the breast to scan several locations inside the breast phantom.

The antenna then receives signals from the breast in terms of reflected or scattered signals. It is used to highlight that the changes in the back-scattered signal divulge disparities in the electrical properties of tissues. Thus, the back-scattered signal can be used to find out tumor cells in the breast, which exhibit higher dielectric constants than normal breast tissues [24, 25].

B.1. Human breast phantom model

A hemispherical shaped breast model has been simulated in the present paper. It is composed of 3 layers i.e. skin, fat and fibro-glandular as depicted in Fig. 9. The properties of human breast phantom model [22, 26] and of the tumor model [27, 28] are given in the Table 2.

Table 2: Parameters of the 3-layer human breast phantom model and tumor model at 2.45 GHz

Tissues	ϵ (F/m)	σ (S/m)	ρ (kg/ m^3)	R (mm)
Skin	38.0067	1.46407	1100	50
Fat	5.14667	0.137039	900	48
Fibro-Glandular	20.1	0.5	1040	38
Tumor	55.2566	2.7015	1050	/

ϵ = permittivity, σ = electrical conductance, ρ = density, R = radius

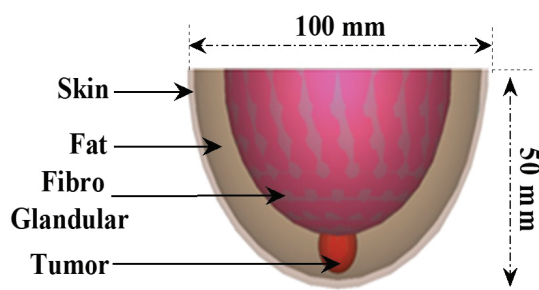


Fig. 9. Hemispherical human breast phantom model.

B.2. Human head phantom model

A spherical-shaped head model was considered in this paper. As depicted in Fig. 10, it is composed of 7 layers, i.e. skin (dry), fat, muscle, skull, dura, cerebrospinal fluid and brain. The properties of the considered human head phantom model and of the stroke model (blood clot) are given in Table 3.

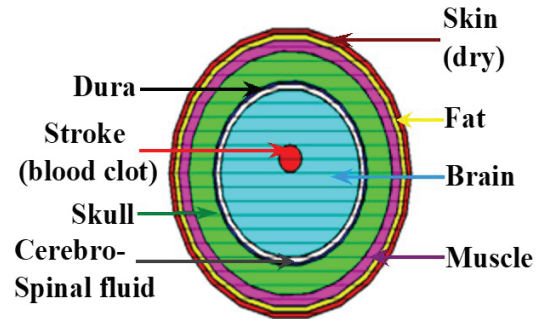


Fig. 10. Spherical human head phantom model.

Table 3: Parameters of the 7-layer human head phantom model and brain stroke model (blood clot) at 2.45 GHz [22, 29]

Tissues	ϵ (F/m)	σ (S/m)	ρ (kg/ m^3)	R (mm)
Skin	38.0067	1.46407	1100	50
Fat	5.14667	0.137039	900	48
Muscle	53.573540	1.810395	1040.0	46
Skull	14.965101	0.599694	1850.0	42
Dura	42.035004	1.668706	1130	32
Cerebro-spinal Fluid	66.243279	3.457850	1006	31
Brain	42.538925	1.511336	1030.0	29
Stroke (Blood Clot)	58.263756	2.544997	/	/

B.3. Human arm phantom model

A portion of a human arm phantom model has been designed. It is composed of 4 layers, i.e. skin, fat, muscle and bone, as depicted in Fig. 11. The properties of

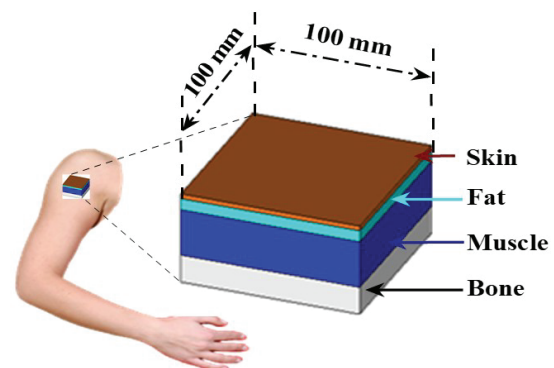


Fig. 11. Portion of a human arm phantom model.

the considered human arm phantom model are given in Table 4 [30].

Table 4: Parameters of the 4-layer human arm phantom model at 2.45 GHz [30]

Tissues	ϵ (F/m)	σ (S/m)	ρ (kg/m ³)	T (mm)
Skin	37.95	1.49	1001	2
Fat	5.27	0.11	900	5
Muscle	52.67	1.77	1006	20
Bone	18.49	0.82	1008	13

T = thickness

III. SIMULATION AND RESULTS

A. Breast cancer detection

The effect of radiation on the human breast model is examined in this section. First, the proposed CPPMA was positioned at a safe distance of 10 mm from a healthy human breast phantom model as depicted in Fig. 12 (a). Then, a spherical tumor of radius 2.5 mm was inserted at four different positions inside the healthy human breast phantom as depicted in Fig. 12 (b). The reflection coefficient of the designed CPPMA with the human breast model having a tumor (R = 2.5 mm) at four different positions (0, 0, 15), (20, 15, 30), (0, 0, 40), (30, -30, 50) and without the tumor, is shown in Fig. 13. It is clear that the shifting level of the resonant frequency is inversely proportional to the distance between the CPPMA and the tumor.

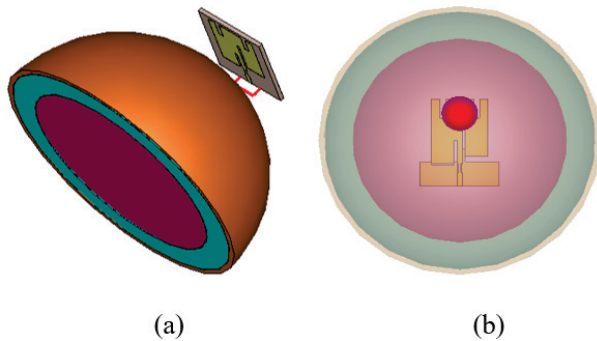


Fig. 12. CPPMA placed at a distance of 10 mm from the human breast phantom model: (a) without tumor and (b) with tumor.

Then, three different sizes (R = 4 mm, 7 mm and 9 mm) of tumors were placed at a fixed position inside the healthy human breast phantom as depicted in Fig. 12 (b). The reflection coefficient of the set CPPMA and human breast model with and without a tumor is presented in Fig. 14. It reveals that the shift in the resonance

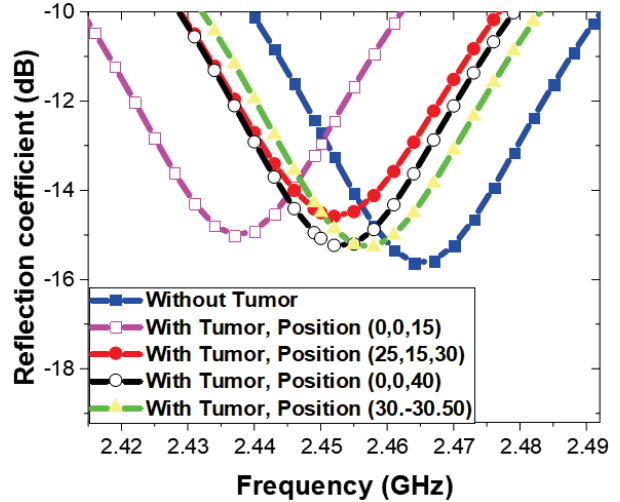


Fig. 13. Simulated reflection coefficient for human breast phantom model in the presence of a tumor of radius = 2.5 mm at 4 different positions.

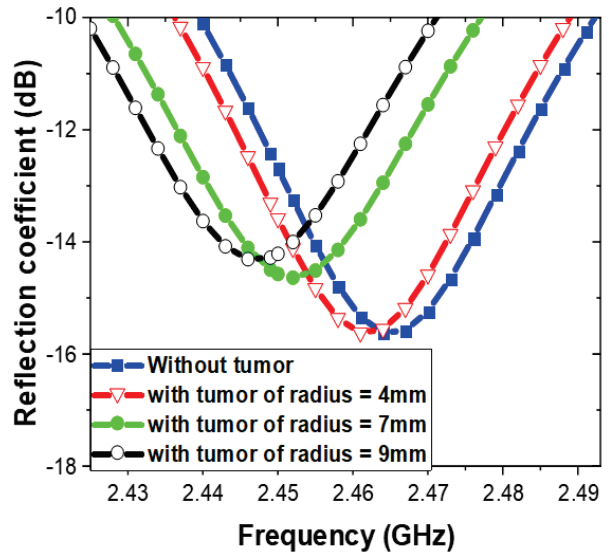


Fig. 14. Simulated reflection coefficient for detecting three different sizes of breast tumor at the same location.

frequency and in the adaptation level is more noticeable for large tumor sizes. Thus, as the tumor size increases, its detection becomes easier.

B. Brain stroke detection

In this section, the effect of radiation on the human head model is discussed. First, the designed CPPMA was positioned at a safe distance of 5 mm from the healthy human head phantom model as depicted in Fig. 15 (a). Then, a brain stroke (blood clot) of two different radiuses 5 and 13 mm, with the dielectric properties depicted in Table 3, was placed inside the healthy brain as depicted

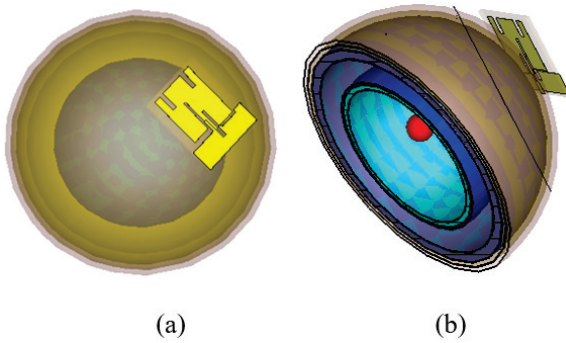
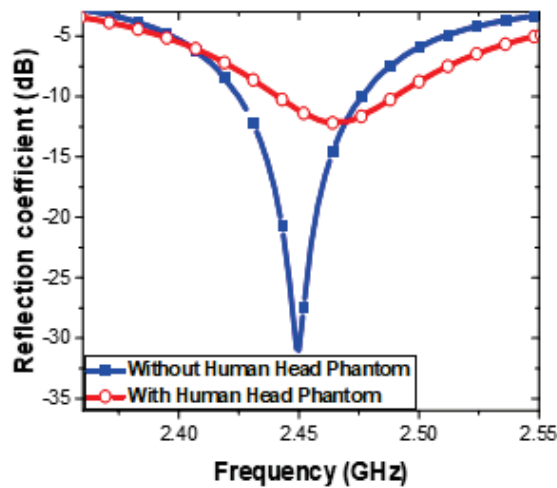
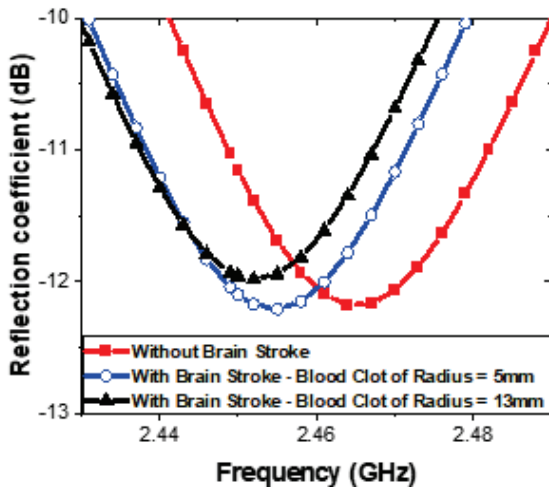


Fig. 15. CPPMA positioned at a distance of 5 mm from the human head phantom model: (a) without brain stroke, and (b) with brain stroke (blood clot).



(a)



(b)

Fig. 16. (a) Simulated reflection coefficient with and without human head phantom model, (b) simulated reflection coefficient for detecting two different sizes of stroke (blood clot).

in Fig. 15 (b). The reflection coefficient of the set CPPMA and human head model with and without stroke (blood clot) is shown in Fig. 16. A shift in the resonance frequency of the CPPMA in the cases of normal and brain stroke is clear. The reflected wave increases with the increase in the size of the blood clots which agree with expectation.

Figures 17–19 show the simulated E-field, H-field and current density of the set CPPMA and human head model with and without stroke at 2.45 GHz. Table 5 indicates that the current density, E-field and H-field values decrease in the presence of brain stroke which predict its existence in the human head.

Table 5: Comparison of the simulated results with and without brain stroke model at 2.45 GHz

	Without Brain Stroke	With Brain Stroke R = 5 mm	With Brain Stroke R = 13 mm
Resonance Frequency (GHz)	2.464	2.455	2.452
Reflection Coefficient (dB)	-12.142075	-12.207286	-11.97995
Current Density A/m ²	683.562	639.836	636.324
E Field V/m	71078.5	59542.3	62530
H Field A/m	770.724	545.151	505.475

The linearly-polarized antenna shown in Fig. 2 (b) has been simulated without and with a brain stroke model (R = 5 mm and 13 mm) to show the advantages of the circular polarization for the detection of the brain stroke. Slight adjustments have been introduced in the dimensions of the antenna to shift the resonant frequency to 2.45 GHz.

The reflection coefficient of the simulated linearly polarized printed monopole antenna (LPPMA) is presented in Fig. 20. The reflection coefficient of the set LPPMA and human head model with and without the stroke model is shown in Fig. 22.

It reveals that there is no shift in the resonance frequency compared to the results obtained with the proposed CPPMA (Fig. 16 (b)). Table 6 indicates that the CPPMA is more effective than the LPPMA in detecting brain stroke because the circularly polarized waves penetrate the body more deeply.

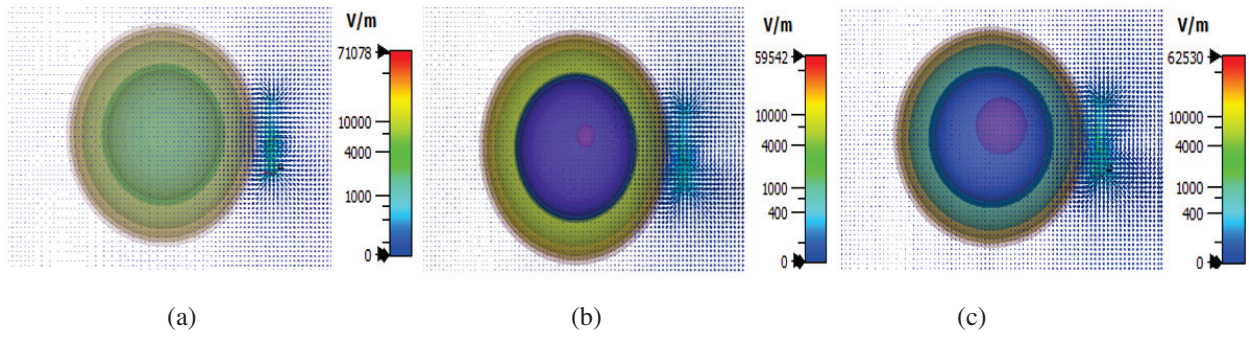


Fig. 17. Electric field: (a) without brain stroke, (b) with stroke R = 5mm, and (c) with stroke R = 13mm.

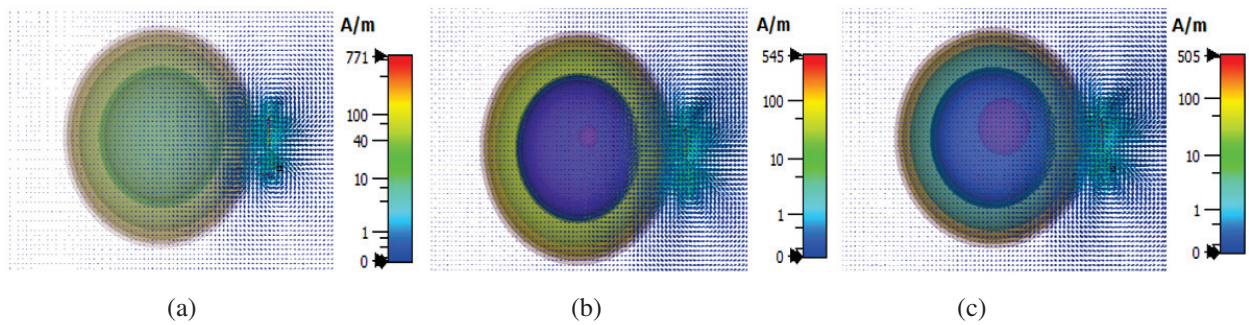


Fig. 18. Magnetic field: (a) without brain stroke, (b) with stroke R = 5mm, and (c) with stroke R = 13mm.

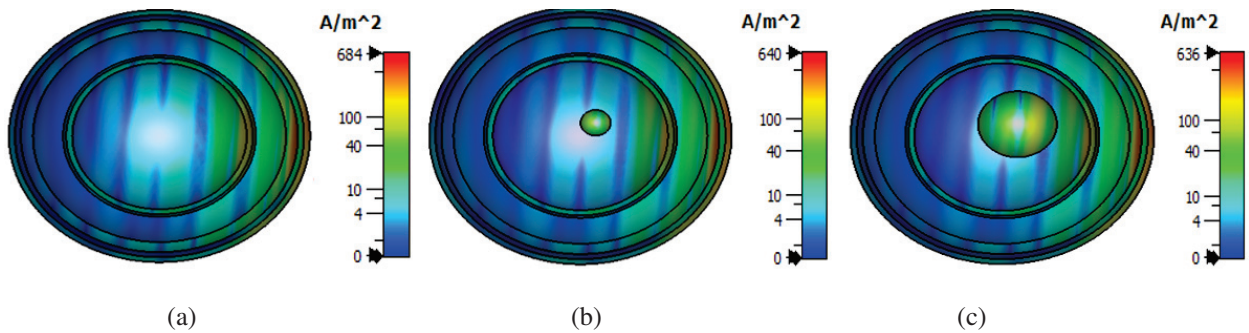


Fig. 19. Current density: (a) without brain stroke, (b) with stroke R = 5mm, and (c) with stroke R = 13mm.

Table 6: Comparison of the simulated results of the two antennas CPPMA and LPPMA with and without brain stroke model

		Without Brain Stroke	With Brain Stroke R = 5 mm	With Brain Stroke R = 13 mm
CPPMA	Resonance Frequency (GHz)	2.464	2.455	2.452
	Reflection Coefficient (dB)	-12.14207	-12.207286	-11.97995
LPPMA	Resonance Frequency (GHz)	2.467	2.467	2.467
	Reflection Coefficient (dB)	-13.50134	-13.485089	-13.45988

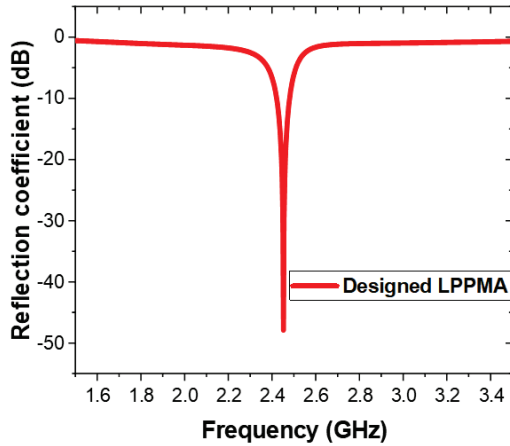


Fig. 20. Reflection coefficient of the designed LPPMA.

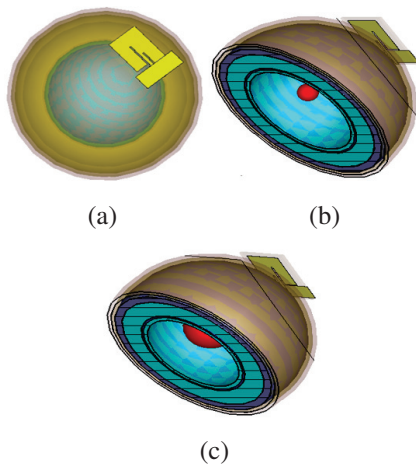


Fig. 21. LPPMA placed at a distance of 5 mm from the human head phantom model: (a) without brain stroke, (b) with brain stroke $R = 5$ mm, and (c) with brain stroke $R = 13$ mm.

IV. WEARABLE APPLICATION

In this section, the CPPMA performance has been simulated on a human arm phantom model and on a human arm to check its usefulness for health monitoring and wearable application. First, the designed CPPMA was positioned at a safe distance of 10 mm from a human arm phantom model as depicted in Fig. 23 (a). Figure 23 (b) indicates that the resonant frequency of the CPPMA positioned on a human arm phantom model has a small shifting compared to the antenna without a human arm phantom due to the high dielectric properties of body tissues. Nonetheless, the designed CPPMA in the presence of a human arm phantom has an impedance bandwidth extending from 2.438 GHz to 2.489 GHz with a reflection coefficient level of -13.28 dB which covers the desired ISM band.

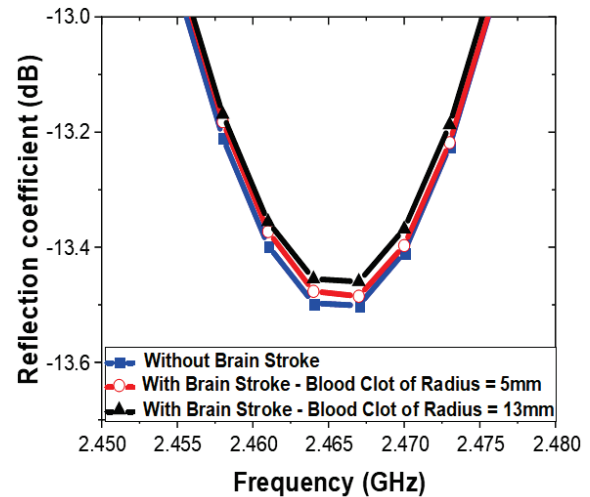


Fig. 22. Simulated reflection coefficient of the LPPMA for detecting two different sizes of brain stroke model.

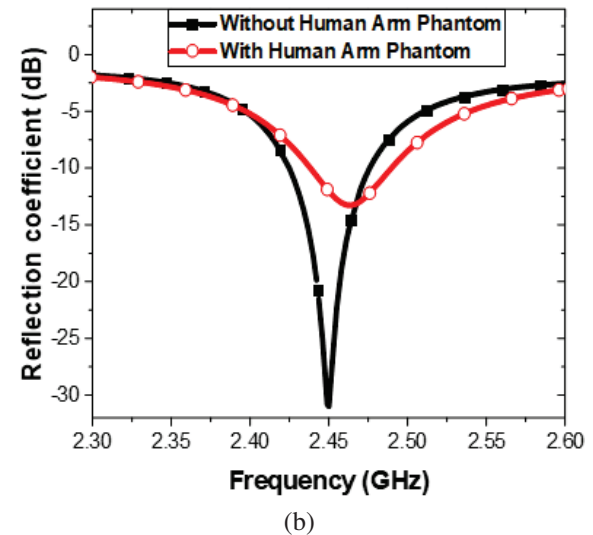
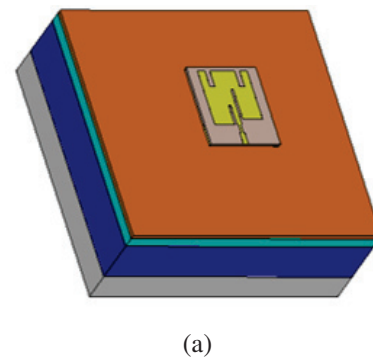


Fig. 23. (a) CPPMA placed at a distance of 10 mm from the portion of a human arm phantom model and (b) simulated reflection coefficient with and without human arm phantom.

The usefulness of the proposed CPPMA for wearable health-monitoring applications was checked experimentally by placing the fabricated prototype on a human arm as shown in Fig. 24. The simulated and measured reflection coefficient results of the proposed CPPMA placed on a human arm are compared in Fig. 25.

The volume of the human arm, the gap between the CPPMA and the human arm, and SMA losses were the causes of the mismatch between the on-arm simulated and measured values. We conclude from the results that

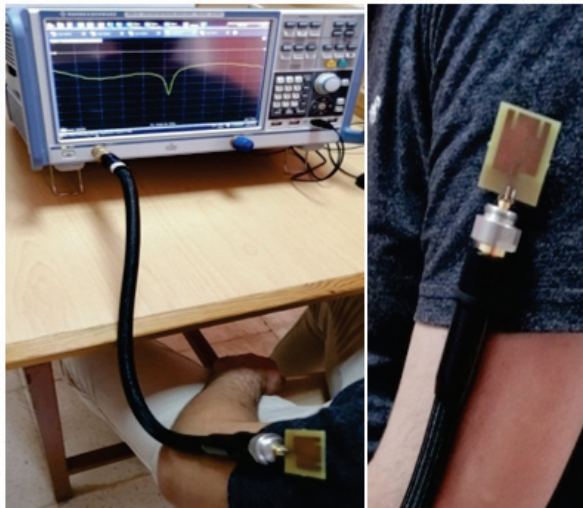


Fig. 24. Reflection coefficient measurement of the fabricated prototype on a human arm.

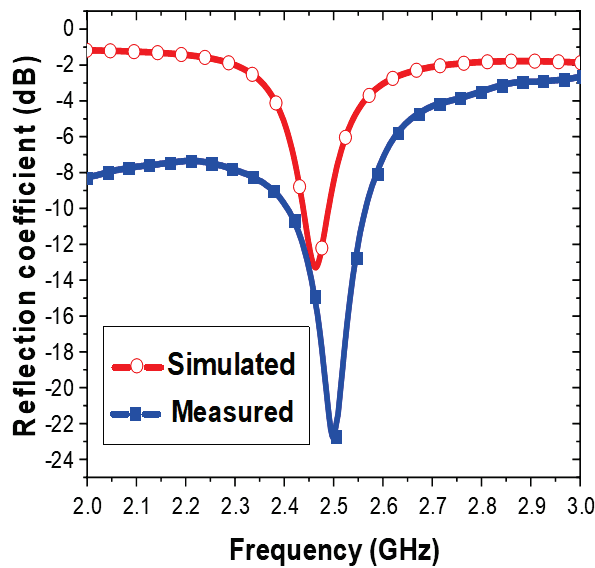


Fig. 25. Reflection coefficient of the proposed CPPMA on a human arm.

the proposed CPPMA is suitable for wearable health-monitoring applications.

V. SPECIFIC ABSORPTION RATE (SAR) CALCULATIONS

SAR describes how much power is absorbed per kilogram of human body tissue. Hence, its unit is Watts per Kilogram (W/Kg). Typically the SAR is averaged across a small volume (1 g or 10 g) of tissue. Its value is calculated using the following equation [31]:

$$SAR = \frac{\sigma}{\rho} |E|^2 = \frac{J^2}{\rho\sigma}, \quad (2)$$

where, E is the electric field intensity in V/m, J is the current density in A/m, σ is the electric conductivity of the tissue in S/m, and ρ is mass density of the tissue in Kg/m³.

In this section, the SAR parameter of the proposed CPPMA was analyzed on the breast, head and arm of the human body phantom.

The SAR values refer to power averaged over 10 g of tissue. In order to satisfy the most restrictive SAR regulation (i.e. SAR_{10g} < 2 W/kg), the input powers must be limited according to Table 7.

Table 7: Input power limits that give acceptable SAR_{10g} values at 2.45 GHz

	Distance (mm)	Input Power (mW)	SAR _{10g} (W/Kg)
Breast	10	110	1.84
Head	5	68	1.9
Arm	10	170	1.92

The simulated SAR_{10g} on the breast, head and portion of a human arm is shown in Fig. 26.

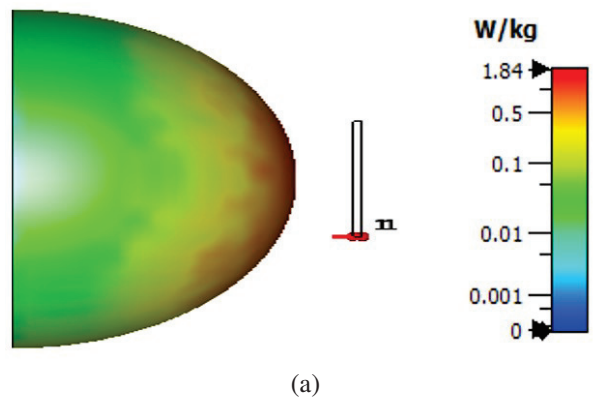


Fig. 26. Continued.

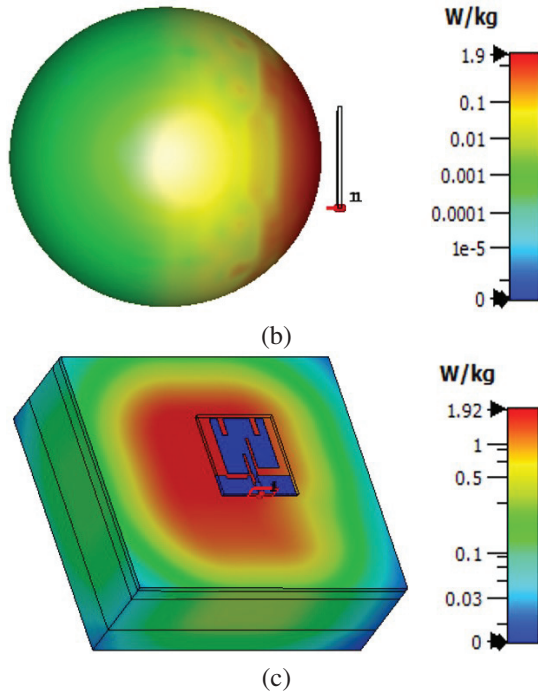


Fig. 26. Simulated specific absorption rate (SAR_{10g}) at 2.45 GHz: (a) breast, (b) head, and (c) portion of a human arm phantom model.

VI. CONCLUSIONS

This paper presented a mono-static narrow band CPPMA for medical microwave imaging and health monitoring applications. A prototype of the designed CPPMA of size $34 \times 28 \times 1.5 \text{ mm}^3$ has been fabricated and printed on the low-cost FR-4 substrate. The measured results indicate that the fabricated prototype operates in a narrow bandwidth of 195 MHz (2.32 - 2.515 GHz). Moreover, the designed CPPMA exhibits a circular polarization in the range of 2.4386 - 2.4633 GHz. The capability of the detection of breast tumor and brain stroke for the proposed CPPMA was validated using different phantom models.

Furthermore, the practicality of the proposed CPPMA for wearable health-monitoring applications was confirmed experimentally. The overall obtained results confirm the effectiveness and usefulness of the proposed CPPMA for several biomedical applications.

ACKNOWLEDGMENT

This work is supported by the Ministry of Higher Education and Scientific Research of Algeria, as part of a research project (PRFU N^o, A25N01UN240120220002).

Table 8: Comparison of the proposed CPPMA with several recently reported antennas

Ref.	Application	Technique Used for Pathological Tissue Detection	Substrate and Dimensions (mm^3)	Circular Polar	Frequency Band (GHz)	SAR Evaluation
[32]	Body-centric communications	-	RO4003 $42 \times 30 \times 0.813$	No	2.4 - 12	Not reported
[33]	Breast tumor detection	Scattering imaging	Air-gap $40 \times 25 \times 10.5$	No	1.67 - 1.74	Not reported
[34]	Breast tumor detection	Resonance frequency shift	RO4003C $40 \times 40 \times 1.54$	No	0.49 - 0.56	Not reported
[35]	Wireless body area network	-	RT-Duroid 5880 $34.4 \times 34.4 \times 4$	Yes	5.27 - 6.37	SAR evaluated on human body
[36]	Head imaging	Scattering parameters and near field directivity	RO4350B $50 \times 44 \times 1.524$	No	1.70 - 3.71	SAR evaluated on head
[37]	Wireless body area network	-	Denim $50 \times 44 \times 0.7$	No	2.27 - 3.42	SAR evaluated on human body arm
This work	Tumor detection, brain stroke detection and remote health monitoring	Resonance frequency shift, current density, E-Field and H-Field distribution	FR-4 $34 \times 28 \times 1.5$	Yes	2.425 - 2.475	SAR evaluated on breast, head and human body arm

REFERENCES

- [1] K. Lalitha and J. Manjula, "Non-invasive microwave head imaging to detect tumors and to estimate their size and location," *Phys. Med.*, vol. 13, pp. 100047, 2022.
- [2] M. A. Aldhaeabi, K. Alzoubi, T. S. Almoneef, S. M. Bamatraf, H. Attia, and O. M. Ramahi, "Review of microwaves techniques for breast cancer detection," *Sensors*, vol. 20, no. 8, pp. 2390, 2020.
- [3] G. Kaur and A. Kaur, "Monostatic radar-based microwave imaging of breast tumor detection using a compact cubical dielectric resonator antenna," *Microw. Opt. Technol. Lett.*, vol. 63, no. 1, pp. 196-204, 2021.
- [4] W. He, Y. He, S. W. Wong, and C. H. Liao, "A wide-band circularly polarized S-shaped slot antenna," *Int. J. RF Microw. Comput.-Aided Eng.*, vol. 31, no. 5, pp. e22612, 2021.
- [5] N. Sharma, A. Kumar, A. De, and R. K. Jain, "Design of compact hexagonal shaped multiband antenna for wearable and tumor detection applications," *Prog. Electromagn. Res. M*, vol. 105, pp. 205-217, 2021.
- [6] R. Alageea and A. Assalem, "Brain cancer detection using U-shaped slot vivaldi antenna and confocal radar based microwave imaging algorithm," *Am. Sci. Res. J. Eng. Technol. Sci.*, vol. 66, no. 1, pp. 1-13, 2020.
- [7] M. Samsuzzaman, K. A. Fakeeh, M. S. Talukder, M. M. Hasan, M. H. Rahman, M. M. Alam, M. S. Shaik, and M. T. Islam, "A double hollow rectangular-shaped patch and with the slotted ground plane monopole wideband antenna for microwave head imaging applications," *Int. J. Commun. Syst.*, vol. 34, no. 16, pp. e4958, 2021.
- [8] N. Niranjankumar, B. S. Srikanth, S. B. Gurung, S. Manu, G. N. S. Gowthami, T. Ali, and S. Pathan, "A slotted UWB monopole antenna with truncated ground plane for breast cancer detection," *Alex. Eng. J.*, vol. 59, no. 5, pp. 3767-3780, 2020.
- [9] A. B. Dey, S. S. Pattanayak, D. Mitra, and W. Arif, "Investigation and design of enhanced decoupled UWB MIMO antenna for wearable applications," *Microw. Opt. Technol. Lett.*, vol. 63, no. 3, pp. 845-861, Mar. 2021.
- [10] U. R. Khan, J. A. Sheikh, S. Bashir, and S. Ahmed, "Metamaterial inspired wideband on-body antenna design for bio-medical applications," *Mater. Today: Proc.*, vol. 80, no. 3, pp. 1772-1776, 2023.
- [11] H. Singh, K. Srivastava, S. Kumar, and B. K. Kanaujia, "A planar dual-band antenna for ISM/wearable applications," *Wirel. Pers. Commun.*, vol. 118, no. 1, pp. 631-646, 2021.
- [12] Y. K. Ho, T. E. M. Foong, H. Takefumi, L. K. Chun, and H. Kazuhiro, "A multi-band planar antenna for biomedical applications," *Frequenz*, vol. 75, no. 5-6, pp. 221-228, 2021.
- [13] S. Roy and U. Chakraborty, "Metamaterial based dual wideband wearable antenna for wireless applications," *Wirel. Pers. Commun.*, vol. 106, no. 3, pp. 1117-1133, June 2019.
- [14] K. Zhang, P. J. Soh, and S. Yan, "Design of a compact dual-band textile antenna based on metasurface," *IEEE Trans. Biomed. Circuits Syst.*, vol. 16, no. 2, pp. 211-221, Apr. 2022.
- [15] X. Lin, Y. Chen, Z. Gong, B. C. Seet, L. Huang, and Y. Lu, "Ultrawide band textile antenna for wearable microwave medical imaging applications," *IEEE Trans. Antennas Propag.*, vol. 68, no. 6, pp. 4238-4249, June 2020.
- [16] K. Zhang, G. A. E. Vandenbosch, and S. Yan, "A novel design approach for compact wearable antennas based on metasurfaces," *IEEE Trans. Biomed. Circuits Syst.*, vol. 14, no. 4, pp. 918-927, Aug. 2020.
- [17] O. Fiser, V. Hruby, J. Vrba, T. Drizdal, J. Tesarik, and D. Vrba, "UWB bowtie antenna for medical microwave imaging applications," *IEEE Trans. Antennas Propag.*, vol. 70, no. 7, pp. 5357-5372, July 2022.
- [18] A. Chaabane and M. Guerroui, "Circularly polarized ultra wideband antenna with question mark-shaped patch for ground penetrating radar applications," *J. Appl. Res. Technol.*, vol. 20, no. 3, pp. 274-283, June 2022.
- [19] A. Chaabane, M. Guerroui, and D. Aissaoui, "Circularly polarized quasi-rectangular patch UWB antenna for GPR applications," *Serb. J. Electr. Eng.*, vol. 19, no. 3, pp. 261-271, Oct. 2022.
- [20] S. Gabriel, R. W. Lau, and C. Gabriel, "The dielectric properties of biological tissues: II. Measurement in the frequency range 10 GHz to 20 GHz," *Phys. Med. Biol.*, vol. 41, no. 11, pp. 2251-2269, 1996.
- [21] L. Farrugia, P. S. Wismayer, L. Z. Mangion, and C. V. Sammut, "Accurate in-vivo dielectric properties of liver from 500 MHz to 40 GHz and their correlation to ex-vivo measurements," *Electromagn. Biol. Med.*, vol. 35, no. 4, pp. 365-373, 2016.
- [22] C. Gabriel, "Compilation of the dielectric properties of body tissues at RF and microwave frequencies," *U.S. Air Force Report AFOSR-*

- TR-96. Available at: <https://www.fcc.gov/general/body-tissue-dielectric-parameters>, 1996.
- [23] N. De Geeter, G. Crevecoeur, L. Dupré, W. V. Hecke, and A. Leemans, "A DTI-based model for TMS using the independent impedance method with frequency-dependent tissue parameters," *Phys. Med. Biol.*, vol. 57, no. 8, pp. 2169-2188, 2012.
- [24] I. R. Sheeba and T. Jayanthi, "Design and analysis of a flexible softwear antenna for tumor detection in skin and breast model," *Wireless Pers. Commun.*, vol. 107, no. 2, pp. 887-905, 2019.
- [25] R. Singh, N. Narang, D. Singh, and M. Gupta, "Compact wideband microstrip patch antenna design for breast cancer detection," *Def. Sci. J.*, vol. 71, no. 3, pp. 352-358, May 2021.
- [26] Z. Katbay, S. Sadek, R. Lababidi, A. Perennec, and M. le Roy, "Miniature antenna for breast tumor detection," *IEEE NEWCAS 13th International New Circuits and Systems Conference*, Grenoble, France, pp. 1-4, 2015.
- [27] R. Ortega-Palacios, L. Leija, A. Vera, and M. F. J. Cepeda, "Measurement of breast-tumor phantom dielectric properties for microwave breast cancer treatment evaluation," *IEEE 7th International Conference on Electrical Engineering Computing Science and Automatic Control.*, Tuxtla Gutierrez, Mexico, pp. 216-219, 2010.
- [28] M. Palandoken, C. Murat, A. Kaya, and B. Zhang, "A novel 3-D printed microwave probe for ISM band ablation systems of breast cancer treatment applications," *IEEE Trans. Microw. Theory Tech.*, vol. 70, no. 3, pp. 1943-1953, Mar. 2022.
- [29] M. A. Rahman, M. F. Hossain, M. A. Riheen, and P. K. Sekhar, "Early brain stroke detection using flexible monopole antenna," *Prog. Electromagn. Res. C*, vol. 99, pp. 99-110, 2020.
- [30] S. Kiani, P. Rezaei, and M. Fakhr, "A CPW-fed wearable antenna at ISM band for biomedical and WBAN applications," *Wirel. Netw.*, vol. 27, no. 1, pp. 735-745, 2021.
- [31] M. K. Hosain, A. Z. Kouzani, S. J. Tye, O. A. Abulseoud, A. Amiet, A. Galehdar, and M. Berk, "Development of a compact rectenna for wireless powering of a head-mountable deep brain stimulation device," *IEEE J. Transl. Eng. Health Med.*, vol. 2, pp. 1-13, 2014.
- [32] A. Darvazehban and T. Rezaee, "Ultra-wideband microstrip antenna for body centric communications," *Applied Computational Electromagnetics Society (ACES) Journal*, vol. 33, no. 3, pp. 355-358, Mar. 2018.
- [33] M. A. Ullah, T. Alam, M. S. Alam, S. Kibria, and M. T. Islam, "A unidirectional 3D antenna for biomedical microwave imaging based detection of abnormality in human body," *Microsyst. Technol.*, vol. 24, no. 12, pp. 4991-4996, 2018.
- [34] M. A. Aldhaeabi, T. S. Almonee, H. Attia, and O. M. Ramahi, "Electrically small magnetic probe with PCA for near-field microwave breast tumors detection," *Prog. Electromagn. Res. M*, vol. 84, pp. 177-186, 2019.
- [35] Y. B. Chaouche, M. Nedil, I. B. Mabrouk, and O. M. Ramahi, "A wearable circularly polarized antenna backed by AMC reflector for WBAN communications," *IEEE Access*, vol. 10, pp. 12838-12851, 2022.
- [36] A. Hossain, M. T. Islam, M. E. Chowdhury, and M. Samsuzzaman, "A grounded coplanar waveguide-based slotted inverted delta-shaped wideband antenna for microwave head imaging," *IEEE Access*, vol. 8, pp. 185698-185724, 2020.
- [37] D. Gopi, P. V. Kokilagadda, S. Gupta, and V. R. K. R. Dodda, "Asymmetric coplanar strip-fed textile-based wearable antenna for MBAN and ISM band applications," *Int. J. Numer. Model. Electron. Netw. Devices Fields*, vol. 34, no. 6, pp. e2920, 2021.



Bilal Guetaf is currently a Ph.D. Student at the University 8 Mai 1945 Guelma, Algeria. He is a member of the Telecommunications Laboratory, University 8 Mai 1945 Guelma. His main research interests include: antennas for medical microwave imaging, wearable antennas, implantable antennas, and biomedical engineering.



Abdelhalim Chaabane received a Ph.D. degree and completed his habilitation in electronics in 2017 and 2020, respectively. He is currently an associate professor and the Director of the Telecommunications Laboratory at the University 8 Mai 1945 Guelma, Algeria. His current research areas of interest include: fractal antennas, MIMO antenna systems, reconfigurable antennas, millimeter-wave high-gain and wide-band antennas, UWB applications and radar, and biomedical engineering.



Abderrezak Khalfallaoui received a Ph.D. degree in Electronics from the University of Littoral Côte d'Opale, France, in 2010 at the Laboratory of Materials and Components for Electronics (LEMCEL). In 2011, he joined the Telecommunications Laboratory at the University

8 Mai 1945 Guelma, Algeria where he is an Assistant Professor. His research interests are design and processing of radio-frequency integrated circuits, tunable ferroelectric devices, and their applications in microwaves. Since 2020, his research has been on antennas, multi-band antennas, and ground-penetrating radar antennas.



Hussein Attia received a Ph.D. in Electrical and Computer Engineering from the University of Waterloo, Ontario, Canada, in 2011. He worked as a Research Engineer with the Coding and Signal Transmission Laboratory at the University of Waterloo from March 2011 to July

2013. He was granted a Postdoctoral Fellowship at Concordia University, Montreal, Canada, from August 2014 to July 2015. He was also a Visiting Scholar at the University of Quebec (INRS), from August 2015 to December 2015 and from June 2017 to August 2017. He is currently an Associate Professor and the Director of the Applied Electromagnetics Laboratory at King Fahd University of Petroleum and Minerals (KFUPM). He is currently an Associate Editor for IEEE Antennas and Wireless Propagation Letters and IEEE ACCESS. He has published about 100 journal and conference papers. His research interests include biomedical engineering, microwave sensors, millimeter-wave antennas, analytical techniques for electromagnetic modeling, and metamaterials. Dr. Attia has received several awards, including a full Ph.D. scholarship from the Ministry of Higher Education, Egypt (2007-2011), the University of Waterloo Graduate Scholarship for excellence in research and coursework in 2009, and a certificate in University Teaching from the University of Waterloo in 2010. He was a finalist in the Best Paper Competition of the 2011 IEEE AP-S International Symposium on Antennas and Propagation. In 1999 he was ranked first among all B.Sc. electronics and communication engineering students at Zagazig University, Egypt.

Low-profile Circularly Polarized Conformal Antenna Array with Side Lobe Suppression for Vehicular SATCOM Applications

Ebenezer Abishek¹, Ramesh Subramaniam², Parthasarathy Ramanujam³, and Manikandan Esakkimuthu⁴

¹Department of Electronics and Communication Engineering
Vel Tech Multi Tech Dr.Rangarajan Dr.Sakunthala Engineering College, Chennai, 600062, India
ebenezerabishek@gmail.com

²Department of Electronics and Communication Engineering
SRM Valliammai Engineering College, Chennai, 603203, India

³Department of Electronics and Communication Engineering
National Institute of Technology, Tiruchirappalli, 620015, India

⁴Centre for Innovation and Product Development
Vellore Institute of Technology, Chennai, 600127, India

Abstract – A circularly polarized microstrip antenna array with low side lobe levels is proposed for Vehicular Satellite Communication. The suppression of side lobe levels is accomplished by the non-uniform power distribution utilized to feed the individual patch elements. Impedance matching is ensured by the incorporation of a quarter-wave transformer via a microstrip line fed to the edge of the patch. When the proposed amplitude-weighted feed is compared to the conventional corporate feed, simulation results indicate a reduction in side lobe levels of 8.9 dB. The proposed antenna is constructed out of RT/DUROID 5880 material, which is lighter, more flexible, and less expensive than ceramic materials. The radiation characteristics of the proposed antenna are compared when the antenna is planar versus when it is made to conform to the roof of the vehicle. The measured results indicate a reflection coefficient at the resonant frequency of -31.5 dB and -27.7 dB when conformal, an impedance bandwidth of 410 MHz and 180 MHz when conformal, an axial ratio bandwidth of 140 MHz and 170 MHz when conformal, and a peak gain of 15.719 dB and 14.335 dB when conformal. The measured results validate the simulation results that this proposed antenna is appropriate for a variety of Vehicular Satellite Communication applications.

Index Terms – amplitude tapering ratio, circular polarization, microstrip array, side lobe level, vehicular satellite communication.

I. INTRODUCTION

The vehicle-based SATCOM technology is known as Vehicular Satellite Communication. Satellites are utilized to establish and maintain communication between moving vehicles and immobile infrastructures such as hospitals, police stations, etc. Compared to vehicle-to-vehicle communication, the satellite provides a larger coverage area in vehicular satellite communication [1]. Important issues that must be addressed in Vehicular Satellite Communication include interference with nearby satellites [2], [3] and the need for increased power to provide high-quality services [4], [5]. Due to their ability to overcome the Faraday rotation that occurs in the ionosphere, circularly polarized antennas are preferred for Vehicular Satellite Communications [6], [7]. The radiation characteristics of a microstrip antenna with a single element can be enhanced by constructing an array of that antenna.

Microstrip technology is used to develop the proposed antenna as a low-profile alternative to conventional SATCOM antennas. IEEE has established Wireless Access in Vehicular Environment as the standard for vehicular networks [8], [9]. This standard is a part of the IEEE 802.11p protocol for mobile ad hoc networks. Vehicular Satellite Communication necessitates the installation of antennas on moving vehicles. More than 50% of earth-orbiting satellites are used for communication [10], [11]. Among these satellites there are satellites used exclusively for Vehicular Satellite Communication to connect moving vehicles and also to

stationary infrastructures [12], [13]. There are numerous civilian applications, including the use of laptops or mobile devices with high-speed internet connectivity in moving vehicles, rapid rescue of passengers in moving vehicles in the event of an accident, tracking of thieves travelling in moving vehicles in the event of a theft, etc. [14]. Vehicular Satellite Communication antennas are also required for military vehicles to maintain communication with the satellite even when traversing difficult terrain [15], [16]. There is a need for low-profile alternatives to high-profile vehicular antennas because a greater number of antennas must be integrated into vehicles as the number of applications increases [17].

Power is a crucial factor for providing high-quality services in moving vehicles. Therefore, it is undesirable for the side lobes to waste energy. Various techniques can be used to suppress side lobes [18]. To address this issue, it is proposed to implement a feed structure that suppresses the side lobes, thereby reducing the battery’s power consumption. This feed structure is incorporated into the proposed planar antenna array alongside circularly polarized patches. The radiation characteristics of this proposed planar antenna array are examined and discussed.

II. ANTENNA DESIGN METHODOLOGY

The antenna proposed was developed in three stages. In the initial phase of the work, a single element microstrip antenna with circular polarization and improved cross polarization isolation is developed. This preliminary phase of the project has been completed and published [19]. A proposed feed structure is designed to suppress the side lobes in the second stage. Using the single element circularly polarized microstrip patch antenna developed in the first stage and the proposed feed structure, a proposed 1*8 element antenna array is constructed. The third stage entails adapting the proposed planar antenna array to the shape of the vehicle’s roof. The antenna’s dimensions are optimized to compensate for changes in the desired performance caused by the conformal placement of the proposed antenna on the roof of the vehicle. The proposed antenna’s radiation characteristics are analyzed using both simulated and measured data.

The proposed feed structure uses unequal T-junction power dividers to distribute power with tapered amplitude. Taylor, Chebyshev, and Binomial arrays are frequently employed amplitude tapered or amplitude weighted arrays, each with their own benefits and drawbacks. Although Binary arrays completely eliminate side lobes, the amplitude coefficients of the array’s individual elements vary greatly. If the Taylor array achieves a radiation pattern with complete suppression of inner side lobes and all side lobes at the same level, directivity will decrease. Chebyshev arrays are also used to obtain opti-

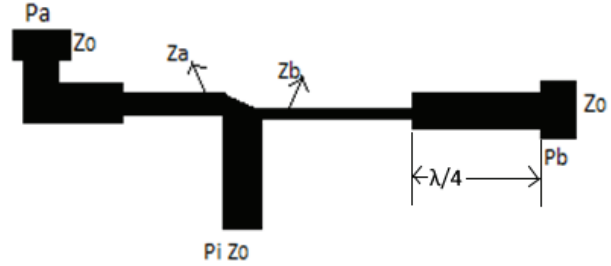


Fig. 1. T-junction unequal power divider.

mal main lobe and suppressed side lobe radiation patterns. The T-junction used for unequal power distribution is shown in Fig. 1.

Assuming lossless transmission, the relation between input and output power of the T-junction power divider for unequal power distribution can be written as

$$P_o = P_a + P_b = P_i, \tag{1}$$

where $P_i = V_o^2/2Z_o,$

$$P_a = V_o^2/2Z_a \text{ and} \tag{2}$$

$$P_b = V_o^2/2Z_b. \tag{3}$$

$$P_a = aP_i. \tag{4}$$

$$P_b = (1 - a)P_i, \tag{5}$$

where a value lies between 0 and 1.

The output port impedances derived from the above equations can be written as

$$Z_a = Z_o/a, \text{ and} \tag{6}$$

$$Z_b = Z_o/(1 - a). \tag{7}$$

Equation (1) describes the simplest case of unequal power division. The impedance is varied at the output ports because of the different widths of the feed at the output ports. The relation between the impedance at ports and the amount of power division is described in equations (2) and (3). Equations (4) to (7) describe the unequal power division and its relation to impedance. Given that port 1 is matched, the formula for calculating the input time average power is $P_i=V_o^2/Z_o,$ where V_o is the junction’s phasor (total) voltage. Since both ports are assumed to be matched, the output powers can be computed similarly and are given in equations (2) and (3). To achieve the desired distribution of incident power between the two output ports, the characteristic impedances of the two transmission lines are modified. The modified values of characteristic impedances are given in equations (6) and (7). The modified characteristic impedances result in unequal power division, and the ratio of unequal power division is given in equations (4) and (5). If output power is known, the impedance of the T-junction output ports can be determined. Using the above equations, the quarter wave transformer transforms impedance in order to perform

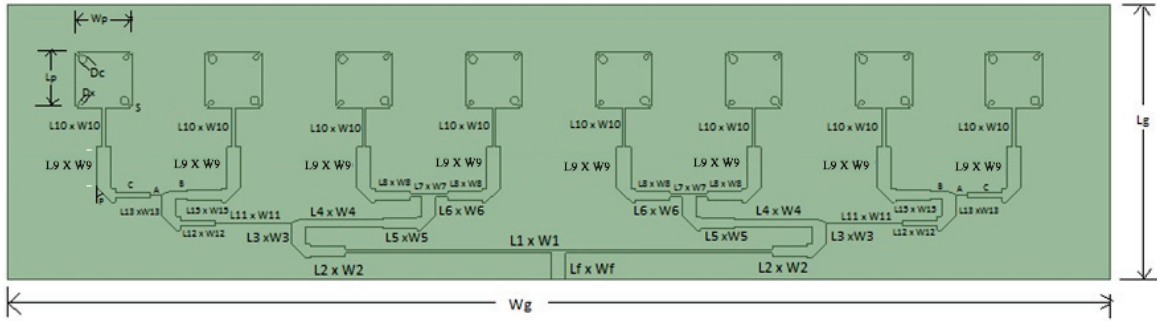


Fig. 2. Design of the proposed planar microstrip array.

power division and determine the physical dimensions of the proposed feed structure [20].

The proposed 1*8 element planar array is constructed using this feed structure and the single element circularly polarized patch antenna array as depicted in Fig. 2. and the optimal physical dimensions of the proposed antenna are given in Table 1.

Table 1: Physical dimensions of the proposed planar microstrip array

Parameters	Values
$L_g \times W_g$	39.23mm \times 157.83mm
$L_p \times W_p$	8mm \times 8mm
Dc	1.2
Dx	0.69
$L_f \times W_f$	4mm \times 2mm
$L_1 \times W_1$	0.4mm \times 60mm
$L_2 \times W_2$	1.2mm \times 4.8mm
$L_3 \times W_3$	2.4mm \times 2mm
$L_4 \times W_4$	1.1mm \times 10.8mm
$L_5 \times W_5$	1.7mm \times 4.9mm
$L_6 \times W_6$	2.5mm \times 2mm
$L_7 \times W_7$	0.5mm \times 5.5mm
$L_8 \times W_8$	1.4mm \times 4.9mm
$L_9 \times W_9$	7.8mm \times 2mm
$L_{10} \times W_{10}$	5.6mm \times 0.4mm
$L_{11} \times W_{11}$	0.15mm \times 11mm
$L_{12} \times W_{12}$	0.85mm \times 4.9
$L_{13} \times W_{13}$	2.4mm \times 1.8mm
$L_{15} \times W_{15}$	1.6mm \times 4.8mm
A	0.25mm \times 1.6mm
B	1mm \times 1.75mm
C	0.8mm \times 4.8mm
D	2mm \times 0.5mm
E	2mm \times 0.5mm
F	2mm \times 0.5mm
G	2mm \times 0.5mm
H	2mm \times 0.5mm
P	45°

The unequal power distribution to the individual patch elements is proportional to the 0.5:1:2:2:2:2:1:0.5 amplitude tapering ratio. The power divider at the T-junction is designed for this amplitude tapering ratio. The material chosen for antenna construction is 0.78 mm thick RT Duroid 5880. This substrate material's permittivity measures 2.2. For the construction of the proposed 1*8 element planar antenna array, the circularly polarized single element antenna and the proposed feed structure are combined. This proposed antenna is mounted conformally to the vehicle's roof, as depicted in Figs. 3 and 4, shown below.

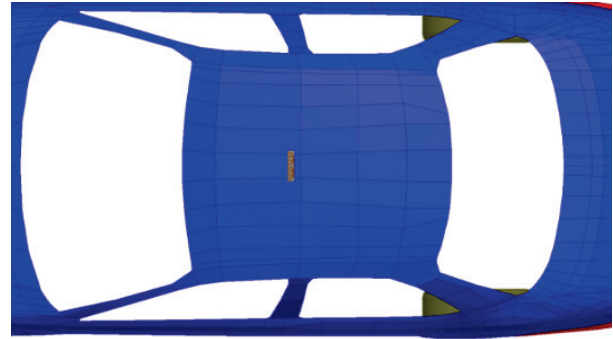


Fig. 3. Proposed conformal microstrip antenna array-top view.

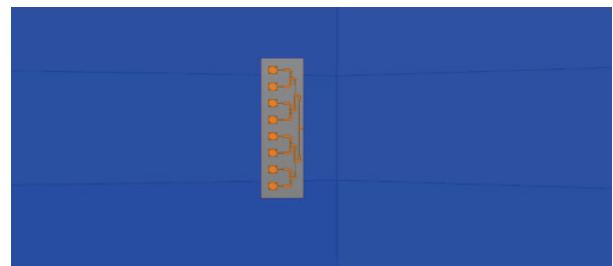


Fig. 4. Magnified top view of conformal microstrip antenna array.

The conformal placement of the proposed antenna reduces its visibility to human eyes and improves its mechanical properties, such as the reduction of aerodynamic drag. The rise in the number of antennas mounted on civilian vehicles makes the conformal antenna an attractive option for vehicle manufacturers.

III. RESULTS AND DISCUSSION

A. Planar microstrip antenna array proposed for vehicular SATCOM applications

Simulating the proposed antenna utilizes both the HFSS and CST suite tools. The reflection coefficient versus frequency graph is depicted in Fig. 5. The impedance bandwidth at -10 dB is measured using this graph, which is the industry standard. At a resonant frequency of 11.2 GHz, simulation results indicate an impedance bandwidth of 410 MHz, or 3.66% of the resonant frequency. The axial ratio of practically circularly polarized antennas should be less than 3. The axial ratio versus frequency graph is depicted in Fig. 6. This graph is used to evaluate the bandwidth of the axial ratio at 3 dB. Simulated results reveal an axial ratio bandwidth of 150 MHz at a resonant frequency of 11.2 GHz, which is 1.34% of the resonant frequency.

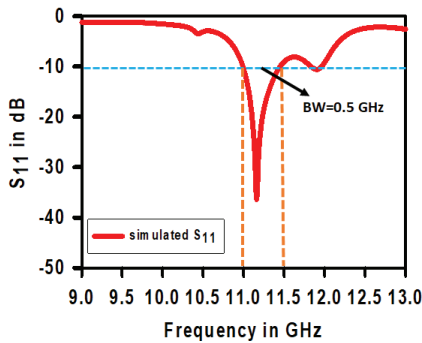


Fig. 5. Return loss versus frequency plot of proposed planar microstrip antenna array.

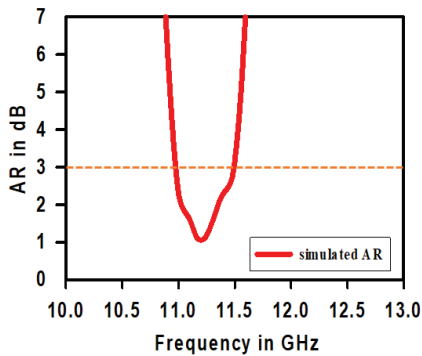


Fig. 6. Axial ratio versus frequency plot of proposed planar microstrip antenna array.

Figure 7 shown below depicts the linear gain versus theta relationship. The graph displays a maximum gain of 14 dB, and the difference in gain between co-polarization and cross-polarization is consistently greater than 15 dB. Figure 8 depicts the polar gain versus theta plot. Maximum gain is 13.54 dB, and the difference between co-polarization and cross-polarization gain is greater than 15 dB throughout the entire plot. Figure 9

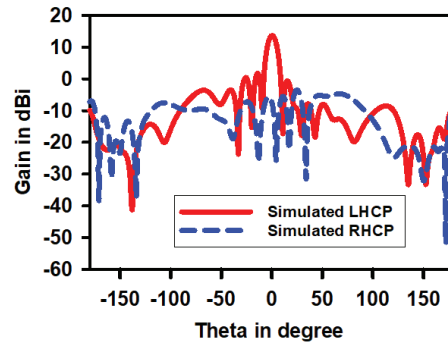


Fig. 7. Polarization gain versus theta linear plot of proposed planar microstrip antenna array.

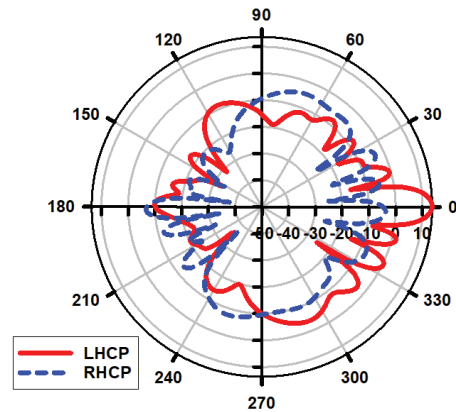


Fig. 8. Polar plot of polarization gain versus theta for proposed planar microstrip antenna.

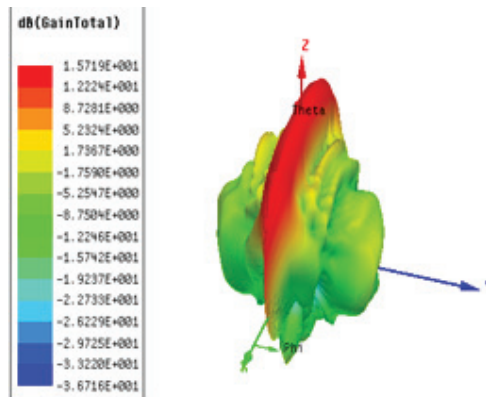


Fig. 9. 3D gain representation of the proposed planar microstrip antenna array.

illustrates the 3D gain versus frequency graph. The graph displays a maximum gain of 15.71 dB.

B. Conformal microstrip antenna array proposed for automotive SATCOM applications

Simulating the proposed antenna utilizes both the HFSS and CST suite tools. Figure 10 depicts a reflection coefficient versus frequency graph. The impedance bandwidth at -10 dB is measured using this graph, which is the industry standard. At the resonant frequency of 11.2 GHz, simulation results indicate an impedance bandwidth of 180 MHz, or 1.6% of the resonant frequency. The axial ratio of practically circularly polarized antennas should be less than 3. The axial ratio versus frequency graph is depicted in Fig. 11. This graph is utilized to assess the axial ratio bandwidth at 3 dB. Simulated

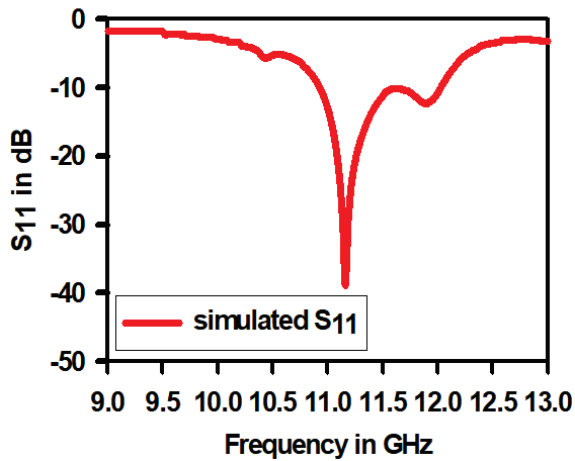


Fig. 10. Conformal microstrip antenna array return loss versus frequency plot.

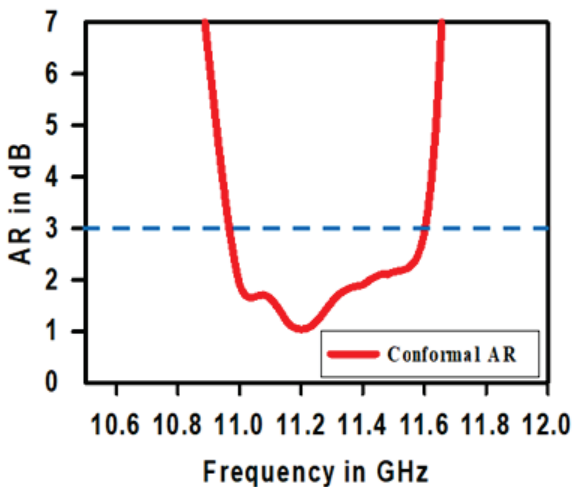


Fig. 11. Conformal microstrip antenna array axial ratio versus frequency plot.

results reveal an axial ratio bandwidth of 180 MHz at a resonant frequency of 11.2 GHz, which is 1.6% of the resonant frequency. Figure 12 depicts the graph of 3D gain versus frequency. The graph indicates a peak gain of 14.39 dB.

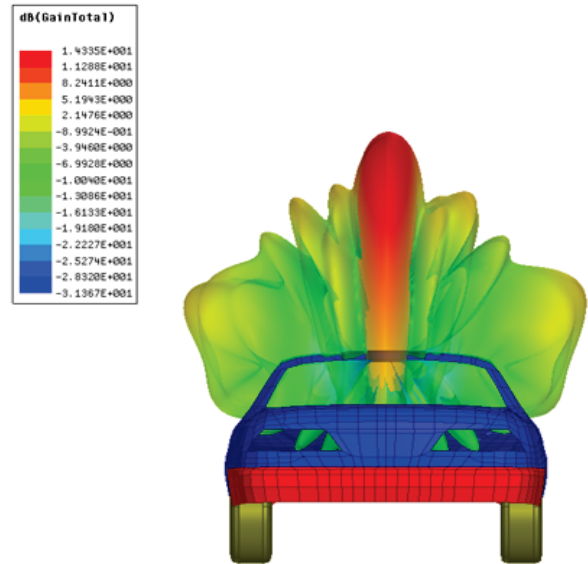


Fig. 12. 3D pattern of proposed conformal microstrip antenna array's far field.

C. Reduced side lobe levels

Figures 13 and 14 depict the far field directivity versus theta plot of the circularly polarized planar array with the existing feed and the proposed feed, respectively. The results demonstrate that the proposed feed's side lobe levels are 8.9 dB lower than the corporate feed.

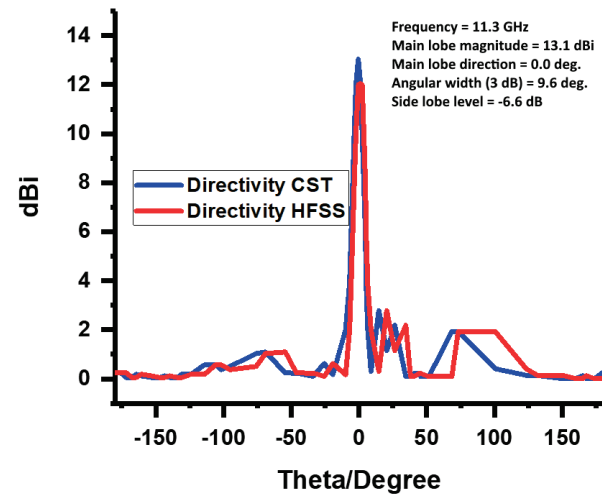


Fig. 13. Side lobe levels of a conventional-feed conformal antenna-directivity in Cartesian plot.

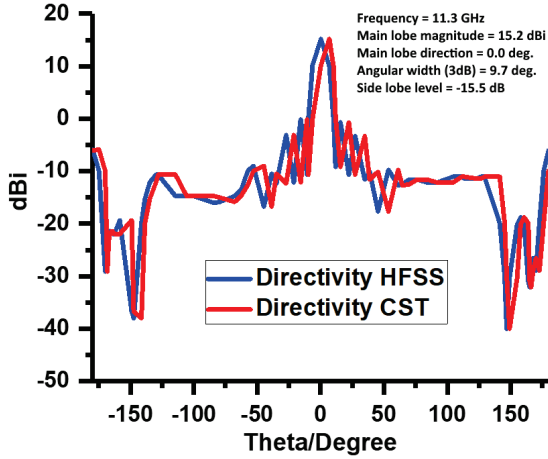


Fig. 14. Side lobe levels of conformal antenna with proposed feed-directivity in Cartesian plot.

D. Fabrication and testing

Figure 15 depicts the developed planar and conformal circularly polarized microstrip array antenna with a single element. These antennas were evaluated by measuring the various parameters of radiation characteristics using a test setup comprised of a transmitting Verdant JR12 horn antenna, Vector Network Analyzer, and anechoic chamber. Figure 16 depicts the proposed antenna

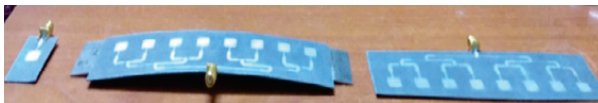


Fig. 15. Single-element proposed planar microstrip antenna array and conformal microstrip antenna array fabrication.

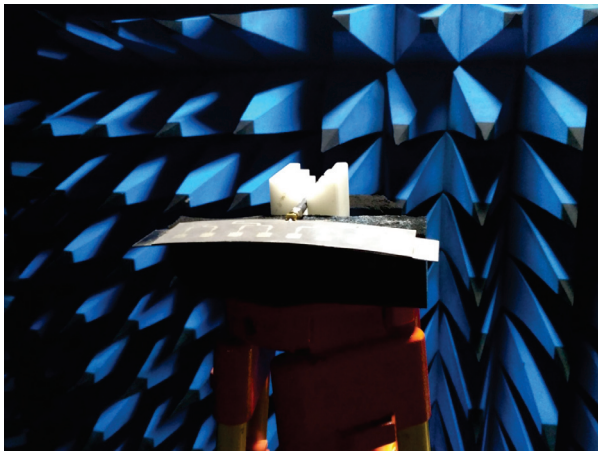


Fig. 16. Testing the proposed conformal microstrip antenna array in the anechoic chamber.

placed in the anechoic chamber for testing. The proposed antenna was measured with the transmitting Verdant JR12 horn antenna positioned at 2 metres distance apart. Figures 17, 18 and 19 depict simulation versus comparison plots for the various radiation characteristic parameters.

The proposed conformal microstrip antenna array is compared with similar antennas in recent research and is shown in Table 3 given above. At the resonant frequency, Figs. 18, 19, and 20 demonstrate good agreement between the simulated and measured values. Although the gain could not be measured directly using the test setup, it was calculated using the Friss transmission formula. Comparing the measured gain to the gain obtained through simulation, connector losses caused a slight decrease in gain. Table 2 provides a comparison between the measured radiation characteristic parameters of single element antenna, proposed planar array and proposed conformal array.

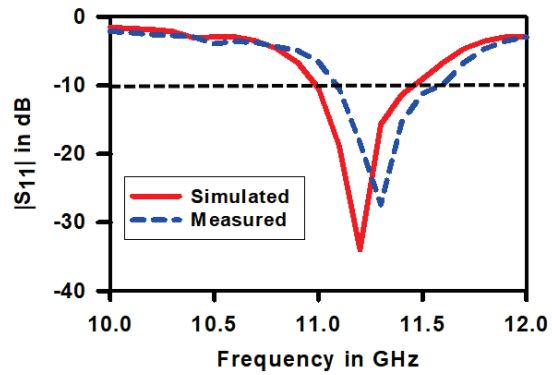


Fig. 17. Simulated versus measured return loss of proposed conformal microstrip antenna array.

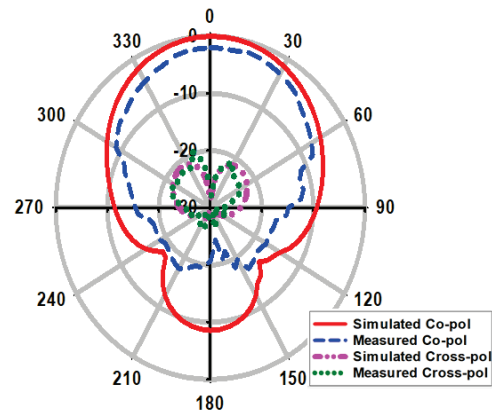


Fig. 18. Radiation pattern in the far field of the proposed conformal microstrip antenna array in the Y-Z plane (E-Plane).

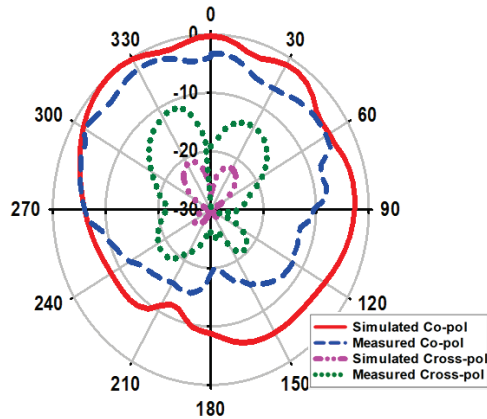


Fig. 19. Radiation pattern in the far field of the proposed conformal microstrip antenna array in the X-Z plane (H-Plane).

Table 2: Comparison of the measured results of single element antenna, proposed planar and proposed conformal microstrip antenna array

Parameter	Single Element Antenna	Proposed Planar Array	Proposed Conformal Array
Impedance Bandwidth (MHz)	490	400	170
Axial Ratio Bandwidth (MHz)	170	140	160
Gain (dB)	5.6	14	13.33

Table 3: Comparison of performance metrics of the proposed antenna with recent related works

Ref.	Resonant Frequency (GHz)	Gain (dBi)	Side Lobe Levels (dB)
[19]	11.2	5.6	-14.9
[21]	13	19.4	-16
[22]	12.2	25.3	<-26.5
[23]	4.3-7.4	5-6.5	around -15
[24]	9.3	11.39	-20
[25]	9.37	28	-25
This work	11.2	14.335	-15.5

IV. CONCLUSION

The proposed microstrip conformal circularly polarized antenna array has been designed, simulated, developed, tested, and measured for vehicular applications. RT 5880 material with a thickness of 0.78 mm was utilized as the substrate. The characteristics of the radiation were analyzed using both simulated and measured

data. The proposed feed structure reduces side lobe levels by 8.9 dB compared to the current feed structure. The measured results reveal 1 dB reduction in gain when compared to the simulation findings; however, the measured values are consistent with the simulation findings. According to the measured data, the proposed antenna has a gain of 13.33 dB, an impedance bandwidth of 1.6%, and an axial ratio bandwidth of 1.6%. The proposed antenna's enhanced axial ratio bandwidth and reduced side lobe levels make it the optimal low-profile antenna for vehicular SATCOM applications.

REFERENCES

- [1] Z. Zhao, G. Xu, N. Zhang, and Q. Zhang, "Performance analysis of the hybrid satellite-terrestrial relay network with opportunistic scheduling over generalized fading channels," *IEEE Transactions on Vehicular Technology*, vol. 71, no. 3, pp. 2914-2924, Mar. 2022.
- [2] H. K. Kim, Y. Cho and, H. S. Jo, "Adjacent channel compatibility evaluation and interference mitigation technique between earth station in motion and IMT-2020," *IEEE Access*, vol. 8, pp. 213185-213205, Nov. 2020.
- [3] A. D. Panagopoulos, M. P. Anastasopoulos, and P. G. Cottis, "Error performance of satellite links interfered by two adjacent satellites," *IEEE Antennas and Wireless Propagation Letters*, vol. 6, pp. 364-367, Oct. 2007.
- [4] W. Li, Q. Zhang, Y. Luo, Q. Zhang, and F. Jiang, "Development of a new multifunctional induced polarization instrument based on remote wireless communication technology," *IEEE Access*, vol. 8, pp. 100415-100425, May 2020.
- [5] L. Liu, Y. Yi, J.-F. Chamberland, and J. Zhang, "Energy-efficient power allocation for delay-sensitive multimedia traffic over wireless systems," *IEEE Transactions on Vehicular Technology*, vol. 63, no. 5, pp. 2038-2047, June 2014.
- [6] L. Zhang, S. Gao, Q. Luo, P. R. Young, W. Li, and Q. Li, "Inverted-S antenna with wideband circular polarization and wide axial ratio bandwidth," *IEEE Transactions on Antennas and Propagation*, vol. 65, no. 4, pp. 1740-1748, Apr. 2017.
- [7] Y. Yao, F. Shu, Z. Li, X. Cheng, and L. Wu, "Secure transmission scheme based on joint radar and communication in mobile vehicular networks," *IEEE Transactions on Intelligent Transportation Systems*, pp. 1-11, May 2023.
- [8] S. A. M. Ahmed, S. H. S. Ariffin, N. Faisal, and S. Com, "Overview of wireless access in vehicular environment (WAVE) protocols and standards," *Indian Journal of Science and Technology*, vol. 6, no. 7, pp. 4994-5001, July 2013.

- [9] M. M. Bilgic and K Yegin, "Low-profile wideband antenna array with hybrid microstrip and waveguide feed network for Ku band satellite reception systems," *IEEE Trans. Antennas Propag.*, vol. 62, no. 4, pp. 2258-2263, Jan. 2014.
- [10] F. Ananasso and F. D. Prisco, "The role of satellites in personal communication services," *IEEE Journal on Selected Areas in Communications*, vol. 13, no. 2, pp. 180-196, Feb. 1995.
- [11] A. I. Zaghoul, R. K. Gupta, E. C. Kohls, L. Q. Sun, and R. M. Allnutt, "Low cost flat antennas for commercial and military SATCOM terminals," *MILCOM Proceedings Communications for Network-Centric Operations: Creating the Information Force (Cat. No.01CH37277)*, vol. 2, pp. 795-799, Oct. 2001.
- [12] G. Comparetto and R. Ramirez, "Trends in mobile satellite technology," *Computer*, vol. 30, no. 2, pp. 44-52, Feb. 1997.
- [13] B. Cao, J. Zhang, X. Liu, Z. Sun, W. Cao, R. M. Nowak, and Z. Lvet, "Edge-cloud resource scheduling in space-air-ground-integrated networks for internet of vehicles," *IEEE Internet of Things Journal*, vol. 9, no. 8, pp. 5765-5772, Apr. 2022.
- [14] S. Jiang, C. Zhao, Y. Zhu, C. Wang, and Y. Du, "A practical and economical ultra-wideband base station placement approach for indoor autonomous driving systems," *Journal of Advanced Transportation*, vol. 2022, pp. 1-12, Mar. 2022.
- [15] Y. Li, K. An, T. Liang, and X. Yan, "Secrecy performance of land mobile satellite systems with imperfect channel estimation and multiple eavesdroppers," *IEEE Access*, vol. 7, pp. 31751-31761, Mar. 2019.
- [16] C. Chen, S. Wang, L. Li, S. Ke, C. Wang, and X. Bu, "Intelligent covert satellite communication for military robot swarm," *IEEE Access*, vol. 8, pp. 5363-5382, Dec. 2019.
- [17] S. Pan, M. Lin, M. Xu, S. Zhu, L.-A. Bian, and G. Li, "A low-profile programmable beam scanning holographic array antenna without phase shifters," *IEEE Internet of Things Journal*, vol. 9, no. 11, pp. 8838-8851, June 2022.
- [18] R. Masood and S. A. Mohsin, "No side-lobe condition for linear uniform broadside and end-fire antenna arrays," *IEEE 15th International Symposium on Antenna Technology and Applied Electromagnetics*, Toulouse, France, pp. 1-6, June 2012.
- [19] E. Abishek, A. Raaza, S. Ramesh, S. Jerritta, and V. Rajendran, "Circularly polarized circular slit planar antenna for vehicular satellite applications," *Applied Computational Electromagnetics Society (ACES) Journal*, vol. 34, no. 9, pp. 1340-1345, Sep. 2019.
- [20] D. M. Pozar and D. H. Schaubert, "Microstrip antenna array design," *Microstrip Antennas: The Analysis and Design of Microstrip Antennas and Arrays*, Wiley-IEEE Press, pp. 267-308, 1995.
- [21] U. Beaskoetxea, A. E. Torres-García, M. Beruete, "Ku-band low-profile asymmetric bull's-eye antenna with reduced sidelobes and monopole feeding," *IEEE Antennas and Wireless Propagation Letters*, vol. 17, no. 3, pp. 401-404, Mar. 2018.
- [22] L.-X. Wu, N. Zhang, K. Qu, K. Chen, T. Jiang, J. Zhao, and Y. Feng, "Transmissive metasurface with independent amplitude/phase control and its application to low-side-lobe metalens antenna," *IEEE Transactions on Antennas and Propagation*, vol. 70, no. 8, pp. 6526-6536, Aug. 2022.
- [23] F. Z. Abushakra, A. S. Al-Zoubi, and D. F. Hawatmeh, "Design and measurements of rectangular dielectric resonator antenna linear arrays," *Applied Computational Electromagnetics Society (ACES) Journal*, vol. 33, no. 4, pp. 380-387, July 2021.
- [24] Y. P. Saputra, F. Oktafiani, Y. Wahyu, and A. Munir, "Side lobe suppression for X-band array antenna using Dolph-Chebyshev power distribution," *22nd Asia-Pacific Conference on Communications (APCC)*, Yogyakarta, Indonesia, pp. 86-89, Aug. 2016.
- [25] L. Lu, L. Shu, W. Jun, L. Shoulan, Y. Caitian, and A. Denisov, "Simulation and analysis of an X-band low sidelobe and high gain microstrip antenna array," *International Symposium on Antennas and Propagation (ISAP)*, Phuket, Thailand, pp. 1-2, Oct. 2017.



0003-2908-7069.

Ebenezer Abishek is an Associate Professor at Vel Tech Multi Tech. Dr. Rangarajan Dr. Sakunthala Engineering College, Chennai. His research interests include antennas and electromagnetism.. He has ten years' teaching and 7 years' research experience. His ORCID is 0000-



0000-0002-2946-5296.

S. Ramesh is a Professor with 19 years' teaching experience at SRM Valliammai Engineering College in Chennai. He is a senior member of the IEEE Antennas & Propagation Society (S'10-M'17-SM'18) His research interests include antennas, propagation. His ORCID is



Parthasarathy Ramanujam is an Assistant Professor at the National Institute of Technology, Tiruchirappalli. His research interests include microwave components and circuits. His ORCID is 0000-0003-3179-0036.



E. Manikandan is a Senior Assistant Professor at the Centre for Innovation and Product Development and School of Electronics Engineering at Vellore Institute of Technology, Chennai. His research interests include antennas, micromachining and sensors. His ORCID is 0000-0002-0381-6406.

Unified Formulation for Evaluation and Visualization of Electric and Magnetic Fields Inside Waveguides and Cavities

Zahid Hasan and Atef Elsherbeni

Department of Electrical Engineering
Colorado School of Mines, Golden, CO 80401, USA
aelsherb@mines.edu

Abstract – The output of this research is an interactive software package developed to enhance and expedite the design of waveguides and cavity resonators through the computation and visualization of the electric and magnetic field distribution. The software features a user-friendly interface through which users can select one of seven different configurations and specify parameters of their design, such as structure dimensions, transverse electric or magnetic mode, mode numbers, operating frequency, number of points of any of the field components along the x, y, and z axis for rectangular structures, and any 2D plane angles between 0° to 360° for cylindrical structures. Both transverse and longitudinal field components can be visualized in vector, color contour or both. The software makes it easy for users to see how the changes of physical dimensions and operating frequency affect the field distribution. Moreover, the user interface allows users to select how visualizations of the field distribution are generated and displayed. Field distributions can be displayed as static images or video animations using appropriate sequencing of computed field values at different plane cuts. The software provides all necessary warning messages for invalid input parameters. Mathematical expressions of the field components used in this software were derived from the classical solution of the wave equations using the separation of variables technique in cartesian coordinates for rectangular configurations and cylindrical coordinates for all other configurations. Results obtained using this software were validated against values found in the literature for similar types of problems, and results show perfect agreement.

Index Terms – Cavity Resonators, Educational Software, EM Fields, Waveguides.

I. INTRODUCTION

The history of the development of waveguides is more than 100 years old. It was first discovered by George C. Southworth who played an important role in radar system design [1]. An electromagnetic field can-

not be seen directly [2], only its effects can be observed. Nowadays, technology is growing faster, and millimeter and sub-millimeter waves applications require a combination of active and passive devices. Usually, waveguide-based transmission lines are preferred in the design of low-loss filters, hybrid couplers, power dividers, antennas, etc. [3]. These applications require microwave devices to operate at higher frequencies (above 100 GHz). For operating at these frequency bands, waveguide size needs to be smaller and tolerance requirements need to be tightened. In medical applications, there is a growing need for wireless sensing systems [4]. Passive wireless sensors such as those used in harsh environmental conditions are generally composed of resonant circuits [5]. Cavity resonators are the most used component in passive wireless sensors. For cavity resonators, EM waves bounce back and forth between the cavity walls which produce field oscillations. Evanescent-mode cavity resonators inherently fulfill the need for high frequency passive wireless sensor applications because the size can be greatly reduced. But, with the growing demand for high speed, smaller size devices that consume less power, conventional manufacturing is becoming more and more challenging every day [6]. To the demands for small size and low-power consumption, microwave engineers must fully understand electromagnetic wave propagation inside waveguides and cavity resonators.

WGC (version 2.1) was developed in 1994 to compute and visualize EM field distribution inside waveguides and cavity resonators using an interactive BASIC language for a personal computer running DOS operating system [7]. The executable code of the software was available for the IBM-PC computer family, but it is no longer useable due to recent changes and advancements in computing technology and operating systems. Several software packages for designing and simulating microwave devices and transmission lines, such as Ansys HFSS, CST, and ADS are being used nowadays. For example, the design and simulation of a coplanar and air-gap waveguide transmission line using ADS has been

introduced in [8, 9]. CST studio suite has been used for similar design problem [10–12] and similarly HFSS as in [13–15]. These software packages are not only expensive, but they also require substantial memory and computational resources to compute and visualize field components inside such configurations of waveguides and cavities. Other software packages like COCAFIL [16] and XFDTD [17] are available, but they require substantial memory and computational resources. A web application to visualize the field pattern inside waveguide has been recently introduced in [18], but it is limited to waveguides with rectangular and circular cross-sections. The software package introduced here WGC (version 3) aims to overcome those challenges. It allows users to visualize the electric and magnetic field distribution inside several types of waveguides and cavity resonators (rectangular, circular, coaxial, baffle, sectoral, sectoral-coaxial, and baffle-coaxial) almost instantaneously on current PC platform. Advantages of using this software include the ability to model a wide variety of waveguide and cavity resonators, less memory requirements and computation time. WGC (version 3) features a user-friendly interface that makes easy for users to quickly model, compute and generate figures and video animations (using appropriate sequencing of computed field values at different plane cuts) of the EM field distribution within their design structure to assess the performance of their design.

WGC (version 3) allows user to observe the change of electric and magnetic fields distribution for different dimensions of the physical or electrical parameters of the cross-sections at different plane cuts. Also, users do not need to limit their interest in any specific mode of operation or order. They have a lot of flexibility in choosing among shapes, dimensions, mode numbers, plane views (x - y , x - z and y - z). Moreover, this software is capable of generating video animations of field distribution as the view angle and position changes. The code is executable on all modern computer families with installed MATLAB version 2021a and later versions. No internet connectivity is needed to run this software. The package can be downloaded from ACES site, software section.

II. MATHEMATICAL DERIVATION OF FIELD EQUATIONS

The objective of this section is to introduce different configurations of waveguide and cavity resonators used in WGC (version 3). The mathematical expressions of the field components are derived from the classical solution of the wave equation using the separation of variables technique.

Seven different cross-sections are considered in this software. These are rectangular, circular, sectoral, baffle, coaxial, sectoral coaxial, and baffle coaxial (see Fig. 1).

The electromagnetic wave is propagating along the z -axis and the boundary walls are assumed to be perfectly conductive. The waveguides and the cavity resonators are filled with homogeneous, isotropic, and lossless material with permeability denoted by μ and permittivity denoted by ϵ . The field equations for TE and TM modes are obtained after solving the Helmholtz wave equation inside the guide using the separation of variables technique. For rectangular geometry, the Cartesian coordinates system is considered and for the circular, sectoral, baffle, coax, sectoral coax, and baffle coax, the cylindrical coordinates system is used [19].

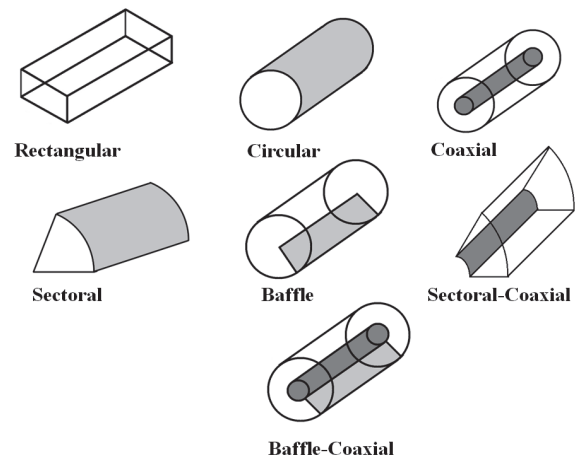


Fig. 1. Different cross-sections of waveguides and cavity resonators.

Rectangular Cross-Section: The fields in a rectangular waveguide and cavity resonator consist of several propagating modes which depend on the electrical dimensions, the type, and the position of excitation. Assuming the inner dimensions of the rectangular waveguide are a and b and d along the x , y , and z axes as shown in Fig. 2. A rectangular waveguide supports TM or TE mode but not TEM mode because a hollow rectangular waveguide does not have any inner conductor.

Circular and Coaxial Cross-Section: For the cross-section of circular waveguide and cavity, the radius is denoted by a and for the coaxial cross-section, a is the inner radius and b is the outer radius. The parameter d is the dimension along the propagation of waves as shown in Fig. 3.

Sectoral and Sectoral-Coaxial Cross-Section: The geometry of sectoral and sectoral-coaxial cross-section are shown in Fig. 4. The only difference is the value of m . For sectoral and sectoral-coaxial cross-section subscript m is a rational number.

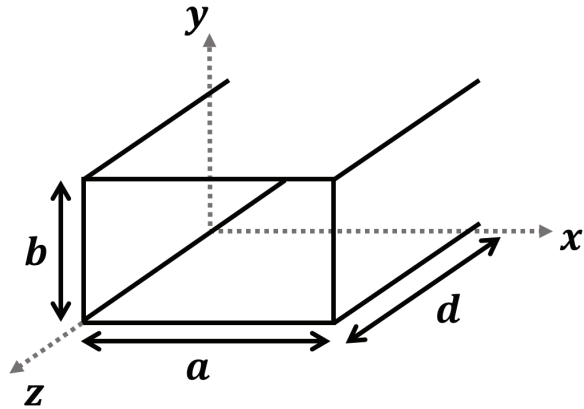


Fig. 2. Dimensional parameters of a rectangular waveguide or a cavity.

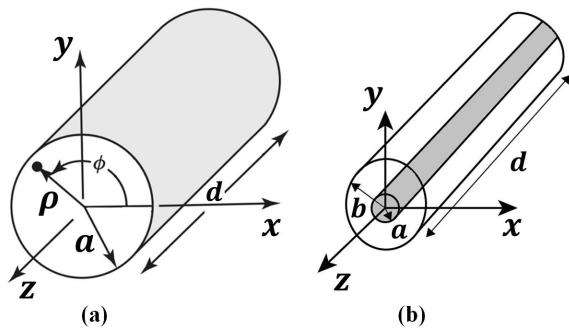


Fig. 3. Dimensional parameters of a waveguide or a cavity: (a) circular; (b) coaxial.

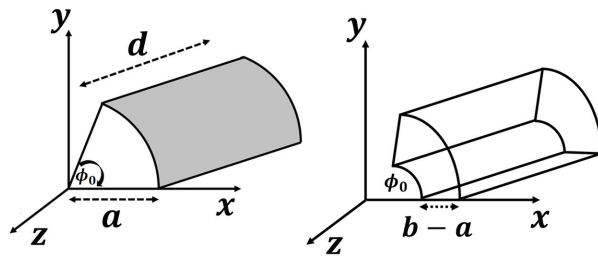


Fig. 4. Dimensional parameters of a sectoral and a sectoral-coaxial waveguide or a cavity.

Baffle and Baffle-Coaxial Cross-Section: When a conducting plate is inserted into a hollow cylindrical waveguide or cavity resonator, then the baffle configuration is created (see Fig. 5). The field equations for these configurations are similar to the circular except for the value of ϕ_0 . For baffle and baffle-coaxial waveguides and cavity resonators $\phi_0 = 2\pi$.

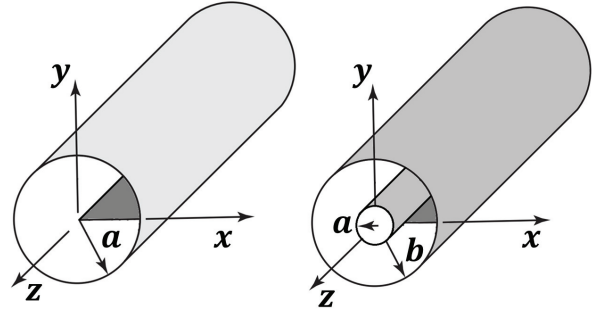


Fig. 5. Dimensional parameters of a circular baffle and a baffle-coaxial waveguide or a cavity.

III. SOFTWARE DESIGN

This section provides the design configuration of the software which will visually represent the electric and magnetic field distribution inside waveguides and cavity resonators for different modes of operation. The full software package is designed in the MATLAB App designer platform. First, field equations in this document have been verified with existing figures documented in [21, 22]. Then in MATLAB App designer, two windows are created to access the cross-sections of different waveguides and cavity resonators and later seven different windows are designed for seven different configurations of waveguides and cavity resonators.

MATLAB App Designer Platform: App designer helps to design professional apps. Simple drag and drop visual components in the app designer window help to layout the design of the graphical user interface (GUI) and to use the integrated editor to quickly program its behaviour. App designer has two view options, one is design view and another one is code view. In the design view window, one can easily layout the visual components from the component library. Each component has callback options that allow commanding individual components separately. Callback functions allow working in the code view window. Also, the code view window has property, functions, and app input arguments options which give the freedom to work in multiple app window settings. App Designer can automatically check for coding problems using the Code Analyzer. Standalone applications can be created by using MATLAB Compiler and Simulink Compiler to share them royalty-free with other users [20].

Graphical User Interface Development: Our software has nine different windows. The first window is called the main menu which will guide users to the next option menu. There a user can select which cross-section of a waveguide or a cavity they want to select. After that, the

user will be able to generate figures or create movies for different modes of operation in a waveguide or a cavity.

Layout and Operation of the Software: The layout of the software is mainly categorized into four main windows. Those are Main Window, Geometry Selection, and Parameters Screen and Output Screen (Figure and Video Creation). Each of them is described below.

Main Window: The window that will appear when a user starts the software is called the main window (shown in Fig. 6). In this window at the top of the left corner, there is a button called help. If the user selects this button, he/she will find two options there. One is about the app and the other will help the user find the contact details of the authors. In the main window, there is a big button called “Get Started”. When the user presses that button, it will lead to the next geometry selection window.

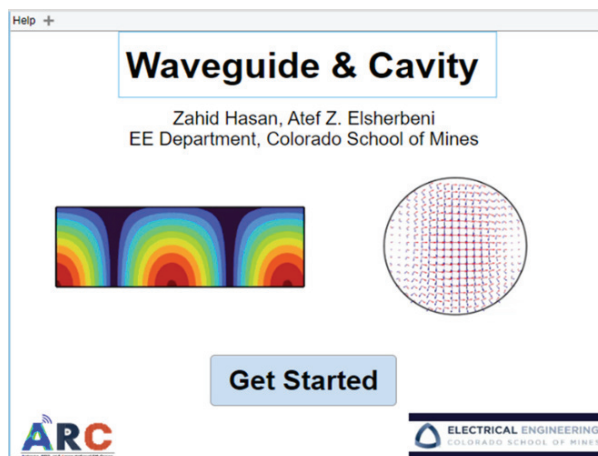


Fig. 6. Main window of WGC software.

Geometry Selection: The geometry selection (Options Menu) window is shown in Fig. 7. Seven different cross-sections are included. Those are rectangular, circular, sectoral, baffle, coaxial, sectoral-coaxial, baffle-coaxial cross-sections. When the user clicks any button beside a picture, the next window will open the parameters window of this picture geometry, and this geometry selection window will close automatically.

Parameters Screen: The parameters screen window is different for different geometry selections. Each of them has a waveguide or a cavity selection button, mode choice option, input for waveguide and cavity dimensions, operation frequency, and plane cut option. Also, there are cut-off, resonant frequency calculator option which depends on the dimensions of the cross-sections

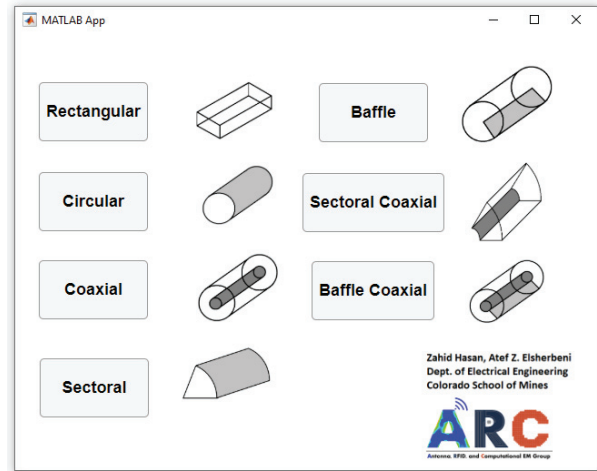


Fig. 7. Geometry selection window.

of waveguides and cavity resonators. The waveguide and cavity selection button will enable or disable some options (which are not needed) in the parameter screens. In the waveguide and cavity dimension box, three different units (cm, mm, and inch) are added in the drop-down menu. There is also an input for the number of points along the x, y, and z-axis. It will give the users the flexibility to see the propagation of electromagnetic waves as to how they want to see them. In the bottom of the left corner, there are two options for figure or video creation. Users can save their works as a picture as well as a video. The drop-down menu of the figure or video creation buttons, contains 5 different options. These are vector plot, E-field strength, H-field strength, E-field strength with vector, and H-field strength with vector. At the end of the right corner of the window there are three buttons called “Check”, “Run”, and “Return” buttons. The “Check” button checks all the input parameters. If there is an error in the input parameters, this “Check” button will show warning messages. Also, if the user puts some wrong inputs while trying to find the cut-off and resonance frequency for waveguides or cavity resonators, this “calculate” button will also show some warning messages. Initially, the “Run” button is kept deactivated so that users can easily understand the mistakes if they do any by pressing the “Check” button. If there is no error, the “Run” button will be activated, and the user will be able to see the picture or the video according to his/her options selection. Right below the Create figure and Video box, there is a text area where the user can see the message about the current figure or video creation status. The “Return” button will get the user return back to the geometry selection window to work further with the app. The parameters screen for rectangular cross-section is shown in Fig. 8.

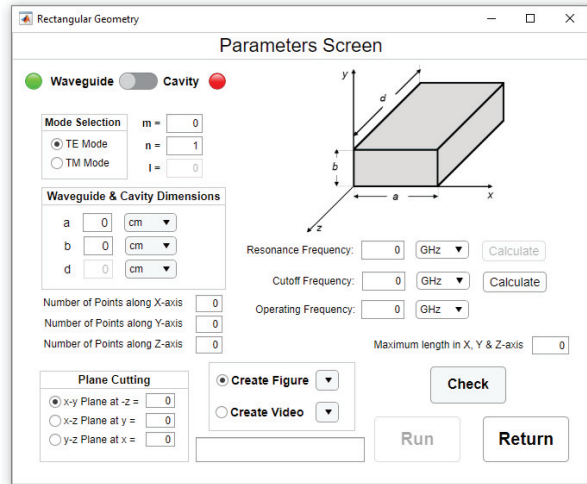


Fig. 8. Parameters screen window for rectangular waveguides and cavities.

Figures of EM Fields: When the user selects the “Create Figure” button, initially, it is selected for the vector plot. But the user can change the view option by pressing the drop-down menu just beside the button. After creating one figure the user does not need to exit the figure window to see another configuration of input parameters. This will help the user to compare figures by placing them side by side. And after that, the user can save those images in whichever directory they want to select.

Video Animations of EM Fields: The video creation option is pretty much like the figure creation option. The animation is created using an appropriate sequencing of computed field values at different plane cuts. For creating a video, more time is needed than figure creation. So, at that time a progress bar and successful bar are included so that the user can understand that the video is being created, and it will take some time. When the video creation is completed, a success message will appear and telling the user that the movie creation is successful.

IV. ILLUSTRATED EXAMPLES

This section provides illustrated examples of software functionality. Each parameters screen has the option to switch between waveguide and cavity. The default position of the switch is for waveguide. When a user slides the switch to cavity, the red light next to it turns green and the green light next to the waveguide turns red. When the user changes the switch position back to waveguide, the light color will change again. This way, a user receives feedback from the software confirming which of the two configurations is active. Figure 9 shows different options and dropdown menus

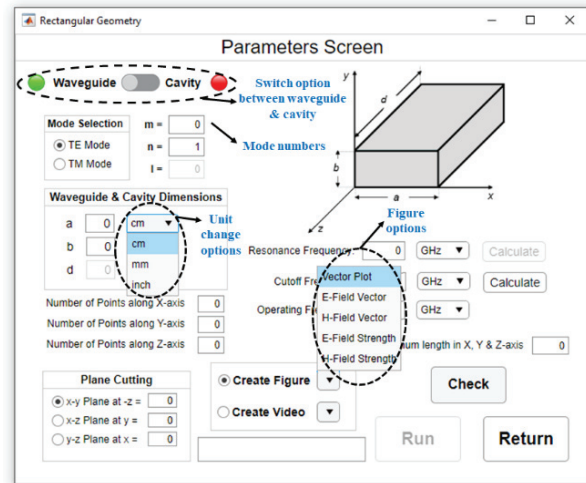


Fig. 9. Different options in parameters screen window.

in the parameters screen window. Initially the “Run” button is disabled. If all inputs are valid, then after clicking the “Check” button no error is shown and that enables the “Run” button. The “Return” button will take users back to the geometry selection window. For invalid inputs, users will be warned by showing error messages. While checking the error, the software automatically disables the “Run” button, and this makes the user understand that some corrections need to be done. Figure 10 shows a warning message for invalid input in the mode number.

Figures for Waveguide: For valid inputs, some figures of the coaxial and sectoral-coaxial waveguide for different views are shown here in Figs. 11–14.

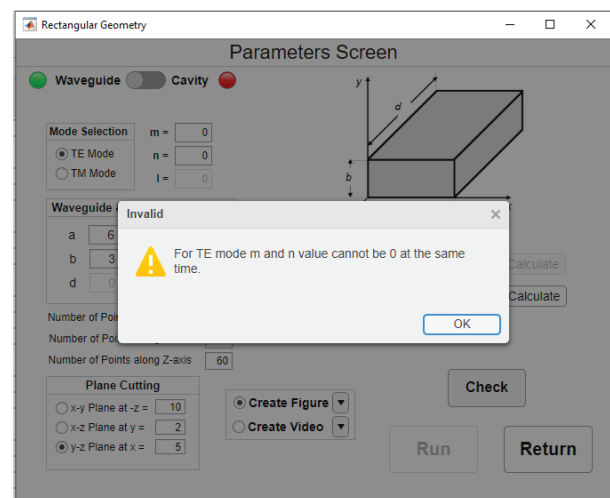


Fig. 10. Checking the error message for invalid mode number.

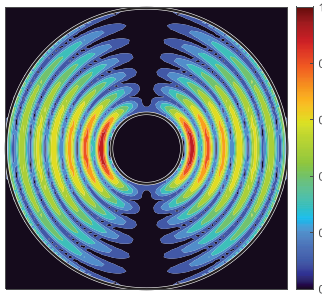
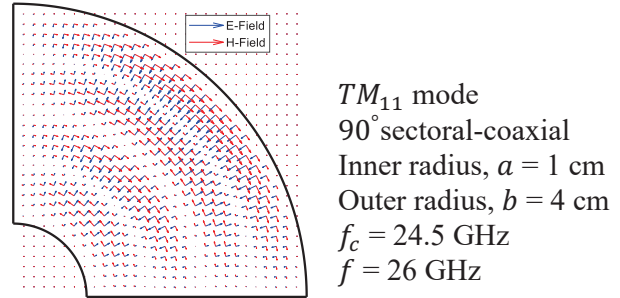
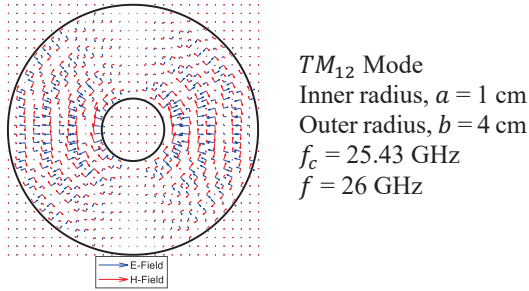


Fig. 13. Cross-sectional vector fields for the TM_{11} mode of a 90° sectoral coaxial waveguide.

Fig. 11. Vector and field strength of E-Field or H-Field for TM_{12} mode of a coaxial waveguide.

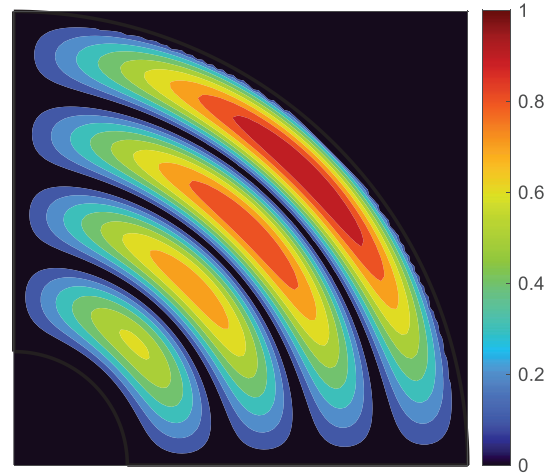
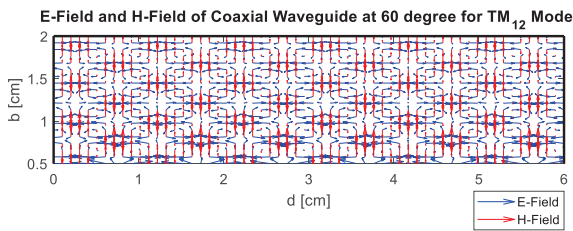
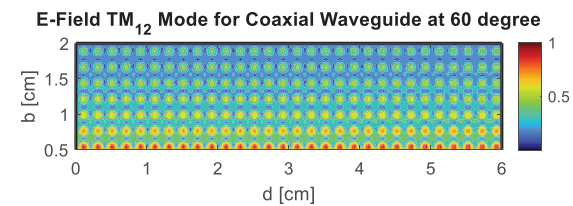


Fig. 14. E-Field and H-Field strength at the cross-section of a 90° sectoral coaxial waveguide for TM_{11} mode.



given for baffle and baffle-coaxial cavity as shown in Figs. 15–18.



This section provided illustrated examples (Figs. 11–18) for various cross-sections of waveguide and cavity resonator configurations. For rectangular cross-section, users can view the field pattern in x-y, x-z and y-z axis. For cylindrical cross-sections, users can

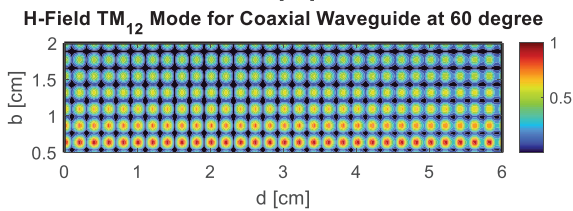


Fig. 12. Vectors and field strength for TM_{12} mode in the 60° plane cut of a coaxial waveguide.

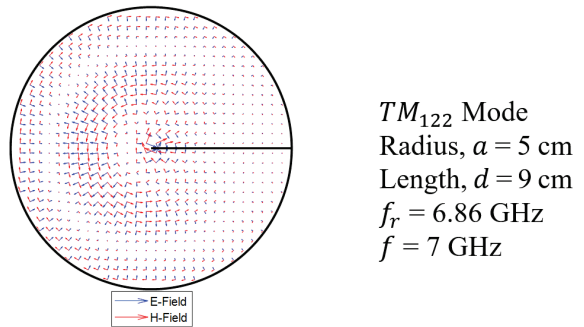


Fig. 15. Cross-sectional vector fields for the TM_{122} mode of a baffle cavity.

Figures for Cavity: Switching to cavity mode, activates some input parameters in the parameters screen. Those input parameters have no function in the waveguide mode and that is why those are inactive in the waveguide mode. Illustrated examples have been

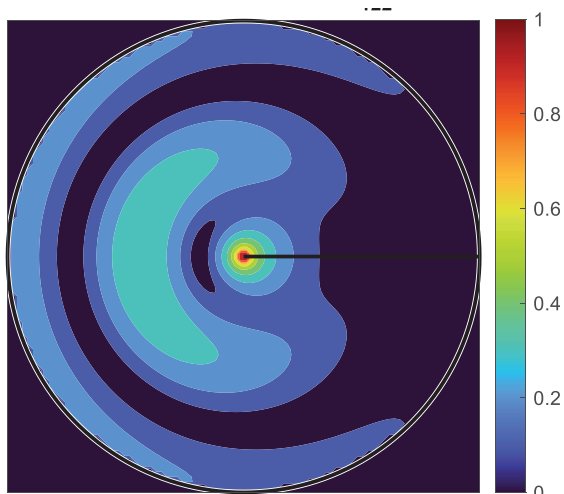


Fig. 16. E-Field and H-Field strength at the cross-section of a baffle cavity for TM_{122} mode.

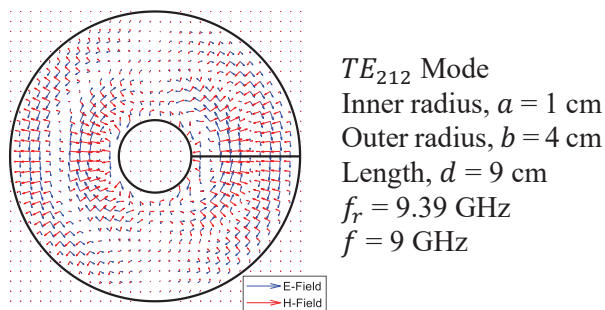


Fig. 17. Cross-sectional vector fields for the TE_{212} mode of a baffle-coaxial cavity.

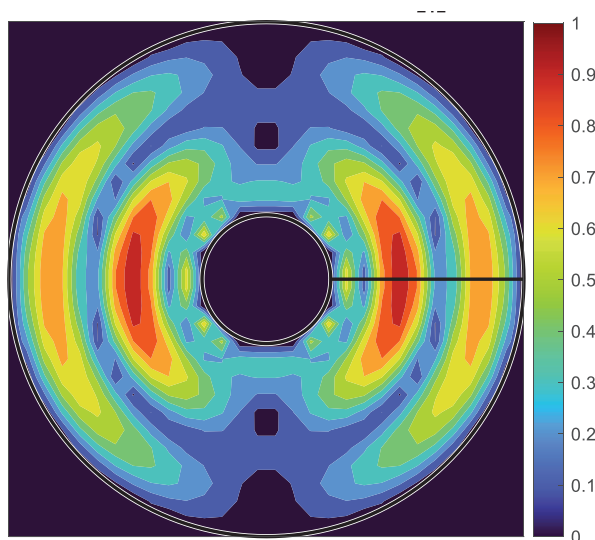


Fig. 18. E-Field and H-Field strength at the cross-section of a baffle-coaxial cavity for TE_{212} mode.

view field distribution in x-y axis and in any arbitrary angle between 0° and 360° . However, since the sectoral cross-sections limits the geometry structure with the angle ϕ_0 , users can observe field pattern between 0° and ϕ_0 degrees. If users input in the view angle is greater than the sectoral angle ϕ_0 , for sectoral and sectoral-coaxial cross-sections, WGC will show warning messages.

V. CONCLUSION

Coding languages used to build WGC (version 2.1) are no longer available and the major advanced in computer technology, rendered the software unusable. This research is the rework and major update of the waveguide and cavity software (WGC version 2.1). The revival of the software was essential to compute and visualize the electric and magnetic fields inside waveguides and cavity resonators on current computing platforms. Several enhancements were made to make the software more powerful and user-friendly.

The software package presented in this paper WGC (version 3) has been developed in the MATLAB App designer platform. WGC's graphical user interface (GUI) is easy to use and self-explanatory. The main window provides information about the software and the contact info of the authors. Users are able to select one of the seven cross-sections listed by names along with graphical representation. Based on selected cross-section, the appropriate parameters screen is displayed to allow the user to enter physical dimensions, operating frequency and select how to visualize the results. Warning messages are generated for invalid input parameters. WGC allows users to save the computed field values for comparison and validation against theoretical calculations and measurements.

Performance evaluation of WGC through comparisons with HFSS and CST's computational time and memory requirements for similar waveguides and cavity resonators problem, may be conducted for benchmarking purposes. Future work also includes research on the development of mathematical expressions for dielectric, partially filled, and rigid waveguides and cavity resonators for inclusion as modelling options in the software.

REFERENCES

- [1] K. S. Packard, "The origin of waveguides: A case of multiple rediscovery," *IEEE Transactions on Microwave Theory and Techniques*, vol. 32, no. 9, pp. 961-969, 1984.
- [2] N. N. Rao, "PC-assisted instruction of introductory electromagnetics," *IEEE Transactions on Education*, vol. 33, no. 1, pp. 51-59, 1990.
- [3] S. Farjana, M. Ghaderi, A. U. Zaman, S. Rahiminejad, P. Lundgren, and P. Enoksson, "Low-loss gap

- waveguide transmission line and transitions at 220–320 GHz using dry film micromachining,” *IEEE Transactions on Components, Packaging and Manufacturing Technology*, vol. 11, no. 11, pp. 2012–2021, 2021.
- [4] REMCOM, “How to build a rectangular waveguide in XFDTD,” *Remcom Inc State College, PA*, [Online].
- [5] Y. Zhao, Y. Li, B. Pan, S. H. Kim, Z. Liu, M. M. Tentzeris, J. Papapolymerou, and M. G. Allen, “RF evanescent-mode cavity resonator for passive wireless sensor applications,” *Sensors and Actuators A: Physical*, vol. 161, no. 1-2, pp. 322–328, 2010.
- [6] A. Sahu, V. K. Devabhaktuni, R. K. Mishra, and P. H. Aaen, “Recent advances in theory and applications of substrate-integrated waveguides: a review,” *International Journal of RF and Microwave Computer-Aided Engineering*, vol. 26, no. 2, pp. 129–145, 2016.
- [7] A. Z. Elsherbeni and C. D. Taylor, “Interactive visualizations of electromagnetic fields inside waveguides and cavity resonators using the WGC program,” *Computer Applications in Engineering Education*, vol. 2, no. 2, pp. 97–107, 1994.
- [8] F. D. Mbairi and H. Hesselbom, “High frequency design and characterization of SU-8 based conductor backed coplanar waveguide transmission lines,” in *Proceedings. International Symposium on Advanced Packaging Materials: Processes, Properties and Interfaces, 2005*, pp. 243–248, 2005.
- [9] I. Jeong, S. H. Shin, J. H. Go, J. S. Lee, C. M. Nam, D. W. Kim, and Y. S. Kwon, “High-performance air-gap transmission lines and inductors for millimeter-wave applications,” *IEEE Transactions on Microwave Theory and Techniques*, vol. 50, no. 12, pp. 2850–2855, 2002.
- [10] F. Taringou, D. Dousset, J. Bornemann, and K. Wu, “Substrate-integrated waveguide transitions to planar transmission-line technologies,” in *2012 IEEE/MTT-S International Microwave Symposium Digest*, pp. 1–3, 2012.
- [11] J. Shi, H. Chen, S. Zheng, D. Li, R. Rimmer, and H. Wang, “Comparison of measured and calculated coupling between a waveguide and an RF cavity using CST microwave studio,” Thomas Jefferson National Accelerator Facility, Newport News, VA, technical report, 2006.
- [12] E. Pucci, A. U. Zaman, E. Rajo-Iglesias, P.-S. Kildal, and A. Kishk, “Losses in ridge gap waveguide compared with rectangular waveguides and microstrip transmission lines,” in *Proceedings of the Fourth European Conference on Antennas and Propagation*, pp. 1–4, 2010.
- [13] N. A. Amoli, S. Sivapurapu, R. Chen, Y. Zhou, M. L. Bellaredj, P. A. Kohl, S. K. Sitaraman, and M. Swaminathan, “Screen-printed flexible coplanar waveguide transmission lines: Multi-physics modeling and measurement,” in *2019 IEEE 69th Electronic Components and Technology Conference (ECTC)*, pp. 249–257, 2019.
- [14] S. H. Kamath, R. Arora, and V. Agarwal, “Studying the characteristics of a rectangular waveguide using HFSS,” *International Journal of Computer Applications*, vol. 118, no. 21, pp. 5–8, 2015.
- [15] Y. Zhou, H. Liu, E. Li, G. Guo, and T. Yang, “Design of a wideband transition from double-ridge waveguide to microstrip line,” *International Conference on Microwave and Millimeter Wave Technology*, pp. 737–740, 2010.
- [16] Zeland Software Inc., Fremont, CA, “Software for optimizing the design and low-cost production of waveguide filters,” *Microwave Journal*, [Accessed: March 24, 2022]: <https://www.microwavejournal.com>, 2002.
- [17] M. Al Ameen, J. Liu, and K. Kwak, “Security and privacy issues in wireless sensor networks for healthcare applications,” *Journal of medical systems*, vol. 36, no. 1, pp. 93–101, 2012.
- [18] S. Mitheran, R. T. Narayanan, and R. Singaravelu, “User-friendly waveguide mode visualizer, Educator’s corner,” *IEEE Microwave Magazine*, vol. 23, no. 5, pp. 96–100, 2022.
- [19] A. Z. Elsherbeni and C. D. Taylor, Jr., “Electromagnetic Fields Inside Waveguides and cavity resonators; WGC (version 2.1),” *Software Book II*, Center on Computer Applications for Electromagnetic Education (CAEME), 1994.
- [20] MathWorks, “App designer-create desktop and web apps in MATLAB,” *Mathworks Natick, MA*, <https://www.mathworks.com> [Accessed: August 01, 2021].
- [21] C. A. Balanis, *Advanced Engineering Electromagnetics*. John Wiley & Sons, 2012.
- [22] A. Elsherbeni, D. Kajfez, and S. Zeng, “Circular sectoral waveguides,” *IEEE Antennas and Propagation Magazine*, vol. 33, no. 6, pp. 20–27, 1991.



Zahid Hasan completed his B.Sc. and M.Sc. from the Department of Electrical and Electronic Engineering at University of Dhaka, Bangladesh. He earned his second master's degree in the Electrical Engineering department of Colorado School of Mines. He was employed as a teaching assistant there and a member of the ARC Research Group directed by Dr. Atef Elsherbeni.

Currently, he is pursuing his Ph.D. degree at the Electrical and Computer Engineering department at University of Central Florida. At the first year of his Ph.D., he was awarded the ORCGS Doctoral Fellowship at UCF. He is also employed as a research assistant and a member of the ARMI Research Group directed by Dr. Xun Gong. Besides, he is serving as a secretary in the IEEE AP/MTT chapter in Orlando.



Atef Z. Elsherbeni received an honor B.Sc. degree in electronics and communications, an honor B.Sc. degree in applied physics, and a M.Eng. degree in electrical engineering, all from Cairo University, Cairo, Egypt, in 1976, 1979, and 1982, respectively, and a Ph.D.

degree in electrical engineering from Manitoba University, Winnipeg, Manitoba, Canada, in 1987. He started his engineering career as a part-time software and system design engineer from March 1980 to December 1982 at the Automated Data System Center, Cairo, Egypt. From January to August 1987, he was a post-doctoral fellow at Manitoba University. Dr. Elsherbeni joined the faculty at the University of Mississippi in August 1987 as an assistant professor of electrical engineering. He advanced to the rank of associate professor in July 1991, and to the rank of professor in July 1997. He was the associate dean

of the college of Engineering for Research and Graduate Programs from July 2009 to July 2013 at the University of Mississippi. He then joined the Electrical Engineering and Computer Science (EECS) Department at Colorado School of Mines in August 2013 as the Dobelman Distinguished Chair Professor. He was appointed the interim department head for (EECS) from 2015 to 2016, and from 2016 to 2018 he was the Electrical Engineering Department head. He spent a sabbatical term in 1996 at the Electrical Engineering Department, University of California at Los Angeles (UCLA) and was a visiting professor at Magdeburg University during the summer of 2005 and at Tampere University of Technology in Finland during the summer of 2007. In 2009 he was selected as Finland Distinguished Professor by the Academy of Finland and TEKES.

Over the years, Dr. Elsherbeni participated in acquiring millions of dollars to support his research group activities dealing with scattering and diffraction of EM waves by dielectric and metal objects, finite difference time domain analysis of antennas and microwave devices, field visualization and software development for EM education, interactions of electromagnetic waves with the human body, RFID and sensor integrated RFID systems, reflector and printed antennas and antenna arrays for radars, UAV, and personal communication systems, antennas for wideband applications, and measurements of antenna characteristics and material properties. Dr. Elsherbeni is an IEEE life fellow and ACES fellow. He is the editor-in-chief for *ACES Journal*, and a past associate editor to the *Radio Science* journal. He was the chair of the Engineering and Physics Division of the Mississippi Academy of Science, the chair of the Educational Activity Committee for IEEE Region 3 Section, and the general chair for the 2014 APS-URSI Symposium and the president of ACES Society from 2013 to 2015. Dr. Elsherbeni is selected as distinguished lecturer for IEEE Antennas and Propagation Society for 2020-2023.

CMOS High Swing and Q Boosted Dual Core Voltage Controlled Oscillator for 5G New Radio Application

Pravinah Shasidharan¹, Jagadheswaran Rajendran¹, Selvakumar Mariappan¹,
Narendra Kumar², and Masuri Othman³

¹Collaborative Microelectronic Design Excellence Center (CEDEC)
Universiti Sains Malaysia, Sains @USM, Bayan Lepas (Penang), 11900, Malaysia
pravinah.shasidharan@student.usm.my, jaga.rajendran@usm.my, selva_kumar@usm.my

²Department of Electrical Engineering, Faculty of Engineering
University of Malaya, Kuala Lumpur, 50603 Malaysia
narendra.k@um.edu.my

³Institute of Microengineering and Nanoelectronics
National University of Malaysia
Bangi, 43600, Malaysia
masuri@ukm.edu.my

Abstract – This paper describes a low power, low phase noise CMOS voltage controlled oscillator (VCO) with a cascoded cross-coupled pair (XCP) configuration for high data rate 5G New Radio (5G-NR) applications. The core consists of a primary auxiliary VCO built as a negative conductance circuit to improve phase noise and a secondary core with a cascoded formation to increase output voltage swing. A switched varactor array (SVA) wideband tuner is integrated for a wide bandwidth application in a low power implementation. The dual-core VCO was designed in CMOS 130 nm technology and occupies only 1.05 mm² of space. With a supply voltage of 1.2 V, the VCO achieved a tuning range of 32.43% from 3.45 GHz to 4.47 GHz. At 3.96 GHz carrier center frequency with 1 MHz offset, the total power consumption is 0.7 mW with a corresponding phase noise (PN) of –121.25 dBc/Hz and a Figure of Merit (FoM) of 193.25 dBc/Hz. The results are validated using Cadence Spectra RF simulations.

Index Terms – cascode, CMOS, cross-coupled pair, 5G, New Radio, Q enhancement, switched varactor array (SVA), Voltage Controlled Oscillator.

I. INTRODUCTION

The 5th generation radio system is entirely dependent on fast data rates and low latency. This raises the bar for improved front-end system performance, particularly in the transceiver system. In general, any transceiver system requires a stable oscillator that provides low

noise performance while also consuming little power. The power consumption should be low enough to avoid exorbitant maintenance costs, such as frequent battery replacement and higher manufacturing costs. It is still a challenge today, as many oscillators with low power consumption have difficulty achieving low phase noise and wide bandwidth applications. Wideband applications have made extensive use of switched active cores [1–2]. The switched inductor array, which greatly increased the chip's area is the most widely used for bandwidth extension. Many digital switches experience a variety of issues, which contribute to the complexity of tuning voltages as well as the risk of tuning range gaps [3–5]. However, a novel varactor [6] has been proposed to broaden the tuning range using a single varactor without the need for digital control signal tuning achieving a tuning range of 40.3%. Some work encounters a disadvantage in improving phase noise at the expense of increased die area and a low quality factor (Q). Work [7] implements a Q enhancement and filtering technique without affecting the tank circuit's inductor component. To reduce the noise, a narrow band filter with a capacitor is placed on the current source [8].

Another method is to bias the capacitor placed between the gate and drain of the tail current source at twice the oscillation frequency of the resonant tank in order to suppress the flicker noise cause by the active devices. The transistor has been cleverly designed to be cycled between strong inversion and accumulation mode operation to reduce flicker noise contribution [9]. Aside from that, another technique has been implemented that

involves operating the transistor in the weak inversion (WI) region to achieve low power performance at the expense of poor process, voltage and temperature (PVT) variation [10]. The current reuse technique has been proposed to reduce power consumption, but the drawback is that it causes some asymmetrical output in the amplitude of the oscillation swing, which triggers flicker noise up-conversion and degrades the performance of the VCO’s phase noise [11–15]. Another approach, on the other hand, has been taken to properly model the varactor noise in order to reduce an avalanche phenomenon that can cause controllable phase noise [16].

However, extreme action is required at the varactor device to avoid device degradation caused by enormous high breakdown when VCO output swing is large. As a low phase noise VCO, being unaware of the effect of varactor breakdown noise may result in difficult simulation results. In this work a dual-core VCO is implemented, with the primary core acting as a Q enhancement circuit without affecting the structure of the tank inductor and the secondary core acting as a high swing trigger. Both cores have an adequate biasing scheme and have attained a suitable biasing point for better phase noise under low power consumption. The remainder of the paper is structured as follows. The principle of operation and its design concept are explained in detail in section II. Section III presents the performance reliability results and section IV concludes.

II. PRINCIPLE OF OPERATION AND DESIGN CONCEPT

A. Dual core VCO circuit design

Figure 1 illustrates the design flow chart that describes the top-down approach which starts with mathematical analysis on determining the Q factor for the

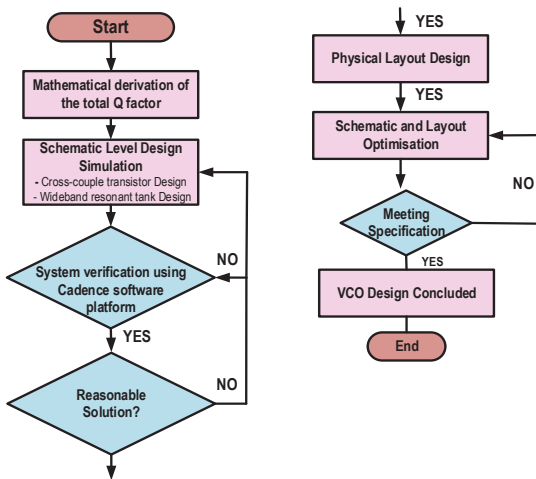


Fig. 1. Flow chart of the design flow for the proposed VCO

proposed circuit. Predetermined simulations and system verification were performed under the Cadence environment. Here, the schematic to the layout process flow is achieved with further optimization until the proposed specifications are met. With this, the proposed wideband, low power, dual core VCO is shown in Fig. 2. The architecture of the VCO consists of two sets of cores: the primary auxiliary core and the secondary core. The auxiliary structure comprises of the cross-coupled pairs N_1 and N_2 stacked on top of the cross-coupled pairs, N_3 and N_4 , which function as a gain booster and contributes to an increase of the Q factor via the bias voltage, V_P . The secondary core, consisting of a cascode pseudo differential pair comprised of N_5 to N_8 , is gate driven using a single biasing voltage, V_S . The transistors are sized symmetrically and merged with the primary core in order to improve the VCO’s swing and start-up. The resistors and capacitor, R_1C_2 and R_2C_1 , are dynamically biased to permit a wider output swing at the nodes of the V_{out+} and V_{out-} , which is sufficient to meet an oscillator’s start-up condition. The VCO is equipped with a wideband tuner consisting of an inductor, L_1 and a switched varactor array, SVA which are arranged in parallel and consist of the multiple tuner voltage V_{TUNE1} through V_{TUNE4} . For wideband operation, the capacitor values of the varactor capacitors are sized differently.

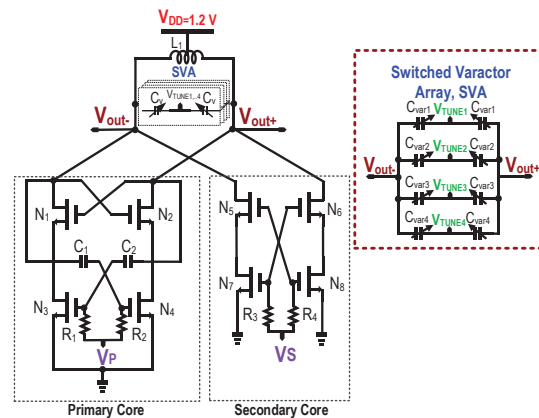


Fig. 2. Proposed LC-VCO with dual core VCO.

B. Theory of operation of primary core

As observed in Fig. 3 which shows the circuit operation of the primary core where Fig. 3 (a) shows the detail representation of the primary core of a cross couple structure (XCP) whereas Fig. 3 (b) shows a model of the cross-couple structure’s small signal equivalent. Two feedback-biased cross-coupled devices which linked to the feedback-biased voltage, V_P provide the drain current flows of $I_{1,3}$ and $I_{2,4}$ respectively. When oscillation begins, the differential oscillator signal, V_{out+} and V_{out-} determine the conduction mode of the stacked transistor

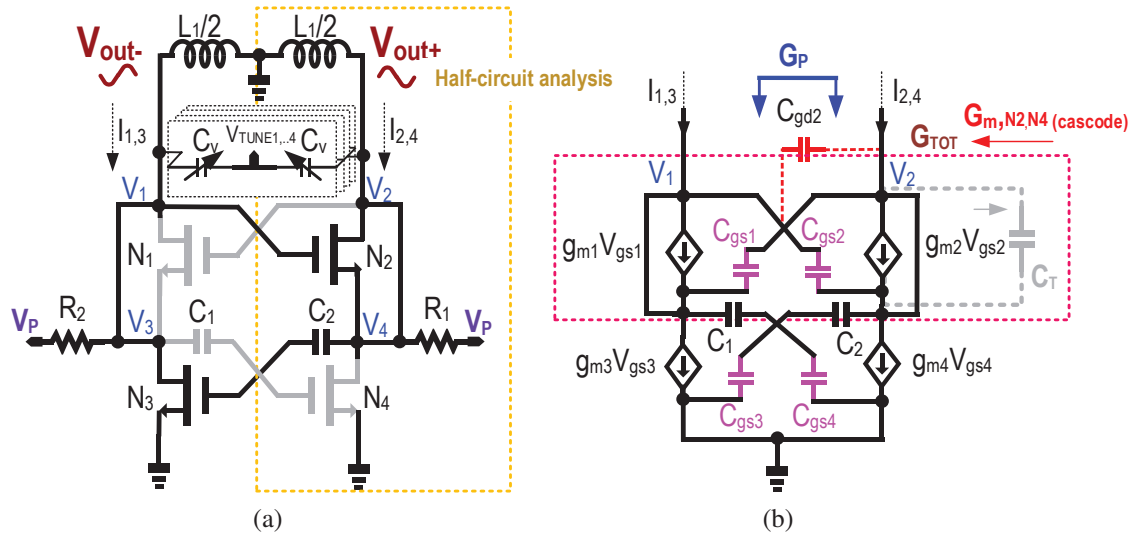


Fig. 3. Primary core (a) circuit and (b) small signal equivalent model.

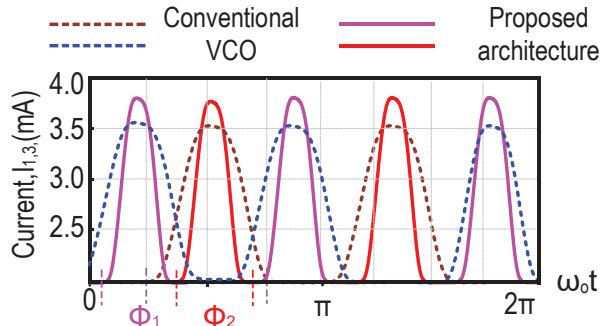


Fig. 4. Simulated MOS current waveform for the dual core conduction.

N_1 - N_4 . Figure 4 shows the drain current of transistors N_1 and N_4 become zero when the local oscillator (LO) switches to Φ_1 . The conduction period of the LO signal is shown in Fig. 5.

Hence, when the LO switches during the Φ_2 interval, N_3 and N_2 are both fully on while N_1 and N_4 are both fully off. The current flowing to the output has been inverted since the pair of transistors have been switched alternately. In this repeated process, the cross-coupled switches encounter a sync up session with the push pull mechanism, which changed the polarity of the VCO output signal. According to the small signal equivalent circuit shown in Fig. 3 (b), the transconductance of the cross coupling stage, g_m influences and contributes linearly to the circuit's Q factor. The Q factor's large output swing significantly improves phase noise performance. In the cascode construction of the primary core, transconductance is determined as follows:

$$G_{m,N2,N4(cascode)} = -\frac{g_{m4}r_{04}(r_{02}(g_{mb2} + g_{m2}) + 1)}{r_{02} + r_{04} + r_{02}r_{04}(g_{mb2} + g_{m2})}. \quad (1)$$

where g_{m2} and g_{m4} refers to the small signal

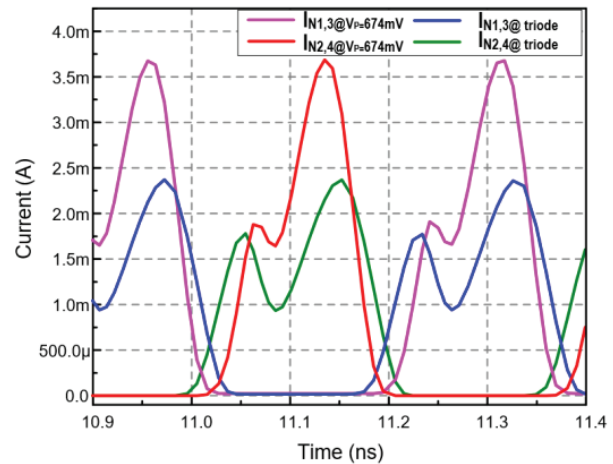


Fig. 5. Simulated drain current waveform for the dual core VCO.

trans-conductance of N_2 and N_4 respectively. The g_{mb2} is the bulk transconductance of N_2 . The intrinsic output resistance, R_o form at the node V_2 is denoted as:

$$R_O = r_{02} + r_{04} + r_{02}r_{04}(g_{mb2} + g_{m2}). \quad (2)$$

R_{02} and r_{04} refer to the output resistance of N_2 and N_4 respectively. The equivalent parallel conductance of the inductor, G_L is expressed as:

$$G_L = -\frac{1}{R_s(Q_{IN}^2 + 1)} \approx -\frac{R_s}{\omega^2 \left(\frac{L_1}{2}\right)^2}. \quad (3)$$

where Q_{IN} and R_s represents the internal quality factor of the inductor, L_1 and series equivalent resistance respectively. In the primary core, especially under wide bandwidth operation, the output of the node of V_2 is affected

by the total parasitic capacitance, C_T computed as:

$$C_T = -\frac{j\omega^3(C_{gs1}C_{gd2})}{\omega^2(C_{gs1}(C_{gd2} + C_{gs3}) + C_{gd2})}. \quad (4)$$

The negative transconductance, G_P then can be expressed as:

$$G_{TOT} = -G_L + G_P. \quad (5)$$

Hence in its full form expressed as:

$$G_{TOT} = -\frac{g_{m4}r_{o4}(r_{o2}(g_{m2} + g_{mb2}) + 1)}{2(1 + (g_{m2} + g_{mb2})r_{o2} + 2r_{o4})} + \frac{j\omega^3 C_{gs1} C_{gd2}}{2\omega^2 L_1 (C_{gs1}(C_{gsd2} + C_{gsd3}) + C_{gsd2})}. \quad (6)$$

Therefore the overall Q factor of the VCO can be evaluated as:

$$Q_{TOT} = \frac{1}{G_{TOT}} \sqrt{\frac{C_T}{\frac{R_S}{G_L}}}. \quad (7)$$

In equation (7), the total Q factor, Q_{TOT} expressed and increased with a lower total transconductance, G_{TOT} . Figure 6 shows the comparison of the Q factor in schematic and post layout. The Q factor in the post layout simulation (post.sim) result appears higher than the schematic simulation (sch.sim) due to the slight increase contribution of the parasitic capacitance. However, under a sweet spot V_P bias, the Q factor can be maintained without impacting the phase noise. Therefore, the phase noise improved proportionally affecting towards a higher voltage amplitude under a high Q factor environment.

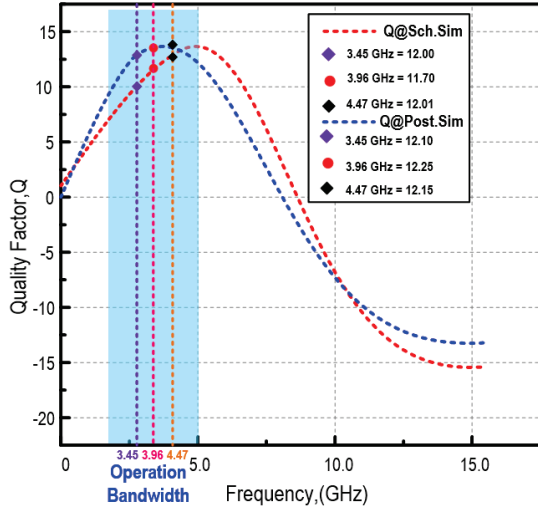


Fig. 6. Simulated Q factor comparison between schematic (sch.sim) and post layout (post.sim).

C. Theory of operation of secondary core

Figure 7 (a) exhibits the secondary core of the circuit sharing the gate bias for the four transistors N_5 - N_8

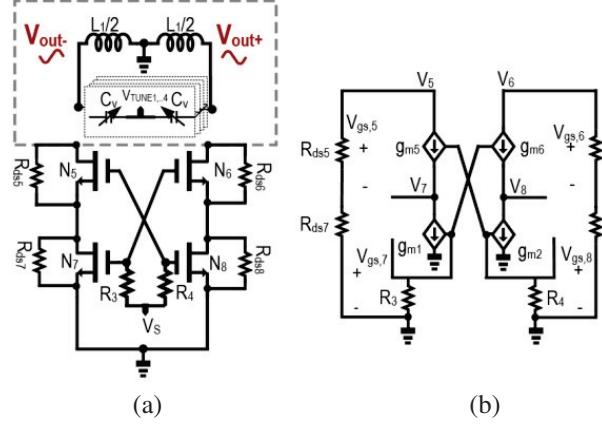


Fig. 7. Secondary core (a) circuit and (b) small signal equivalent model.

in a cascode configuration. In the half signal analysis depicted in Fig. 7 (b), the gain of each circuit is denoted as follows:

$$AV_S = g_{m7}r_{ds7}[(g_{m5} + g_{mb5})r_{ds5} + 1]. \quad (8)$$

The high gain allows the auxiliary core to increase the signal's amplitude, preserving the transistor's saturation mode condition. Figure 8 depicts a balanced amplitude as opposed to the mismatched amplitude of a conventional class-C VCO.

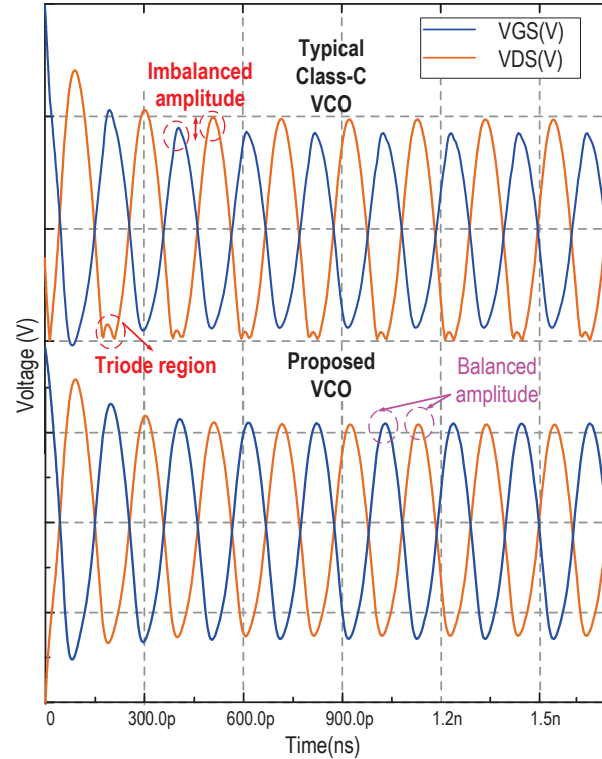


Fig. 8. Simulated drain output voltage.

III. PERFORMANCE RELIABILITY RESULTS

Figure 9 depicts the layout of the proposed VCO. The VCO occupies an active silicon area of 1.05 mm^2 and consumes only 0.7 mW with supply voltage 1.2 V supply headroom.

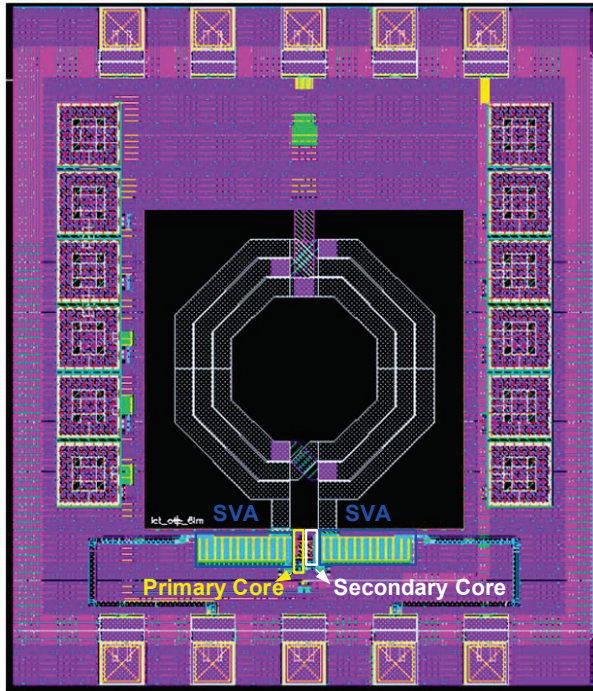
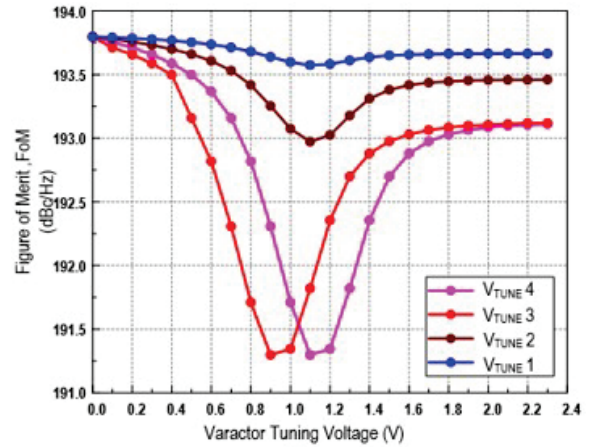
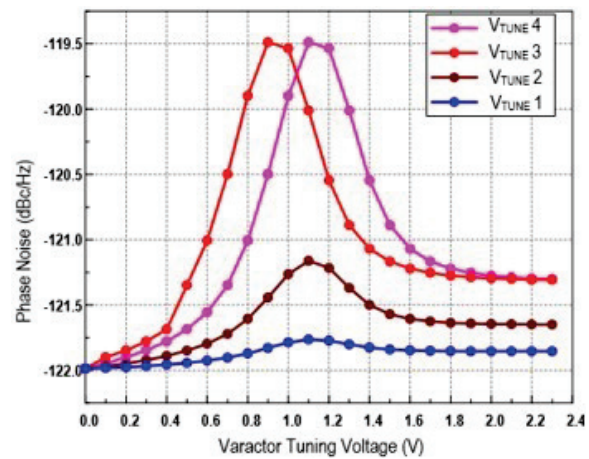


Fig. 9. Layout of proposed VCO.

Figure 10 shows the simulated dual core in which Fig. 10 (a) shows the performance of the FoM and Fig. 10 (b) depicts the PN across the tuning voltages ($V_{TUNE1} - V_{TUNE4}$) where at under a suitable tuned bias of V_p and V_s at 647 mV and 600 mV respectively. The highest FoM obtained is at 193.79 dBc/Hz whereas the lowest PN is -122 dBc/Hz at frequency of 3.45 GHz under the tuning voltage of V_{TUNE1} . The relationship is further illustrated in Fig. 11. This 3D diagram shows the highest region of the phase noise, represented as blue, comprised the lowest phase noise level achieved, contributing to the highest FoM reading, while the red region comprised the higher phase noise reading reflecting towards a lower FoM level. With this tuned variable bias, it would be a degree of freedom to obtain for the best PN and FoM performance. Figure 12 shows the result of the PN and frequency across temperatures -40 to $125 \text{ }^\circ\text{C}$. At room temperature of $25 \text{ }^\circ\text{C}$, the phase noise achieved is in the range of -122 dBc/Hz to -122.5 dBc/Hz , however at the highest temperature



(a)



(b)

Fig. 10. Simulated performance of the dual core VCO (a) FoM and (b) PN performance across the varactor tuning voltages $V_{TUNE1} - V_{TUNE4}$.

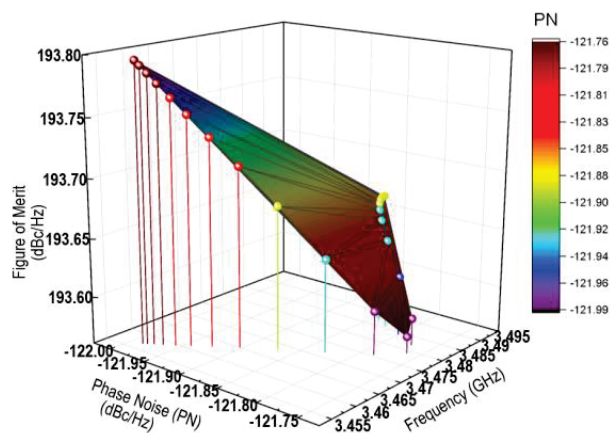


Fig. 11. Relationship of Phase Noise (PN) with frequency and Figure of Merit (FoM).

Table 1: Performance comparison of the dual core VCO with other recent related works

Performance Parameters	This Work	[16]	[17]	[18]	[19]	[20]
Frequency Range (GHz)	3.45 – 4.47	2.05 – 2.75	3.7 – 4.2	6.80–	3.8 – 5.6	8.86– 13.4
Tuning Range (%)	32.43	29	13	12	42	41
V_{DD} (V)	1.2	1.8	1.5	0.55	1.2	1.1
CMOS Tech (nm)	130	180	55	65	130	40
Power Consumption (mW)	0.7	18	6.3	5.0	5	6
$V_{neakk-to-peak}$ (V)	2.3	-	2.1	1	-	-
PN (dBc/Hz)@1MHz	-121.25	-119.5	-121	-117.5	-119.21	-112.63
FoM(dBc/Hz)@1MHz	193.25	174.6	185.05	187.2	184.9	185

$$\text{FoM} = -\text{PN} + 20\log(f_0/\Delta f) - 10\log(P_{DC}/1 \text{ mW}) \quad [21]$$

of 125 °C, the PN achieved is around -120.2 dBc/Hz. Nevertheless, for the frequency, the variation is only 300 MHz of difference across the temperatures. This shows that the performance of the PN and frequency are less impacted during the change in temperature, clearly proving its reliability. Figures 13 (a) and 13 (b) represent the frequency and the output power across the tuning voltages ($V_{TUNE1} - V_{TUNE4}$) respectively. The frequency bandwidth acquired results from 3.45 GHz to 4.47 GHz, whereas the boosted signal output power results from 5.7 dBm to 7.5 dBm. In this simulation, freedom is given to have multiple desired frequency and output power.

Table 1 tabulates the performance comparison of the dual core VCO with other recent reported works. The proposed architecture leads other VCO performances by attaining high output swing and better phase noise reading performance using minimal power consumption.

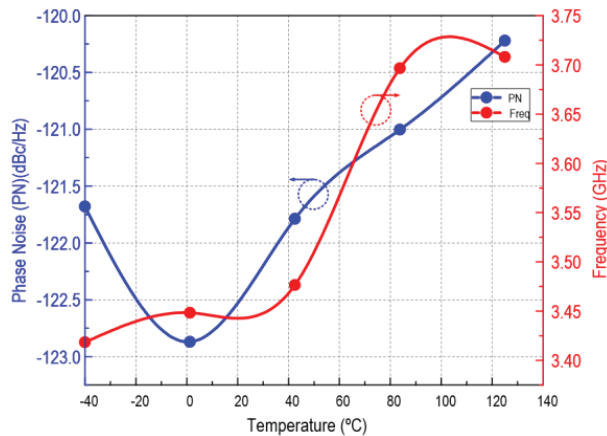
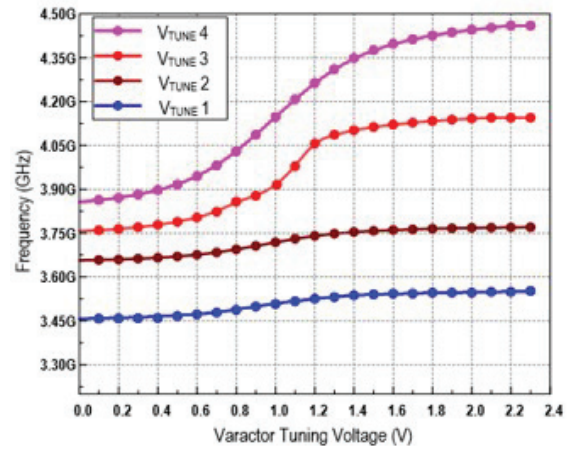
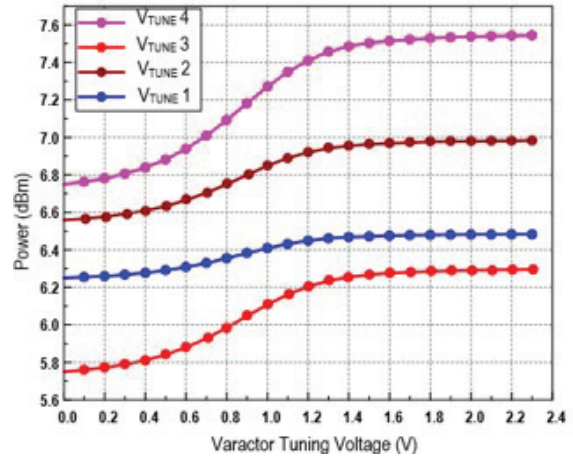


Fig. 12. Simulated PN and frequency across temperature from -40 °C to 125 °C.



(a)



(b)

Fig. 13. Performance of the dual core VCO (a) frequency (GHz) and (b) output power (dBm) across the varactor tuning voltages $V_{TUNE1} - V_{TUNE4}$.

IV. CONCLUSION

In this simulation work, a dual core VCO's design has been demonstrated. Low phase noise performance is achieved by employing a Q enhancement technique in a cascoded structure in the primary auxiliary core. The VCO output swing is also improved by the secondary core merger. The proposed dual core VCO exhibits an output voltage swing of more than 2.0 V with a minimal supply voltage headroom of 1.2 V without significantly worsening its VCO phase noise across the operating bandwidth of 3.45 GHz to 4.47 GHz, as confirmed by both schematic and post layout simulation, which agrees well. Therefore, the presented architecture qualifies for use in 5G New Radio operations due to its low phase noise and low power consumption characteristics.

ACKNOWLEDGMENT

This work was supported by the Ministry of Higher Education Malaysia for Fundamental Research Grant Scheme with Project Code FRGS/1/2019/TK04/USM/02/14 and CREST under grant number PCEDEC/6050415.

REFERENCES

- [1] M. Shahmohammadi, M. Babaie, and R. B. Staszewski, "Tuning range extension of a transformer-based oscillator through common-mode Colpitts resonance," *IEEE Trans. Circuits Syst. I, Reg. Papers*, vol. 64, no. 4, pp. 836-846, Apr. 2017.
- [2] D. Hauspie, E. C. Park, and J. Craninckx, "Wideband VCO with simultaneous switching of frequency band, active core and varactor size," *IEEE J. Solid-State Circuits*, vol. 42, no. 7, pp. 452-455, July 2006.
- [3] O. El-Aassar and G. M. Rebeiz, "A dual-core 8-17 GHz LC VCO with enhanced tuning switchless tertiary winding and 208.8 dBc/Hz peak FoMT in 22nm FDSOI," *IEEE Radio Frequency Integrated Circuits Symposium (RFIC)*, Los Angeles, CA, USA, pp. 247-250, Aug. 2020.
- [4] Y. Luo, C. Ma, Y. Gan, M. Qian, and T. Ye, "A dual-band CMOS LC-VCO with highly linear frequency tuning characteristics," *Microelectronics J.*, vol. 46, no. 12, pp. 1420-1425, June 2015.
- [5] H. Amir-Aslanzadeh, E. J. Pankratz, C. Mishra, and E. Sanchez-Sinencio, "Current-reused 2.4-GHz direct-modulation transmitter with on-chip automatic tuning," *IEEE Trans. Very Large Scale Integr. Syst.*, vol. 21, no. 4, pp. 732-746, Apr. 2013.
- [6] M. Fang, A. Kumura, and T. Yoshimasu, "A 210.4-dBc/Hz FoMT 67.9% tuning range LC-VCO IC with a single analog voltage-controlled novel varactor in 40-nm CMOS SOI," *IEEE International Symposium on Radio-Frequency Integration Technology*, Hualien, Taiwan, pp. 2021-2023, Aug. 2021.
- [7] B. Park, S. Lee, S. Choi, and S. Hong, "A 12-GHz fully integrated cascode CMOS LC VCO with Q-enhancement circuit," *IEEE Microwave and Wireless Components Letters*, vol. 18, no. 2, pp. 133-135, Feb. 2008.
- [8] H. Kim, S. Ryu, Y. Chung, J. Choi, and B. Kim, "A low phase-noise CMOS VCO with harmonic tuned LC tank," *IEEE Trans. Microw. Theory Techn.*, vol. 54, no. 7, pp. 2917-2923, July 2006.
- [9] B. D. Williamson, "A 2.4 GHz LC-VCO using on-chip inductors and accumulation-mode varactors in a CMOS 0.18 μm process," Master's thesis, University of Tennessee, Knoxville, TN, 2005.
- [10] S. Chatterjee, Y. Tsvividis, and P. Kinget, "0.5-V analog circuit techniques and their application in OTA and filter design," *IEEE J. Solid-State Circuits*, vol. 40, no. 12, pp. 2373-2387, Dec. 2005.
- [11] M. Fang and T. Yoshimasu, "A -197.3-dBc/Hz FoMT wideband LCVCO IC with a single voltage-controlled IMOS-based novel varactor in 40-nm CMOS SOI," *IEEE Trans. Microw. Theory Techn.*, vol. 68, no. 10, pp. 4116-4121, Oct. 2020.
- [12] T. Azadmousavi and E. N. Aghdam, "A low power current-reuse LC-VCO with an adaptive body-biasing technique," *AEUE - Int. J. Electron. Commun.*, vol. 89, pp. 56-61, May 2018.
- [13] T. Siriburanon, W. Deng, K. Okada, and A. Matsuzawa, "A current-reuse Class-C LC-VCO with an adaptive bias scheme," *IEEE Radio Frequency Integrated Circuits Symposium (RFIC)*, Seattle, WA, USA, pp. 35-38, June 2013.
- [14] S. Ikeda, S. Lee, H. Ito, N. Ishihara, and K. Masu, "A 0.5 V 5.96-GHz PLL with amplitude-regulated current-reuse VCO," *IEEE Microwave and Wireless Components Letters*, vol. 27, no. 3, pp. 302-304, Mar. 2017.
- [15] V. J. Higgins, F. A. Brand, and J. J. Baranowski, "Characteristics of varactor diodes biased into avalanche," *International Electron Devices Meeting*, Washington, DC, USA, pp. 14-14, Oct. 1965.
- [16] C. Sánchez-Azqueta, J. Aguirre, C. Gimeno, C. Aldea, and S. Celma, "High-resolution wide-band LC-VCO for reliable operation in phase-locked loops," *Microelectronics Reliability*, vol. 63, pp. 251-255, Aug. 2016.
- [17] M. Garampazzi, P. M. Mendes, N. Codega, D. Manstretta, and R. Castello, "Analysis and design of a 195.6 dBc/Hz peak FoM P-N class-B oscillator with transformer-based tail filtering," *IEEE J. Solid-State Circuits*, vol. 50, no. 7, pp. 1657-1668, July 2015.

- [18] Y. Peng, L. Zhou, Y. Yu, H. Liu, Y. Wu, C. Zhao, H. Tang, and K. Kang, "A harmonic-tuned VCO with an intrinsic-high-Q F23 inductor in 65-nm CMOS," *IEEE Microwave and Wireless Components Letters*, vol. 30, no. 10, pp. 981-984, Oct. 2020.
- [19] C. H. Chun, H. S. Choi, Q. D. Bui, S. Y. Kang, J. Y. Jang, U. B. Lee, I. Y. Oh, and C. S. Park, "Compact wideband LC VCO with active inductor harmonic filtering technique," *Electronic Letters*, vol. 47, no. 3, pp. 190-191, Feb. 2011.
- [20] J. Du, X. Zhang, C. Zhang, F. Meng, and N. Yan, "An ultra-wideband VCO using digitally controlled varactor arrays in 40-nm CMOS technology," *IEEE MTT-S International Wireless Symposium (IWS)*, Nanjing, China, pp. 1-3, May 2021.
- [21] P. Shasidharan, H. Ramiah, and J. Rajendran, "A 2.2 to 2.9 GHz complementary class-C VCO with PMOS tail-current source feedback achieving -120 dBc/Hz phase noise at 1 MHz offset," *IEEE Access*, vol. 7, pp. 91325-91336, July 2019.



Pravinah Shasidharan is currently pursuing a Ph.D. degree in microelectronics at the Universiti Sains Malaysia (USM), Pulau Pinang. Her research interest is in CMOS RFIC design.



Jagadheswaran Rajendran (SM'16) is currently serving as a senior lecturer at the Collaborative Microelectronic Design Excellence Center (CEDEC) and School of Electrical and Electronic Engineering, Universiti Sains Malaysia. His work is on CMOS analog IC design, CMOS Radio Frequency (RF) IC design and GaAs Monolithic Microwave Integrated Circuit (MMIC) design. To date, he has published 70 research papers, mainly in journals, and holds one US patent. Jagadheswaran Rajendran was the recipient of the IEEE Circuit and System Outstanding Doctoral Dissertation Award in 2015. He served as the Chairman of IEEE ED/MTT/SSC Penang Chapter for the years 2011 and 2018. He is also a senior member of IEEE.



Selvakumar Mariappan received his B. Eng. Tech. Degree (Hons.) in electrical engineering technology from the Technical University of Malaysia Melaka (UTeM) in 2017. He completed his Ph.D. degree in microelectronics system engineering from Universiti Sains Malaysia in 2022. He was a scholarship recipient of the Industry Graduate Research Assistant Scholarship Programme (i-GRASP) from CREST R&D, Malaysia. Selvakumar Mariappan was a post-graduate intern in Silterra Malaysia Sdn. Bhd. from 2018 to 2021 where he was involved in various IC design activities from device modelling to IC measurements. He was with QRF Solutions Sdn. Bhd. from May 2021 to August 2022 as an IC designer where he worked on numerous RFIC design projects. He served as a Post-Doctoral Fellow at the Collaborative Microelectronic Design Excellence Center (CEDEC), Universiti Sains Malaysia from September to November 2022 before being promoted to Senior Lecturer there in December 2022.



Narendra Kumar received his doctorate degree in electrical engineering from RWTH Technical University Aachen, Aachen, Germany. From early 1999 he was with Motorola Solutions, holding the position of Principal Staff Engineer (product development and testing). Since January 2011 he has been a Visiting Professor to Istanbul University. Since August 2013, he has been with the Department of Electrical Engineering at the University of Malaya, serving as an Associate Professor. He holds three US patents and four defensive patents in the area of microwave power amplifiers, all assigned to Motorola Solutions. He has authored more than 80 papers in technical journals and conferences, and three technical books published in the USA.



Masuri Othman received his master's degree in optoelectronics from the University of Essex, UK, and his Ph.D. degree in microelectronics from the University of Southampton, UK. His main research interests are in the areas of microelectronics and IC design,

energy harvesters and technology planning and commercialization. He joined the National University of Malaysia in 1978, was promoted to an Associate Professor in 1989, and subsequently in 1996 to the post of a Professor in microelectronics. He was the Deputy Director of the Institute of Micro and Nanoelectronics (IMEN), UKM, from 2004 to 2006. He was on secondment to the Malaysian Institute of Microelectronics (MIMOS) from 2005 to 2011 as the Director of MEMS and Nanotechnology and at the same time has produced more than 20 patents mainly in the areas of MEMS and energy harvesting. From 2011 to 2014, he was the Commercialization Director at the Ministry of Science and Technology, Malaysia. In 2016, he rejoined IMEN with the main task of spearheading frontier research as well as the technology commercialization of the research and development. During his tenure he has produced more than 100 research papers and has won several national awards in his research areas.

